THE UNIVERSITY *of* EDINBURGH

Spectral properties of homogeneous magnetohydrodynamic turbulence

Màiri Elise McKay

Doctor of Philosophy
The University of Edinburgh
2018

Abstract

Magnetohydrodynamics (MHD) is the study of how an electrically-conducting fluid interacts with a magnetic field. Many of the constituents of the universe possess a magnetic field and MHD has applications ranging from geophysical flows to solar and galactic physics; in fact, the possible generation of magnetic fields due to early-universe phase transitions makes MHD a valuable tool even in cosmology. From a more practical point of view, liquid metals, such as those required in nuclear fusion reactors, can be described by the MHD equations.

In this thesis various aspects of homogeneous, incompressible MHD without a mean magnetic field are explored. This stripped-back setting facilitates the development of deeper knowledge of the fundamental energy transfer mechanisms of MHD turbulence. A complementary set of numerical and analytical results are presented, which explore the consequences of the fundamental interactions in MHD.

First of all, the results of high-resolution direct numerical simulations of MHD subject to three different forcing functions are analysed in order to determine whether or not the method of energy injection affects the behaviour of the fields. Next, energy transfers between different length scales are computed and compared in cases with differing values of magnetic and cross helicity, with a view to understanding their influence on reverse energy transfer. The effect of the magnetic Prandtl number is studied in detail by varying both the kinetic and magnetic Reynolds numbers in decaying turbulence with initially large values of magnetic helicity. This allows us to distinguish large magnetic Prandtl number effects from large magnetic Reynolds number effects and small kinetic Reynolds number effects.

Lay summary

Magnetism and electricity are intrinsically linked: electric currents produce magnetic fields and magnetic fields can influence electric charges. When we think of electrical conductors, we tend to think of wires and other solid objects, but some gases and liquids can conduct electricity, too. Most fluids that we encounter every day are nonconducting, but as soon as we leave the surface of the Earth and consider the universe around it we quickly find that almost everything in nature is a plasma, made up of electrically-charged particles. When these particles move around, they generate a magnetic field, and this, in turn, influences the movement of the particles. These movements, which are often very turbulent, can be described mathematically by the equations of magnetohydrodynamics.

From an Earthly (i.e. practical) point of view, magnetohydrodynamics is of use in the development of fusion power and MHD drives which could power ships. Extraterrestrially, magnetohydrodynamic turbulence plays an important (yet often underrated) role in the construction and maintenance of stars and galaxies. It describes our planetary magnetic field, which somehow looks a lot like the magnetic field of a bar magnet, despite being made up of something far more complex. It might also provide some clarification of facets of the universe's murky beginnings.

In most situations, turbulence causes disorganisation. To visualise this, one can think of how large, coherent water waves eventually break up into smaller and smaller ripples. In magnetohydrodynamics, quite remarkably, the opposite can happen: magnetic fields can build up across large distances from initially small disturbances. This would be like dropping a stone into a pool and creating a tidal wave.

To gain a better theoretical understanding of the complexities of magnetohydrodynamic turbulence, it is helpful to study an abstract type of magnetohydrodynamics in which the fluid and its magnetic field are *homogeneous*. This is a dramatically simplified version of reality which consists of, essentially, an infinite region of electrically-charged gas. The closest real-life version of this is deep space, where magnetic fields have been measured despite there not being much of anything else present. By taking this approach of homogeneity, it means that instead of comparing the behaviour of the fluid and magnetic

field at every different point in space, we need only consider what the fluid behaves like at different length scales. This is what the word *spectral* in the title refers to: the turbulence is decomposed into a spectrum of fluctuations; long waves, short waves and everything in between. Even in the homogeneous case, the equations are much too complicated to be solved by pen and paper alone. For this reason, scientists turn to supercomputers to simulate and analyse magnetohydrodynamic data. Despite the simple geometry, studying homogeneous magnetohydrodynamics can actually produce valuable information about, for example, cosmological problems and the Earth's large-scale magnetic field.

Declaration

I declare that this thesis was composed by myself, that the work contained herein is my own except where explicitly stated otherwise in the text, and that this work has not been submitted for any other degree or professional qualification except as specified.

Parts of this work have been published in [79, 80, 82, 89, 90].

(*Màiri Elise McKay, 2018*)

Acknowledgements

This work used the ARCHER UK National Supercomputing Service [7], made available through the Edinburgh Compute and Data Facility (ECDF, [44]) and the Director's Time. I was financially supported by the Engineering and Physical Sciences Research Council (EP/M506515/1).

I am grateful to my supervisor, Prof Arjun Berera, for his guidance, patience, insight and good humour. His encouragement to reach for opportunities has been invaluable.

I am also grateful to Dr Moritz Linkmann for being a mentor to me during the first half of my PhD, and for, together with Dr Samuel Yoffe, writing the code which the results of my thesis depended on.

Thank you to my collaborator and officemate, Richard Ho, who excelled in both of those roles.

It was a pleasure to work with the following MSc and MPhys students: Erin Goldstraw, Daniel Clark, Adam Chalupa, Clara Despard and Andrés Cathey Cevallos.

With all my heart I thank my friends and family for being the most wonderful aspect of my life. There are too many of you to name (I'm the luckiest person in the world!) but I suppose I should at least mention Zak. And my parents. And Mary, Liane, Murray, Adam, everyone in Harbingers Drum Crew... Ok, ok, I'll stop now!

Contents

List of Figures

List of Tables

Chapter 1

Introduction

Turbulence is observed in an enormous variety of situations but fully understood in few. It has been a source of intrigue for both scientists and artists for hundreds of years. The Navier-Stokes equations, which describe the turbulent flow of a nonconducting fluid, were written down in the nineteenth century but their nonlinear nature still inhibits a complete understanding of them.

Above a certain temperature, atoms become ionised and fluids exist as plasmas. Most of the constituents of the Universe, including stars, galaxies and the interstellar medium, are above this temperature. The movement of the electrically-conducting particles in such a fluid causes currents to form, and these currents can then amplify tiny seed magnetic fields.

In order to describe the behaviour of conducting fluids, the Navier-Stokes equations are combined with Maxwell's equations of electromagnetism to form the equations of magnetohydrodynamics (MHD). The MHD equations dictate how the movement of the fluid affects the magnetic field lines and vice versa. The seminal work on MHD was done by Hannes Alfvén [5], who developed theories explaining aurorae and geomagnetic storms, correctly predicted the presence of a galactic magnetic field, and was awarded the Nobel Prize in 1970.

Arguably the most fascinating feature of MHD turbulence is the tendency for large-scale self-organisation to take place. This is something which is rarely possible in nonconducting fluids and seems to oppose the very concept of turbulence. The movement of energy from small, turbulent length scales to larger length scales is known as reverse spectral transfer (RST) or the inverse cascade. This effect is unusual in nonconducting fluids but commonplace in MHD. Large-

scale magnetic fields can come about as a result of the redistribution of magnetic energy or through dynamo action, which is the conversion of kinetic to magnetic energy. RST provides insights into questions about magnetic fields in all sorts of settings, from planetary to intergalactic magnetic fields.

1.1 Structure of thesis

This thesis is an exploration of spectral energy transfer properties between length scales in homogeneous, incompressible MHD turbulence without a mean magnetic field.

In Chapter 2 I begin by testing three nonhelical large-scale mechanical methods of energy injection using direct numerical simulations (DNS). The forces each produce qualitatively similar energy spectra and show that the large scales in nonhelical MHD have little influence on the small scales, as is the case in hydrodynamics. Until now, this concept was assumed but untested. I further show that cross helicity can enter the system via the forcing function and it is therefore necessary to protect against this.

Next, in Chapter 3, I look at the way energy is transferred between scales by comparing DNS results of decaying data with different initial values of the ideal invariants. The energy transfer between two scales in homogeneous turbulence is mediated by a third scale, and I show that energy is primarily transferred in interactions between two small scales and one large scale, or three neighbouring scales. To do this, I wrote a module for my research group's in-house DNS code, which enhances the functionality by dissecting shell-to-shell scale interactions. I draw further conclusions in an analytical detour where the MHD equations are deconstructed and the evolution of three coupled helical modes is considered, allowing for a novel and fundamental understanding of MHD energy transfer.

Chapter 4 moves towards the dissipative scales of MHD turbulence. The magnetic Prandtl number, Pr_M, quantifies the relative turbulence of the magnetic and velocity fields, and is also closely associated with dissipation. In this chapter I push current computational limits and undertake the largest systematic study of the magnetic Prandtl number to date. Reverse spectral transfer is found in nonhelical low-Pr_M turbulence for the first time, indicating that the threshold for sustainable large-scale magnetic field amplification is not solely dependent on the

Reynolds numbers and the magnetic Prandtl number, but also on the separation between the various key length scales that characterise a turbulent system.

But first, an introduction to some relevant concepts and literature is needed. What follows is a brief overview of aspects of magnetohydrodynamics that will be relevant in subsequent chapters of this thesis. There are many excellent books on the subjects of MHD turbulence (e.g. [18, 39]) and hydrodynamic turbulence (e.g. [53, 87, 109]) which I would recommend the reader spend some time with for a more in-depth account.

1.2 The magnetohydrodynamic equations

The equations of incompressible magnetohydrodynamics are

$$\partial_t \mathbf{u} = -\nabla P - (\mathbf{u}\cdot\nabla)\mathbf{u} + (\nabla\times\mathbf{b})\times\mathbf{b} + \nu\nabla^2\mathbf{u} + \mathbf{f_u}, \tag{1.1}$$

$$\partial_t \mathbf{b} = (\mathbf{b}\cdot\nabla)\mathbf{u} - (\mathbf{u}\cdot\nabla)\mathbf{b} + \eta\nabla^2\mathbf{b} + \mathbf{f_b}\ , \tag{1.2}$$

$$\nabla\cdot\mathbf{u} = 0\ , \tag{1.3}$$

$$\nabla\cdot\mathbf{b} = 0\ , \tag{1.4}$$

where $\mathbf{u}$ is the velocity field, $\mathbf{b}$ is the magnetic field in Alfvén units, (i.e. the same units as the velocity) P is the pressure and the density is constant and set to one. The pressure term can be eliminated as a variable because of the incompressibility condition, $\nabla\cdot\mathbf{u} = 0$, and computed by taking the divergence of the velocity equation, (1.1). The kinematic viscosity and the magnetic resistivity are ν and η.

There are two ways to inject energy into a magnetohydrodynamic system: via a mechanical force, $\mathbf{f_u}$, or via a magnetic force, $\mathbf{f_b}$. The forcing functions must be prescribed and a traditional choice in simulations of MHD is to use a large-scale, mechanical method of energy injection. In this thesis we consider only decaying or mechanically-forced turbulence, so $\mathbf{f_b} = 0$. Several varieties of mechanical forcing in simulations will be analysed in Chapter 2.

The second term on the right-hand side of the velocity equation represents advection of the velocity field by the flow, $-(\mathbf{u}\cdot\nabla)\mathbf{u}$, and the third term, $(\nabla\times\mathbf{b})\times\mathbf{b}$, is the effect of the Lorentz force. On the right-hand side of the magnetic field evolution equation (1.2) there is the stretching of the magnetic

field lines by the flow, $(\mathbf{b} \cdot \nabla)\mathbf{u}$, and the advection of the magnetic field lines, $-(\mathbf{u} \cdot \nabla)\mathbf{b}$. These four terms ultimately describe the transfer of kinetic and magnetic energy and will be studied in Chapter 3. Kinetic and magnetic energy is dissipated via $\nu\nabla^2\mathbf{u}$ and $\eta\nabla^2\mathbf{b}$ respectively. The dependence of dissipation on ν and η is examined in Chapter 4.

If the magnetic field is set to zero then the equations reduce to the Navier-Stokes equations for incompressible hydrodynamic flows,

$$\partial_t \mathbf{u} = -\nabla P - (\mathbf{u} \cdot \nabla)\mathbf{u} + \nu\nabla^2\mathbf{u} + \mathbf{f}_\mathbf{u}, \tag{1.5}$$

$$\nabla \cdot \mathbf{u} = 0 \ . \tag{1.6}$$

In other words, an existing magnetic field may interact with a conducting fluid through the Lorentz force but it cannot be generated from a purely hydrodynamical flow. Magnetohydrodynamics is the study of the evolution of a magnetic field, without addressing creation mechanisms of the initial field.

1.2.1 Quantifying turbulence using dimensionless parameters

How might we compare the rushing flow of our blood through our veins to a flow of magma beneath the Earth? Likewise, how can we reasonably compare the magnetic fields of, say, the Earth and a galaxy, when the two objects are so vastly different? How can we quantify how turbulent something - a fluid or a magnetic field - is? The study of turbulence has long been associated with *universality*, which is the idea that seemingly disparate flows can have various features in common; for example, what it takes to make a flow transition from smooth to turbulent.

In a nonconducting fluid there is one key dimensionless parameter. The Reynolds number compares the advective and viscous terms in the Navier-Stokes equations,

$$\mathrm{Re} = \frac{UL}{\nu} \ , \tag{1.7}$$

where U is the root-mean-square velocity and L is a characteristic length scale to be defined. If $\mathrm{Re} < 1$ the viscous term dominates and energy is mostly dissipated rather than advected. At some critical Reynolds number greater than one there is a transition from a smooth flow to a turbulent flow. This varies depending

on the nature of the system: in pipe flow, the number is in the range of 1000 to 3000 [9, 45, 87] but in some simulated flows turbulence can be evident at Reynolds numbers not much greater than 1. The reason that there is not a more precise value of Re even for well-studied systems such as pipe flows is that, at moderate Reynolds numbers, turbulence can be transient; switching on and off, seemingly at random. So there is some subtlety in the defining of the critical Reynolds number: it can be associated with a value below which turbulence cannot be excited, or it can be associated with a value above which smooth flow is impossible. Either way, it is not easy to pin down the exact value of the critical Reynolds number in any given situation, but nonetheless it is useful to know the order of magnitude at which it occurs. Many analytical results depend on the infinite-Re limit, meaning that in experiments and simulations one hopes to find an asymptotic trend towards this limit.

Generalising to MHD, the magnetic Prandtl number compares the strengths of the viscous and resistive forces

$$\mathrm{Pr}_M = \frac{\nu}{\eta} = \frac{\mathrm{Re}_M}{\mathrm{Re}} \ , \tag{1.8}$$

and the magnetic Reynolds number, Re_M, quantifies the turbulence of the magnetic field

$$\mathrm{Re}_M = \mathrm{Re}\ \mathrm{Pr}_M = \frac{UL}{\eta} \ . \tag{1.9}$$

If $\mathrm{Pr}_M > 1$ then the magnetic field is more turbulent than the velocity field, and vice versa. There is thought to exist some critical magnetic Reynolds number below which a magnetic field cannot be sustained. This is also affected by the magnetic Prandtl number.

These three dimensionless numbers, Re, Re_M and Pr_M, are key parameters in the study of MHD and can each take on extreme values in physical applications. These applications will be discussed later in the chapter.

1.2.2 Ideal invariants

There are three quantities which are conserved in the ideal (dissipationless) limit of magnetohydrodynamics: these are the total energy, the magnetic helicity, and the cross helicity. The latter two quantities represent the knottedness of magnetic field lines and the alignment between the velocity and magnetic fields [97]. Both

of these have maximum possible values and so I will define them through the *relative* magnetic and cross helicities. The relative magnetic helicity is

$$\rho_b = \langle \mathbf{b} \cdot \mathbf{a} \rangle / (\langle |\mathbf{b}|^2 \rangle \langle |\mathbf{a}|^2 \rangle)^{1/2} \ , \tag{1.10}$$

where the magnetic helicity is $H_M = \langle \mathbf{b} \cdot \mathbf{a} \rangle$, $\mathbf{a}$ is the magnetic vector potential, $\mathbf{b} = \nabla \times \mathbf{a}$, and the angular brackets denote a spatial average. The magnetic helicity is not gauge invariant unless it is defined over an infinite volume, or one for which the magnetic field is zero at the boundary, making helicity injection impossible. A modified definition, using a reference magnetic field, can be used when helicity injection is required [15, 51, 99]. The relative cross helicity can be quantified in two ways:

$$\rho_c = \langle \mathbf{u} \cdot \mathbf{b} \rangle / (\langle |\mathbf{u}|^2 \rangle \langle |\mathbf{b}|^2 \rangle)^{1/2} \text{ and} \tag{1.11}$$

$$\sigma_c = 2\langle \mathbf{u} \cdot \mathbf{b} \rangle / (\langle |\mathbf{u}|^2 \rangle + \langle |\mathbf{b}|^2 \rangle) \ , \tag{1.12}$$

Where $H_C = \langle \mathbf{u} \cdot \mathbf{b} \rangle$ is the cross helicity itself. The former is a measurement of the alignment between the two fields, whereas the latter is the ratio of two ideal invariants, the cross helicity and total energy. Together these definitions obey the inequality $|\sigma_c| \leq |\rho_c| \leq 1$ [59, 111]. Both definitions have their merits, and their differences and similarities are explored in section 2.3.2. We focus our attention mostly on the larger of the two, ρ_c.

In the absence of a magnetic field there are only two ideal invariants: the energy and the kinetic helicity, which is the kinetic analogue of the magnetic helicity. Kinetic helicity, however, is no longer conserved in MHD flows. The relative kinetic helicity is defined as

$$\rho_u = \langle \mathbf{u} \cdot \boldsymbol{\omega} \rangle / (\langle |\mathbf{u}|^2 \rangle \langle |\boldsymbol{\omega}|^2 \rangle)^{1/2} \ , \tag{1.13}$$

where $H_K = \langle \mathbf{u} \cdot \boldsymbol{\omega} \rangle$ is the kinetic helicity and $\boldsymbol{\omega} = \nabla \times \mathbf{u}$ is the vorticity.

1.2.3 A more symmetric system

Soon after the original MHD equations were written down, an alternative formulation was set up, inspired by a desire for symmetry [46]. Since the magnetic and kinetic energies are not seperately conserved, the variables are thought of as

less pure, mathematically. The Elsässer variables, $\mathbf{z}^+$ and $\mathbf{z}^-$, are defined as

$$\mathbf{z}^{\pm} = \mathbf{u} \pm \mathbf{b} \ . \tag{1.14}$$

In terms of these new variables, the MHD equations are

$$\partial_t \mathbf{z}^{\pm} = -\nabla \tilde{P} - (\mathbf{z}^{\mp} \cdot \nabla)\mathbf{z}^{\pm} + \nu_+ \mathbf{z}^{\pm} + \nu_- \mathbf{z}^{\mp} + \mathbf{f_u} \pm \mathbf{f_b} \ , \tag{1.15}$$

$$\nabla \cdot \mathbf{z}^{\pm} = 0 \ , \tag{1.16}$$

where $\nu_{\pm} = \frac{1}{2}(\nu \pm \eta)$ and $\tilde{P} = P + \frac{1}{2}|\mathbf{b}|^2$ is the total magnetic pressure (bearing in mind the density has been set to one).

The Elsässer energies, $E_{\pm} = \frac{1}{4}|\mathbf{z}^{\pm}|^2$ are conserved seperately, and the total energy is $E = E_K + E_M = E_+ + E_-$. The cross helicity is $H_c = \frac{1}{4}\left(|\mathbf{z}^+|^2 - |\mathbf{z}^-|^2\right) = E_+ - E_-$ and the relative cross helicity, which is bound by ± 1, is

$$\rho_c = \frac{E_+ - E_-}{E_+ + E_-} \ . \tag{1.17}$$

Taking the dot product of the Elsässer fields produces what is called the residual energy,

$$E_R = \langle \mathbf{z}^+ \cdot \mathbf{z}^- \rangle = E_K - E_M \ . \tag{1.18}$$

The final ideal invariant, magnetic helicity H_M, tends not to appear in the Elsässer formulation. The realisability condition which constrains its maximum value can be expressed as

$$H_M \leq 2kE_M = k(E - E_R) \ , \tag{1.19}$$

meaning that the relative magnetic helicity is

$$\rho_M = \frac{H_M}{k(E - E_R)} \ . \tag{1.20}$$

When there is a mean magnetic field $\mathbf{B_0}$ the regime is called *strong MHD* and the system is very anisotropic. The Elsässer equations (1.15) and (1.16) can be linearised about $\mathbf{B_0}$. Magnetohydrodynamic interactions are then called Alfvén waves which travel along the magnetic field lines.

1.3 Homogeneous MHD

The complexity of turbulent flows means that simplfications need to be made in order make progress, both in analytical studies and in numerical investigations. In hydrodynamics, some of the most critical theoretical findings have been discovered in the context of homogeneous, isotropic turbulence (HIT). These results often also take the flows to be incompressible. Homogeneity and isotropy allow fundamental aspects of turbulence to be isolated, removing concern for additional effects from, e.g., rotation or a mean flow. If all this seems artificial, it's because it is: strictly speaking, flows of this variety cannot exist in nature. That said, comparable flows could be those of the deep ocean, far from any boundaries. In numerical work, homogeneity is replaced by periodic boundary conditions.

In the case of MHD, homogeneity can be maintained only if there is no mean magnetic field: a mean velocity flow can be removed via a Gallilean transformation (i.e. by considering a reference frame which moves with the mean flow) but a mean magnetic field cannot be transformed away like this [18]. Isotropy in homogeneous MHD, even without a mean magnetic field, is not easily satisfied, but the fluid at large scales is approximately isotropic, with the smaller scales becoming less so [35, 58, 121, 122]. In the same way that oceanic physics is comparable to HIT, deep space may be a good testing ground for homogeneous MHD without a mean magnetic field. Compressibility effects are small in this context [126] and relativistic effects can be accounted for by some simple changes of variables [23], meaning that the nonrelativistic, incompressible MHD equations are surprisingly useful. Furthermore, building a strong foundation of knowledge through studying homogeneous MHD means that more complex situations can be dismantled and eventually understood.

1.3.1 Spectral properties

Homogeneity is the invariance of translations. It means that specific locations in a flow are not relevant; rather, only the size of separation between any two points is relevant. In other words, the problem is best tackled by considering length scales. This way of thinking is much like how one can make sense of a musical chord by decomposing it into its constituent notes, i.e. frequencies, except that in homogeneous turbulence we consider the distribution of energy across length

scales at a fixed moment in time rather than frequencies at a fixed point in space. HIT and homogeneous MHD are generally approached in Fourier space. Problems are formulated in terms of wavevectors, $\mathbf{k}$, and spectral quantities are then considered. For the fields to be physical, we require $\mathbf{u}(-\mathbf{k},t) = \mathbf{u}^*(\mathbf{k},t)$ and $\mathbf{b}(-\mathbf{k},t) = \mathbf{b}^*(\mathbf{k},t)$, where the asterisk denotes the complex conjugate.

In Fourier space the kinetic and magnetic energy spectra are defined as

$$E_K(k,t) = \frac{1}{2}\int_{|\mathbf{k}|=k} d\mathbf{k}\langle|\mathbf{u}(\mathbf{k},t)|^2\rangle \ , \tag{1.21}$$

$$E_M(k,t) = \frac{1}{2}\int_{|\mathbf{k}|=k} d\mathbf{k}\langle|\mathbf{b}(\mathbf{k},t)|^2\rangle \ . \tag{1.22}$$

In words, we have summed over the energies of each wavevector whose magnitude is k and taken a spatial average. The total kinetic and magnetic energies are then the sums of the energies of each wavenumber,

$$E_K(t) = \int_0^\infty dk E_K(k,t) \ , \tag{1.23}$$

$$E_M(t) = \int_0^\infty dk E_M(k,t) \ , \tag{1.24}$$

and, of course, the total energy is

$$E(t) = \int_0^\infty dk E_(k,t) = \int_0^\infty dk \left(E_K(k,t) + E_M(k,t)\right) \ .$$

It is straightforward to derive the time evolution of the energy spectra from the MHD equations. Taking the dot product of (1.1) with $\mathbf{u}$ and (1.2) with $\mathbf{b}$ in Fourier space gives

$$\partial_t E_K(k,t) = T_{uu}(k,t) + T_{bu}(k,t) - D_K(k,t) \ , \tag{1.25}$$

$$\partial_t E_M(k,t) = T_{ub}(k,t) + T_{bb}(k,t) - D_M(k,t) \ , \tag{1.26}$$

where I have introduced the transfer functions $T_{xy}(k,t)$ and the dissipation spectra $D_x(k,t)$. The transfer functions describe the energy transferred from

field x to field y at wavenumber k.

$$T_{uu}(k,t) = -\int d^3\mathbf{x}\mathbf{u}(\mathbf{u}\cdot\nabla)\mathbf{u} \ , \tag{1.27}$$

$$T_{bu}(k,t) = \int d^3\mathbf{x}\mathbf{u}(\mathbf{b}\cdot\nabla)\mathbf{b} \ , \tag{1.28}$$

$$T_{ub}(k,t) = \int d^3\mathbf{x}\mathbf{b}(\mathbf{b}\cdot\nabla)\mathbf{u} \ , \tag{1.29}$$

$$T_{bb}(k,t) = -\int d^3\mathbf{x}\mathbf{b}(\mathbf{u}\cdot\nabla)\mathbf{b} \ , \tag{1.30}$$

and the dissipation spectra are

$$D_K(k,t) = \int d^3\mathbf{x}\nu k^2|\mathbf{u}|^2 = 2\nu k^2 E_K(k,t) \ , \tag{1.31}$$

$$D_M(k,t) = \int d^3\mathbf{x}\eta k^2|\mathbf{b}|^2 = 2\eta k^2 E_M(k,t) \ . \tag{1.32}$$

Integrating the transfer functions over all wavenumbers leads to the continuity relations

$$T_{uu}(t) = T_{bb}(t) = 0 \text{ and} \tag{1.33}$$

$$T_{bu}(t) = -T_{ub}(t) \ . \tag{1.34}$$

$$\tag{1.35}$$

The integrated dissipation spectra are the kinetic and magnetic dissipation rates,

$$\varepsilon_K(t) = \int_0^\infty dk D_K(k,t) \text{ and} \tag{1.36}$$

$$\varepsilon_M(t) = \int_0^\infty dk D_M(k,t) \ . \tag{1.37}$$

During a steady state, the average energies, dissipations and energy transfers are independent of time, and, if the velocity field is forced at large scales in the absence of magnetic forcing, then $T_{ub} = \varepsilon_M$.

1.3.2 Triadic interactions

The MHD equations are quadratic in $\mathbf{u}$ and $\mathbf{b}$, meaning that interactions occur between three wavenumbers, $\mathbf{k}, \mathbf{p}$ and $\mathbf{q}$, such that $\mathbf{k}+\mathbf{p}+\mathbf{q} = 0$ (this is true for

any homogeneous field or fields; see Appendix A). From equations (1.27)-(1.30) we can see that two types of coupling occur: the hydrodynamic interaction, involving three velocity modes, and the magnetic interaction, involving a velocity mode and two magnetic modes. As we will show in Chapter 3, the major players in these triad interactions are local and very nonlocal interactions. Local interactions are those for which $k \simeq p \simeq q$, meaning that the triangle formed by the triad is approximately equilateral. Nonlocal interactions involve one small wavenumber and can result in local or nonlocal energy transfers. For example, if $k < p \simeq q$ there can be a local energy transfer between p and q mediated by the large scale k and a nonlocal energy transfer between k and p mediated by q, or between k and q mediated by p. Understanding the shapes of triadic interactions and the locality of energy transfers is important from a theoretical point of view and also a practical point of view. Simulations which only resolve the larger scales of a system must be able to accurately model the interactions with small scales.

1.3.3 Energy cascades and length scales

One of the cornerstones of HIT theoretical knowledge is the Richardson-Kolmogorov energy cascade; that is, the steady transfer of energy from the largest scales of the system to progressively smaller scales. This concept carries over to more complicated forms of turbulence and is indeed easily visualisable in the way large water waves break up into smaller and smaller waves. The standard energy cascade in hydrodynamics is said to be direct, i.e. from large to small scales, and local, i.e. energy is transferred between neighbouring wavenumbers. In this idealised picture the flux between scales is constant and the system is self-similar, with the energy spectrum following what is called the Kolmogorov scaling, $E_K(k) \simeq k^{-5/3}$, which is derived through dimensional analysis (see e.g. [53]). A consequence of this is that the smaller scales should have no memory of the method of large-scale energy injection or geometry.

Two length scales play an important role in hydrodynamics: the integral length scale,

$$L(t) = \frac{3\pi \int d\mathbf{k} E_K(k) k^{-1}}{4 \int d\mathbf{k} E_K(k)} \ , \tag{1.38}$$

and the Kolmogorov (dissipative) microscale,

$$l_\nu(t) = \left(\frac{\nu^3}{\varepsilon_K}\right)^{\frac{1}{4}} \ . \tag{1.39}$$

These scales are, roughly speaking, the largest and smallest scales of interest. The Kolmogorov scale is the length scale at which the turbulent and viscous effects are balanced: at smaller scales, dissipation dominates, and therefore interactions involving scales much smaller than this can safely be ignored.

The separation between these two scales increases as the Reynolds number increases. If the separation between the largest and smallest scales is large, then an *inertial range* develops between the two. In this range, the turbulence is self-similar and can obey the Kolmogorov spectrum. This is commonly the case in HIT and is observed in many other contexts, too.

There is a further useful small length scale which was historically easier to measure than the dissipative scale in hydrodynamic experiments. The Taylor microscale is

$$\lambda = \sqrt{\frac{E_K \nu}{\epsilon_K}} \, . \tag{1.40}$$

This length characterises the scale at which dissipative effects begin to become relevant and distort the energy spectrum away from the Kolmogorov scaling.

Returning to MHD, the situation is different because there are two dissipative scales to consider,

$$l_\nu(t) = \left(\frac{\nu^3}{\varepsilon_K}\right)^{\frac{1}{4}} \, , \tag{1.41}$$

$$l_\eta(t) = \left(\frac{\eta^3}{\varepsilon_M}\right)^{\frac{1}{4}} \, , \tag{1.42}$$

and some ambiguity in the choice of dissipation by which to define them. Using only kinetic quantities in the definition of the viscous microscale and magnetic quantities in the definition of the resistive microscale, as above, then their ratios are

$$\frac{l_\nu(t)}{l_\eta(t)} = \left(\frac{\varepsilon_K}{\varepsilon_M}\right)^{\frac{3}{4}} \mathrm{Pr}_M^{-\frac{1}{4}} \, . \tag{1.43}$$

As we will discuss in Chapter 4, the kinetic-to-magnetic dissipation ratio may scale with the magnetic Prandtl number, $\varepsilon_K/\varepsilon_M \simeq \mathrm{Pr}_M^p$, with measurements suggesting $0 < p < 1$ [22]. Then the ratio of the two dissipative length scales is proportional to $\mathrm{Pr}_M^{\frac{3p-1}{4}}$. On the other hand, if the total dissipation is used instead of the kinetic and magnetic dissipation rates, then when the magnetic Prandtl number is unity the two dissipative length scales should coincide. This is not what is seen in simulations.

1.3.4 Simulating (homogeneous) magnetohydrodynamics

The significance of magnetic fields in astrophysics and geophysics means that magnetohydrodynamics deserves to be thoroughly understood. Unfortunately, with the exception of the solar wind, naturally-occurring magnetohydrodynamical flows are unreachable for *in situ* observational measurements. One might then think to replicate conditions of, for example, the Sun's corona in a laboratory setting, but this is also fraught with difficulties. For example, there are not many possible options for measuring the velocity field of an MHD flow since conducting fluids tend to be opaque and destructive to probes. In addition, the low magnetic Prandtl number of liquid metals means that experiments require very strong forcing to sustain a magnetic field [98].

Aside from solar wind data, the main experimental tool of the magnetohydrodynamicist is the computer. It is uncommon to read a paper which does not rely on numerical experiments for its results. This is not a complaint: numerical experiments can be repeated and fine-tuned as much as the computational budget will allow.

Homogeneous MHD simulations, like their hydrodynamic counterpart, can be divided broadly into two main categories: direct numerical simulations (DNS) and large eddy simulations (LES). DNS simulate the MHD equations fully while LES simulate only the largest scales, replacing the smaller-scale behaviour with some simplified model. Although LES can be justified in hydrodynamics, where the small scales tend not to have a great effect on the overall problem, it is less appropriate in MHD where there is a stronger coupling between the large and small scales. However, the use of a small-scale model reduces the computational cost (which is proportional to $\mathrm{Re}^{9/4}$ in DNS [18]), making LES quite desirable. See [93] for a recent overview of LES applied to MHD.

The numerical results of this thesis came from the in-house DNS code, (see [81, 138] for details). The code simulates a three-dimensional periodic domain with lattice sizes of up to 2048^3 points. The initial fields were random Gaussian with magnetic and kinetic energy spectra of the form $E_{M,K}(k, t = 0) = Ck^4 \exp(k^2/(2k_0)^2)$, where C is a positive real number and k_0 is the peak of the spectrum, which was set to $k_0 = 5$ in the majority of cases and $k_0 = 40$ otherwise. The maximum wavenumber on a lattice of N^3 points is approximately $N/3$ because of the dealiasing process which removes the erroneous wavenumber couplings that occur due to the periodic domain. There was no imposed magnetic

guide field, meaning that the simulated fields were approximately isotropic.

When computing spectral quantities, it is important to note that the turbulence is generated on a discrete Cartesian lattice, so most points do not have integer values of k. Instead, a shell-average of points with wavenumbers $n - 0.5 \leq k < n + 0.5$, where n is a positive integer, is used when calculating spectral quantities. This means that sometimes the density of states in a particular shell will be higher or lower than the continuum limit of $4\pi k^2$, causing bumps to appear in the spectra. To counteract this, we have taken the spectral energy densities in the n^{th} shell S_n to be $E^n_{K,M} = \frac{4\pi n^2}{M_n} \sum_{\mathbf{k} \in S_n} E_{K,M}(\mathbf{k})$ where M_n is the number of wavevectors in the shell [124]. This produces a smoother spectrum.

1.3.5 Self-organisation, selective decay and dynamic alignment

Self-organisation is the spontaneous emergence of large-scale structure in a turbulent process. It acts in opposition to the Richardon-Kolmogorov forward energy cascade picture of HIT turbulence, in which energy flows from large scales to small scales.

Reverse spectral transfer is an intrinsic property of HIT, as was discovered by breaking apart the Navier-Stokes equations into the fundamental triadic interactions [136]. Large-scale velocity fields, however, never appear in HIT without some manipulation of the equations (for example, the addition of rotation, the reduction to two dimensional turbulence, or stringent controls on the helicity of every wavevector [16, 17]). What this means is that in HIT the portion of triadic interactions that move energy to larger scales is heavily outweighed by the portion that contribute to the forward energy cascade.

Magnetohydrodynamics in its most fundamental form behaves differently to hydrodynamics. It is becoming more and more apparent, thanks to the advance of high performance computing, that a net RST effect may occur in almost all situations, so long as the magnetic Reynolds and Prandtl numbers are above some threshold. The theoretical argument behind this emerged from the same approach of dissecting triadic interactions that was taken in hydrodynamics [79, 80]. The first observations of large-scale magnetic fields in homogeneous MHD came in conjunction with an inverse cascade of magnetic helicity in simulations of helical MHD [3, 4, 77, 110]. It seems to take relatively little effort to produce a large-

scale magnetic field. There is no doubt that the aforementioned alterations to the equations (rotation etc) deserve some credit for the effectiveness of the amplification of a magnetic field, but in my opinion they should be thought of as processes which enhance (rather than cause) large-scale magnetic fields, by favouring the interactions that produce RST.

The three magnetohydrodynamic ideal invariants (the total energy, the magnetic helicity and the cross helicity) control aspects of MHD systems, from the prevalence of RST to the (dimensionless) dissipation rate [37, 78, 82]. An explanation for this is called selective decay, which is the tendency for the fields to self-organise into a force-free state in which the magnetic helicity is maximal, or an Alfvénic state where the velocity and magnetic fields are fully aligned [18, 41]. The alignment of the fields weakens the turbulence, slowing down the decay of energy in unforced systems [18, 125]. These end states fall into distinct classes with their own characteristics [25].

Finally, the presence or absence of a background magnetic field affects the turbulent dynamics, and this is reflected in the scaling of the energy spectrum. In forced MHD with a strong background magnetic field, the theory of dynamic alignment predicts the field-perpendicular energy scaling $E(k_\perp) \propto k^{-3/2}$ [19]. This comes as a result of the tendency for the magnetic and velocity fluctuations to become aligned, with a more pronounced effect at smaller scales. However, dynamic alignment may also occur at the small scales in the absence of a guide field, since large-scale magnetic field fluctuations can play a similar role for the small-scale fluctuations as the guide field does [19]. In this thesis we consider only homogeneous MHD without a mean magnetic field.

1.4 Applications of MHD: from the core of the Earth to cosmic voids

Magnetic fields have been observed in galaxies, stars, planets and other astrophysical objects [12, 28, 113, 123, 137]. Their presence has even been noted in the spaces between galaxies [24, 101], bolstering a question which is a major unsolved problem in astronomy: do these large-scale fields have astrophysical origins (e.g. the expulsion of plasma from galaxies) or cosmological origins (e.g. magnetic fields generated at cosmological phase transitions)? Large-scale magnetic fields

feature in various other interesting problems such as the 11-year quasi-periodic solar magnetic field cycle, i.e. the flipping of the system-scale polarity of the Sun's magnetic field. This is likely to be driven by large-scale flows [92].

Laboratory and numerical experiments have been used in conjunction with each other to validate and build upon models of astrophysical and geophysical dynamos, e.g. [112]. These models can incorporate, for example, strong magnetic fields, convection and rotation. Simulations and experiments alike have reached, with difficulty, relatively extreme values of Re, Re_M and Pr_M, although the required parameter space for physical applications is still inaccessible. DNS simulations can simulate turbulence with Reynolds numbers of the order Re, $\mathrm{Re}_M \simeq 10^3$ which is only just turbulent enough to see an extended inertial range with a measurable spectral exponent. The magnetic Prandtl number is usually kept to one but has been pushed to 100 and 1/100, albeit by sacrificing the resolution of the data. The MHD equations are often modelled, rather than fully simulated, to cheapen the computational expense and allow higher Reynolds numbers to be reached. A troubling consequence of this is that many astrophysical simulations do not properly account for the magnetic Prandtl number, due to the use of numerical dissipation [22, 62, 63].

I will now briefly highlight some of the most interesting features and unsolved questions involving physical applications of MHD, with a view to making connections to results from studies of more fundamental MHD, i.e. turbulence which is homogenous, incompressible, and/or nonrotating.

1.4.1 The geomagnetic field

The molten core of the Earth is a turbulent, rotating, electrically-charged fluid which has kinetic and magnetic Reynolds numbers of around $\mathrm{Re} \simeq 10^8$ and $\mathrm{Re}_M \simeq 10^2$, putting its magnetic Prandtl number around $\mathrm{Pr}_M \simeq 10^{-6}$ [112, 113, 115]. Convection drives the magnetic field amplification, producing a dipolar field aligned 11° to the Earth's axis of rotation. The Earth's magnetic field plays a crucial protective role in diverting charged particles from the solar wind away from the planet; without the magnetic field the Earth would be barren, like the Moon. One of the most striking and unexplained features of the geomagnetic field is its polar reversals, which occur every few hundred thousand years.

To simulate the global magnetic field, the MHD equations are computed for

a thick, rotating, spherical shell, representing the molten outer core which surrounds the solid inner core. Current high-resolution simulations can achieve the required magnetic Reynolds number but not the magnetic Prandtl number. As well as this, the strength of the magnetic field and the Earth's Eckman number (a dimensionless parameter which compares viscous forces to rotational forces) are also generally outwith the regime accessible to simulations. Despite these differences, simulations are able to reproduce a similar dipolar field to that of the Earth [36, 132]. That being said, some features strongly depend on the dimensionless parameters, such as the ratio of the stretching and advection of the magnetic field, which decreases as a function of the magnetic Prandtl number [103]. Global models of the geodynamo tend to make use of LES, which calculate the MHD equations for the largest scales of the system. Applying results from DNS of the MHD equations strengthens the results of these global models through careful control and comparison of the individual factors underlying the problem. For example, the stretching and advection of the magnetic field - in other words, the redistribution of energy in the magnetic field and the transfer of energy from the velocity field to the magnetic field, respectively - have been well-studied in the context of homogeneous, incompressible MHD. Attempts to understand the stretching and advection of the geomagnetic field have called upon characteristics of homogeneous turbulence such as the Richardson-Kolmogorov energy cascade. Magnetic energy transfers in spectral space for models of the Earth's magnetic field were recently calculated using techniques borrowed from homogeneous MHD calculations [66]. They found, much like in homogeneous MHD, that the energy transfers are mostly local but that nonlocal magnetic-to-magnetic transfers away from the largest scale play a significant role. This directly connects the large-scale behaviour of the Earth's magnetic field, which is decreasing in intensity [50], to studies of homogeneous MHD turbulence.

1.4.2 The Sun

It is perhaps surprising that stellar and planetary magnetic fields share many similar features. The Sun's magnetic field is produced by dynamo action, as originally suggested by Larmor 99 years ago [31]. Its kinetic and magnetic Reynolds numbers are $\mathrm{Re} \simeq 10^{12}$ and $\mathrm{Re}_M \simeq 10^9$, so $\mathrm{Pr}_M \simeq 10^{-3}$ [74, 102]. The solar magnetic field is dipolar, closely aligned to the rotational axis, and experiences quasiperiodic polar field reversals, much like the geomagnetic field. The high Reynolds number of the Sun compared to the Earth means that its polar

reversals occur much more frequently: approximately every 11 years. Closely associated with the solar magnetic field are sunspots, small surface regions of intense magnetic activity, the number of which waxes and wanes following the polar reversal cycle. Observations of sunspots, and therefore the reversals of the solar field, have been taking place since the 1600s. The magnetic solar activity may influence the Earth's climate: observations of low levels of sunspots have been noted to coincide with periods of unusually cold weather on Earth [67].

Like the geomagnetic field, the existence of a large-scale magnetic field in an object with such chaotic small scale turbulence is not well understood, especially since the Sun's and the Earth's magnetic Prandtl numbers are small. Taking the base of the Sun's convective zone as the energy injection scale for turbulence and comparing it to the size of the Sun itself, there is clearly a large separation between length scales [65]. This makes it more difficult to capture all of the relevant scales in numerical experiments but it does hint at a connection to the existence of large-scale reverse spectral transfer in homogeneous, nonhelical MHD data [26]. In the homogeneous MHD community it is now fairly well-established that a separation between the scale of the system and the scale of energy injection is needed in computer simulations, if only just to make room for large-scale magnetic fields to grow. It makes sense that if there are more small-wavenumber modes for the main energy scale to couple to, in a context such as MHD where large-scale fields are prone to develop, then a large scale separation will allow more RST to take place.

Recently, energy and helicity spectra in active and quiet regions of the sun have been inferred from data from the Helioseismic and Magnetic Imager (HMI) on board the Solar Dynamics Observatory (SDO) [24], borrowing a technique from mean-field theory to remove cancellations incurred by opposite signs of helicity [27, 114]. As well as finding kinetic and magnetic energy spectra comparable to the Kolmogorov $k^{-5/3}$ scaling, the cross helicities were examined. In active regions the cross helicity was almost maximal, whereas it was low in the quiet sun. Since the steepness of the cross helicity spectrum may be an indicator of enhanced RST [140] and the Sun is thought to have $\mathrm{Pr_M} = 10^{-3}$ or smaller, it is important to consider how RST is affected by the combination of small $\mathrm{Pr_M}$ and high cross helicity.

The main point here is that although convection, rotation and other complexities are present in solar and geomagnetic turbulence, the global magnetic fields seem to arise as a result of a fundamental characteristic of MHD turbulence. Recent

high-resolution LES of the Sun have inspired speculation that the Lorentz force feedback on the velocity field from small magnetic scales is key to maintaining the large-scale solar magnetic field [65], but homogeneous MHD simulations in which the Lorentz force term was removed from the equations have still managed to produce RST [13], so the solution must be more complicated.

1.4.3 The solar wind

The Sun expels hot, fast-moving plasma from its atmosphere which expands like a bubble, encompassing the Solar System and beyond. Known as the solar wind, this low-density plasma can cause geomagnetic storms, disrupting power grids and communications on Earth. The region of space touched by the solar wind is called the heliosphere, and beyond this is the interstellar medium.

The solar wind is the only turbulent, high-Re_M fluid in which unintrusive *in situ* measurements can take place [29, 64, 130]. Since the 1970s, satellite missions have collected data on the solar wind all the way out to its furthest extent of approximately 100 AU (1 AU is roughly the distance between the Earth and the Sun) [18]. The most recent mission, the Parker Solar Probe, was launched a few weeks before the submission of this thesis and has a planned closest approach to the Sun of 0.046 AU, or approximately 10 solar radii. There is a wealth of useful solar wind data, even from the 1970s, that is still used in analyses today, thanks to the vast number of orders of magnitude (approximately eight) that can be measured.

The solar wind divides into two parts: a fast wind of outward-propagating Alfvén waves - by convention these are labelled by the $\mathbf{z}^+$ Elsässer variable - and a slow wind in which the Elsässer fields are only slightly imbalanced. The cross helicity of the fast solar wind decreases with distance from the Sun and eventually comes into balance, with both the total and residual energy spectra resembling the Kolmogorov spectrum. Although the solar wind is highly anisotropic and compressible, its spectral properties are somehow similar to homogeneous, incompressible MHD turbulence, for reasons which are not known.

1.4.4 Accretion disks

Most astrophysical objects are formed by accretion processes, which is when gaseous matter spirals towards a central object such as a star or black hole. As the matter collapses inwards it loses angular momentum and becomes turbulent due to an effect known as the magnetorotational instability [18], which is beyond the scope of this thesis. Kinetic-to-magnetic energy conversion is required to prevent the magnetic field of this conducting fluid from dissipating completely. Indeed, large-scale magnetic fields are observed in simulations, with approximately periodic field polarity reversals visible in spacetime diagrams as characteristic "butterfly" patterns [115]. The thickness of an accretion disk affects its ability to sustain the large-scale magnetic field that produces the butterfly patterns [63]: the thicker the disk, the less likely it is for self-organisation to occur. Similar effects have been found in more theoretical studies, such as simulations of nonhelical homogeneous MHD that found reverse spectral transfer when the separation between the system scale and the peak of the energy spectrum was large enough [13, 26].

The magnetic Prandtl number is thought to increase as a function of the disk thickness and therefore connects the problem of organised large-scale magnetic fields in accretion disks to the more general problem of the existence of critical magnetic Reynolds and Prandtl numbers for dynamo action. The increase of the magnetic Prandtl number as a function of accretion disk thickness supports the possibility of a transition from small-Pr_M in the outer parts of the disk to large-Pr_M in the central part. This would mean there is an order-unity Pr_M in accretion disks [10] which is within the accessible parameter space of direct numerical simulations. The accretion disk findings are another practical example of how basic characteristics explored in fundamental turbulence studies, such as the interplay between length scales, can manifest in complicated real-life applications.

1.4.5 Cosmological magnetic fields

Not only are magnetic fields observed in astrophysical objects such as those mentioned above, but there is mounting evidence for the presence of large-scale magnetic fields even in reasonably empty regions of space known as cosmic voids. If a cosmological-scale magnetic field exists then it may have been generated from some primordial epoch such as during inflation or the electroweak phase

transition. Such a field would need to be sustained over extremely long time periods so many models focus on helical fields, which facilitate reverse spectral transfer. This, however, does not rule out nonhelical cosmic magnetic fields: firstly, even fields with initially small values of magnetic helicity tend to evolve into fully-helical fields and secondly, nonhelical MHD can also exhibit reverse spectral transfer under the right conditions [26, 118].

Data from the *Planck 2015* measurements of the cosmic microwave background placed upper bounds on several possible types of primordial magnetic fields based on how they would affect its anisotropies and polarization [105]. These upper bounds are of the order of 10^{-9}G. Better yet, recent measurements of gamma rays from stacked blazar data indicate an intergalactic magnetic field of strength *greater than* 10^{-16}G, strengthening the case for a cosmological magnetic field [33, 101, 133].

The Cosmological Principle (that the Universe is homogeneous and isotropic) means that homogeneous MHD is particularly well-suited to the study of cosmic magnetic fields. The MHD equations for a flat, expanding universe can be rescaled using the scale factor $a(t)$ which measures the expansion of the Universe. These rescaled equations end up being the same as the nonexpanding MHD equations [23]. Most theoretical results involving MHD dynamos are for incompressible turbulence, which is applicable for planetary and stellar dynamos but not automatically so for interstellar and intergalactic media. Fortunately, comparisons between compressible and incompressible MHD simulations find qualitatively similar behaviour of the kinetic-to-magnetic energy ratios and energy spectra at different values of magnetic Prandtl number [48, 126]. An important next step would be to quantify the difference in efficiency that compressibility has on energy transfers in MHD with astrophysical conditions. Estimates put the magnetic Prandtl number of the early Universe at $\mathrm{Pr}_M \simeq 10^7$ with $\mathrm{Re}_M \simeq 10^10$ and $\mathrm{Re} \simeq 10^3$ [118].

In the same way that inflated quantum fluctuations are thought to have seeded our galaxies, inflation provides a setting for cosmological-scale magnetic fields to have been generated [32, 131]. If this is the case, then today's magnetic fields could encode secrets of the early Universe, including, for example, the duration of inflation itself, which is not predicted by any other theory [69]. Other possible epochs during which cosmological-scale magnetic fields may have been generated include the electroweak phase transition and the quantumchromodynamic (QCD) phase transition [71]. In the former case, magnetic fields may be generated by

shocks and in the latter, through interactions with axion dark matter, should it exist. Either way, a field generated by one of these means should have a present-day strength that lies within the current constaints from CMB and blazar observations [70, 84, 94]. In the near future, telescope arrays and gravitational wave detectors will be able to pinpoint the strength, scale and helicity of the cosmic magnetic field. Each proposed magnetogenesis theory leads to a field with a specific signature and is built around current major problems in modern cosmology, including for example, inflation, dark matter and the matter-antimatter asymmetry, and is thus an important probe for these unanswered questions.

Chapter 2

Shaken or stirred: a comparison of large-scale forcing functions

2.1 Introduction

The advent of high performance computing has caused a rapid growth in the study of turbulence. Direct numerical simulations (DNS) are a computationally expensive tool which allows us to follow the exact evolution of a turbulent flow without introducing any modelling. However, it is often useful to inject energy into a turbulent system to compensate for the energy lost through dissipation, and in these forced simulations, a decision has to be made about the method of energy injection. Once a balance is achieved between the energy lost and the energy injected, the system's statistical properties can be studied.

A wide range of approaches to forcing homogeneous turbulence simulations has been used over the years. Most often these involve injecting energy into the smallest wavenumbers, i.e. the largest length scales, with or without introducing some random component (see e.g. [6, 47, 139]). Different forcing methods have different advantages. A deterministic force could be seen as more physical but stochastic forces may provide better control over energy and helicity input. Another example is that a deterministic forcing may produce fluctuations on larger time scales than a stochastic forcing and so may require a longer run-time to obtain converged statistics, despite being more efficient computationally [139].

The well-established Richardson-Kolmogorov cascade view of hydrodynamics

turbulence implies that the way that turbulence is generated should be largely irrelevant at the intermediate and small scales. This theory doesn't hold up as well in MHD which experiences higher quantities of nonlocal energy transfer and is prone to spontaneous self-organisation. Nonetheless it is often taken to be true, particularly in nonhelical MHD. Interestingly, it was found that self-organised states can be obtained when both the velocity and the magnetic fields are forced in a nonhelical way, depending on the time-correlation of the forcing [38]. The less often the phase was randomised, the more the cross helicity and magnetic helicity would build up, leading to self-organisation. The Archontis dynamo, in which the velocity field is forced in a nonhelical way, is also known to introduce large values of cross helicity. Another feature of the Archontis dynamo is that (in the case where the magnetic and kinetic Reynolds numbers Re_M and Re are equal) the steady-state magnetic and kinetic energy are almost in equipartition [8, 30, 43, 57]. It is important to be sure that effects such as these are independent of the specific implementation of the forcing, especially since MHD has many cosmological, astrophysical and industrial applications and relies heavily on results from numerical simulations. The importance of understanding how independent the turbulence properties are of the forcing function has been underpinned by the above discussion. So far, there has been no systematic study that examines the effect of different forcing functions in MHD.

In this chapter we investigate the evolution of homogeneous, incompressible MHD turbulence without a mean magnetic field, subject to three different types of mechanical forcing functions which aim to represent the range of forcing methods used in the literature. Specifically, we use: one which uses the large-scale velocity field as a forcing function, a nonhelical random force defined by using time-varying helical basis vectors, and a nonhelical static sinusoidal force. In section 2.2 we give details of our simulations, including the three forcing routines. In section 2.3 we examine the time evolution of the three ideal invariants (energy, magnetic helicity and cross helicity), the time-averaged energy and cross helicity spectra, the energy ratios and the dissipation ratios. As we will show, the magnetic helicity remains close to zero in all cases but the sinusoidal method of energy injection has a tendency to introduce cross helicity into the system. Indeed, our results for sinusoidally-forced simulations with identical parameters and different initial conditions show large variations in the normalised cross helicity over long time periods.

2.2 Definition of forcing functions

Three types of forcing function were used: negative damping (ND), adjustable helicity forcing (AHF) and sinusoidal forcing (SF). They are defined as follows:

2.2.1 Negative damping

The negative damping function uses the large-scale velocity field as a forcing function. It was first developed as a way to avoid introducing further randomness into an already random system [85] and is commonly used in hydrodynamic simulations [68, 72, 73, 83, 88]. The function is

$$\mathbf{f}(\mathbf{k},t) = \begin{cases} \frac{\varepsilon_i \mathbf{u}(\mathbf{k},t)}{2E_{K,k_f}(t)} & \text{if } 1 \leq |\mathbf{k}| \leq k_f \ , \\ 0 & \text{otherwise,} \end{cases} \tag{2.1}$$

where $E_{K,k_f}(t) = \int_1^{k_f} E_K(k,t)dk$ is the kinetic energy contained in the forcing range $[1, k_f]$ and ε_i is an adjustable parameter. The rate of energy injection is $\langle \mathbf{u} \cdot \mathbf{f} \rangle = \int d\mathbf{k}\ \mathbf{u}(\mathbf{k}) \cdot \mathbf{f}(-\mathbf{k}) = \varepsilon_i$ which will be equal to the mean total dissipation rate $\varepsilon = \varepsilon_M + \varepsilon_K$ during the steady state. We chose our fields' initial conditions to have negligible kinetic, magnetic and cross helicity and therefore one might expect the fields to remain nonhelical throughout their evolution, although the actual helicity injection cannot be controlled. The variation of cross helicity in MHD subject to negative damping was explored to some extent in [116]. The forcing type has been well-used, but nevertheless, it was recently found that, in hydrodynamics, at low Reynolds numbers, negative damping can induce self-ordering effects due to poor control of kinetic helicity injection [83, 88].

2.2.2 Adjustable helicity forcing

The second type of forcing considered uses a helical basis composed of eigenvectors of the curl operator:

$$\mathbf{f}(\mathbf{k},t) = \begin{cases} A(\mathbf{k})\mathbf{e}_1(\mathbf{k},t) + B(\mathbf{k})\mathbf{e}_2(\mathbf{k},t) & \text{if } 1 \leq |\mathbf{k}| \leq k_f \ , \\ 0 & \text{otherwise,} \end{cases} \tag{2.2}$$

where $\mathbf{e}_1 \cdot \mathbf{e}_2^* = \mathbf{e}_1 \cdot \mathbf{k} = \mathbf{e}_2 \cdot \mathbf{k} = 0$ and $\mathbf{e}_1$ and $\mathbf{e}_2$ are unit vectors which statisfy $i\mathbf{k} \times \mathbf{e}_1 = k\mathbf{e}_1$ and $i\mathbf{k} \times \mathbf{e}_2 = -k\mathbf{e}_2$. At each forcing time step, for every vector $\mathbf{k}$ with magnitude $1 \leq |\mathbf{k}| \leq k_f$, a corresponding random perpendicular unit vector is generated and used to construct the helical basis; thus the basis is changed every time the forcing function is called. $A(\mathbf{k})$ and $B(\mathbf{k})$ are complex parameters which can be adjusted to control the helicity of the forcing [21]. In our simulations we set the kinetic helicity to zero, so the forcing was explicitly nonhelical. This type of forcing has been widely used [16, 21, 22, 86, 100].

2.2.3 Sinusoidal forcing

The sinusoidal forcing we used is deterministic and nonhelical, implemented in real space:

$$\mathbf{f}(\mathbf{x}) = C \sum_{k=1}^{k_f} \begin{pmatrix} \sin(kz) + \sin(ky) \\ \sin(kx) + \sin(kz) \\ \sin(ky) + \sin(kx) \end{pmatrix} , \tag{2.3}$$

where C is an adjustable constant. This forcing type was used in [38]. It is a nonhelical analogue of the well-known ABC forcing, which is fully helical [34, 54–56, 95], and is similar to the Archontis dynamo, $\mathbf{f}(\mathbf{x}) = (\sin(z), \sin(x), \sin(y))$ [30].

2.3 Results

Run ID	N	ν	Re	k_{max}/k_η	k_{max}/k_ν	ρ_M	ρ_K	ρ_c	σ_c
AHFa	1024	0.000625	1085	2.49	3.13	-0.00011	0.0014	-0.012	-0.010
NDa	1024	0.000625	1293	2.60	3.26	0.0036	0.040	0.063	0.057
SFa	1024	0.000625	1524	2.61	3.27	0.016	-0.0034	0.10	0.084
AHFb	512	0.0008	742	1.50	1.88	0.0077	0.00063	0.026	0.023
NDb	512	0.0008	994	1.56	1.96	-0.0043	0.045	-0.035	-0.030
SFb	512	0.0008	1190	1.55	1.94	-0.0046	0.0027	-0.16	-0.13
AHFc	512	0.001	609	1.77	2.20	-0.0038	-0.0072	0.012	0.010
NDc	512	0.001	803	1.85	2.28	-0.029	-0.00015	0.22	0.21
SFc	512	0.001	940	1.85	2.31	0.0022	0.00076	-0.012	-0.010
AHFd	256	0.0015	374	1.25	1.51	-0.0039	0.0037	-0.0084	-0.0069
NDd	256	0.0015	535	1.25	1.53	-0.0046	0.044	-0.093	-0.080
SFd	256	0.0015	618	1.25	1.55	0.011	-0.0046	-0.029	-0.025
AHFe	256	0.002	308	1.55	1.82	0.0069	-0.0098	-0.0062	-0.0049
NDe	256	0.002	410	1.56	1.88	-0.013	0.059	0.0010	0.00081
SFe	256	0.002	541	1.45	1.76	-0.0037	0.0015	0.013	0.010
AHFf	128	0.005	127	1.61	1.61	-0.0044	-0.0019	-0.0088	-0.0060
NDf	128	0.005	171	1.58	1.72	0.0036	-0.041	0.024	0.018
SFf	128	0.005	211	1.46	1.65	0.021	-0.014	0.10	0.080

Table 2.1: Table of basic parameters including the forcing type, number of grid points N^3, viscosity ν, integral-scale and Taylor-scale Reynolds numbers Re and Re_λ respectively, resolution k_{max}/k_η and k_{max}/k_ν defined with respect to the magnetic and velocity fields, relative magnetic helicity ρ_M, relative kinetic helicity ρ_K, and two definitions of relative cross helicity ρ_c and σ_c (equations (1.11) and (1.12)). The values were time-averaged over the duration of the steady state. AHF stands for adjustable helicity forcing, ND for negative damping, SF for sinusoidal forcing.

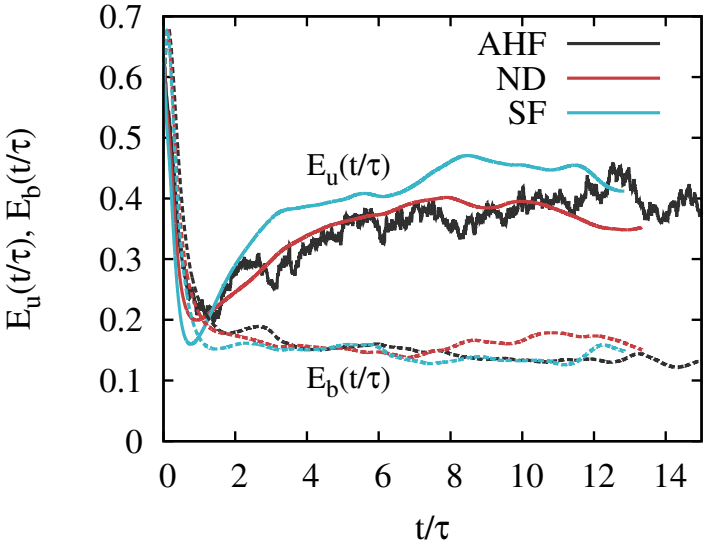

Figure 2.1: Evolution of kinetic energy (solid lines) and magnetic energy (dashed lines) for runs AHFa, NDa and SFa. τ is the steady state large eddy turnover time.

2.3.1 Energy evolution

I will describe our results using the $\nu = 0.000625$ (AHFa, NDa, SFa) simulations to demonstrate points, since they attained the highest Reynolds numbers in our tests (see Table 2.1. The data is also publicly available online [127]). Using these simulations, which are representative of the other simulations we ran, we will highlight features of the three forcing functions.

The analysis focuses on various properties of the forced systems while in a statistically steady state. This allows us to look at time-averaged samples of data taken during that period. Figure 2.1 shows the time evolution of the kinetic and magnetic energies corresponding to runs AHFa, NDa and SFa. An initial transition period precedes the fully-developed statistically steady turbulent state, where the energy injected equals the energy dissipated. We began taking measurements after the transient initial behaviour had passed and both the kinetic and magnetic energies were fluctuating around a constant value. The AHF kinetic energy evolution, as seen in Fig. 2.1, is more erratic than the other two forcing types. This is due to the random nature of the forcing function, as described in section 2.2.2, which causes rapid changes in the amount of energy injected. The time scale was normalised by the steady state large eddy turnover time $\tau = U/L$, where U is the root-mean-square velocity, L is the integral scale and $E_K(k)$ is the steady state kinetic energy spectrum, as defined in the

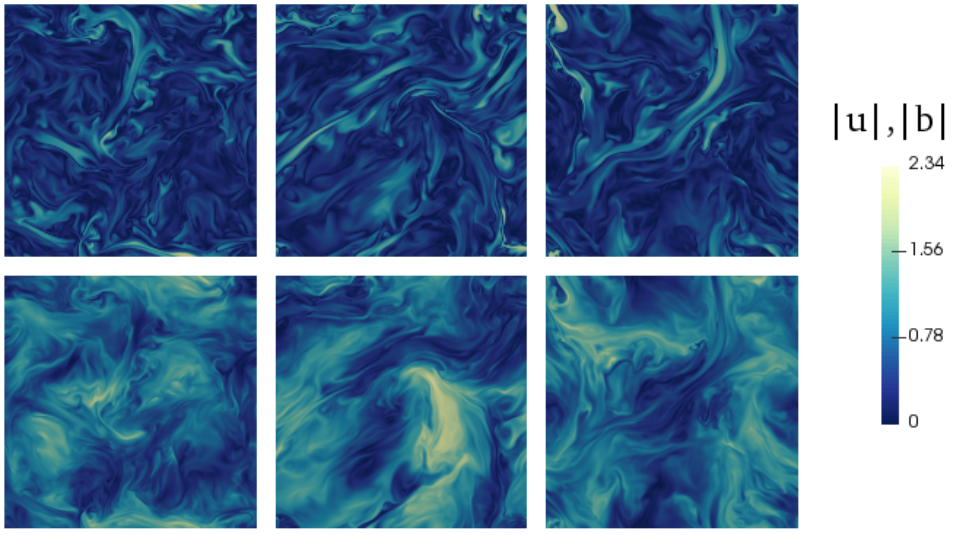

Figure 2.2: Visualisation of a two-dimensional slice of the magnitudes of the magnetic (top) and velocity (bottom) fields in the AHFa (left), NDa (middle) and SFa (right) cases.

Introduction. In an isotropic system, $U^2 = \langle u_i^2 \rangle$ for any direction i, so the total kinetic energy $E_K = 3U^2/2$. All simulations lasted for 100 units of simulation time, corresponding to approximately 30 to 40 large eddy turnover times, except the simulations run on 1024^3 points, which ran for about 40 units of simulation time. The AHF runs generally had a slightly smaller value of τ, meaning that the injected energy was transferred to the smaller scales at a faster rate.

I will use both the integral scale Reynolds number $\mathrm{Re} = UL/\nu$ and the Taylor-Reynolds number $\mathrm{Re}_\lambda = U\lambda/\nu$ as metrics to measure the turbulence, since the integral scale Reynolds number is associated with the forcing scales while the Taylor Reynolds number characterises the turbulence at intermediate scales. The Taylor microscale, λ, is defined in section 1.3.3

Two-dimensional slices of the magnitudes of the fields $|\mathbf{u}|$ and $|\mathbf{b}|$ from the AHFa, NDa and SFa simulations at a point in time during the steady state are shown in Fig. 2.2. These slices are representative of the general structure of the fields throughout the steady state time frame. The time-averaged Reynolds numbers are moderately separated: $\mathrm{Re} = 1085, 1293$ and 1524 respectively, but the fields do not differ greatly and exhibit the same level of detail in the small scales. This is to be expected as they have similar dissipation wavenumbers k_η and k_ν (see Table 2.1). These visualisations demonstrate that, although the forces have very different functional forms, the physical appearance of the fields is similar. Overall

we see that all three forces are capable of producing physically-alike steady state behaviour in the same time frame.

2.3.2 Definitions of relative cross helicity

In section 1.2.2 two ways of defining the relative cross helicity were introduced: ρ_C, based on the alignment between the magnetic and velocity fields, and σ_C, the ratio of two ideal invariants. The time evolution of these quantities and their time-averaged spectra from run SFa are shown in Fig. 2.3.

As can be seen in the figure, the time evolution of the two metrics follow a similar trajectory, with σ_c remaining close to, but less than, ρ_c. The largest separation between ρ_c and σ_c occurs during a period when the difference between the kinetic and magnetic energies was greatest; this effect is apparent from the definitions of ρ_c and σ_c given in equations (1.11) and (1.12). When the kinetic and magnetic energies are in equipartition the two quantities coincide.

Figure 2.3b shows the time-averaged cross helicity spectra corresponding to the two definitions in equations (1.11) and (1.12)

$$\rho_c(k) = \frac{H_c(k)}{2E_M(k)^{1/2}E_K(k)^{1/2}} \ , \tag{2.4}$$

$$\sigma_c(k) = \frac{H_c(k)}{E_M(k) + E_K(k)} \ , \tag{2.5}$$

where $H_c(k) = \int_{|\mathbf{k}|=k} d\mathbf{k}\ \hat{\mathbf{u}}(\mathbf{k}) \cdot \hat{\mathbf{b}}(-\mathbf{k})$ is the cross helicity spectrum. We see that $\rho_c(k)$, which is normalised by $2E_M(k)^{1/2}E_K(k)^{1/2}$, is more sensitive to the ratio of kinetic and magnetic energy than $\sigma_c(k)$ is. Because of this, at the forcing scale, where the kinetic energy is much greater than the magnetic energy, the denominator becomes small for $\rho_c(k)$ and not for $\sigma_c(k)$. Thus $\rho_c(k)$ has a large peak which is absent from the $\sigma_c(k)$ spectrum. The difference in the low-k relative cross helicity spectra occurs consistently across simulations with different forcing functions. This effect, however, could cause data to be misinterpreted, especially between separate groups of researchers.

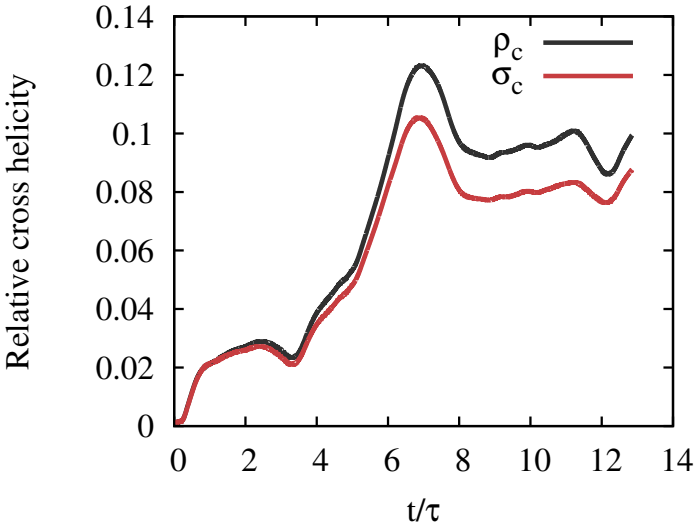

(a)

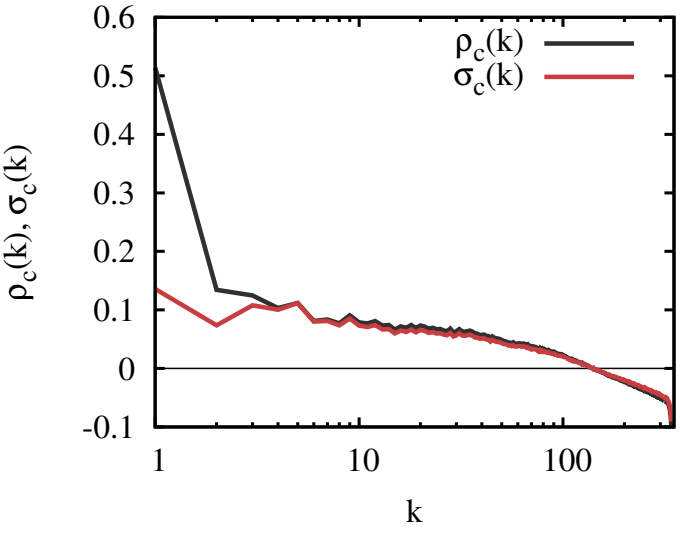

(b)

Figure 2.3: (a) Time evolution and (b) spectra of the two definitions of relative cross helicity (equations (1.11) and (1.12)) for run SFa. Note the logarithmic scale on the x-axis only in Fig. 2.3b.

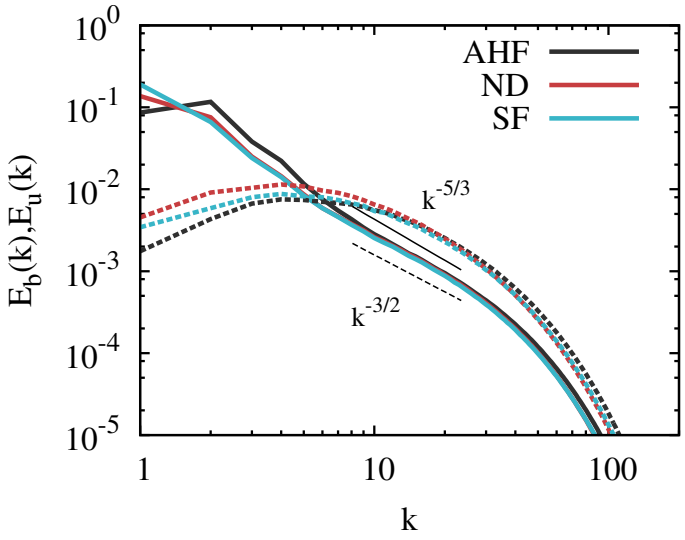

(a)

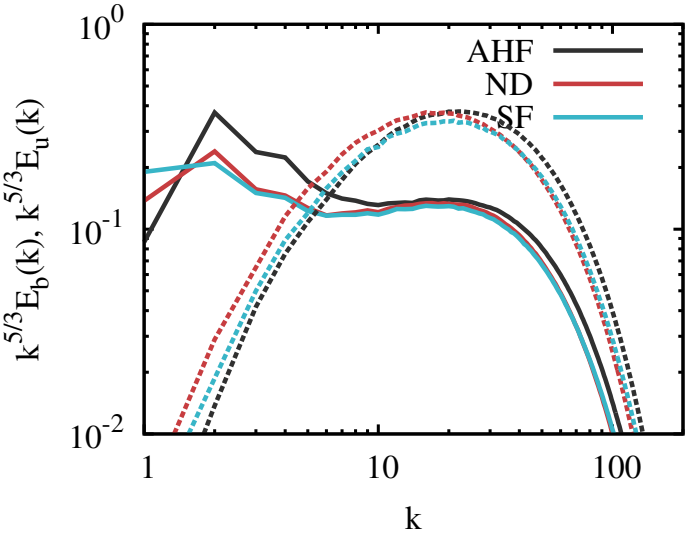

(b)

Figure 2.4: (a) Kinetic and magnetic energy spectra (solid and dashed lines respectively) and (b) compensated kinetic and magnetic energy spectra for runs AHFa, NDa and SFa.

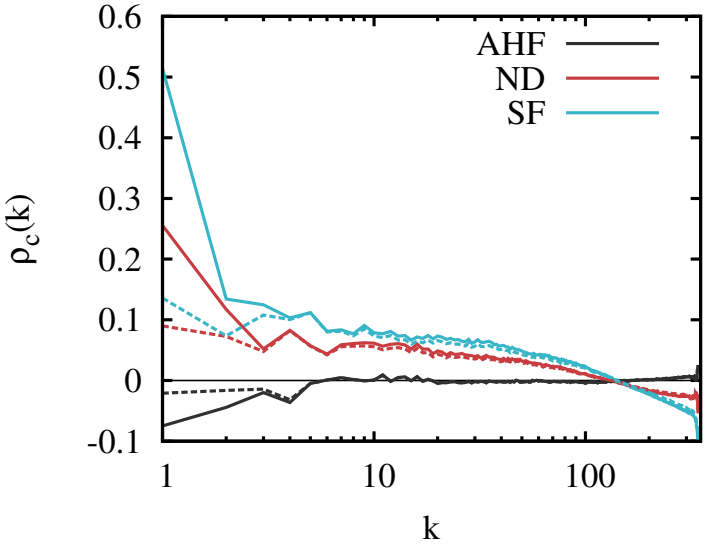

Figure 2.5: Relative cross helicity spectra for runs AHFa, NDa and SFa. Note the logarithmic scale on the x-axis only.

2.3.3 Comparison of energy and cross helicity spectra

Having identified the onset of the statistically steady state, we can examine the time-averaged energy spectra (Fig. 2.4a). The spectra coincide in a small inertial subrange but spread out slightly at the large and small scales. All of our simulations had the same low-k behaviour, with the ND and SF runs having a peak at $k = 1$ and the AHF types peaking at $k = 2$.

Both $k^{-5/3}$ and $k^{-3/2}$ scalings have been indicated in Fig. 2.4a. The compensated kinetic and magnetic energy spectra are shown in Fig. 2.4b. As can be seen in these figures, the power-law range of the kinetic energy spectrum is too short to distinguish between the two scalings. This highlights that we still have to exercise caution in making measurements of this kind, and that larger simulations with a more obvious inertial range are still needed. The inertial range for the magnetic energy spectrum is even less clear. It is plausible that in order to see a clearer scaling we would need to inject energy directly into the magnetic field; this is also indicated by the results of [1] in which the ratio of magnetic to mechanical forcing was varied in generally nonhelical simulations. However, our results focus only on mechanical forcing, as magnetic forcing is known to induce other effects such as large-scale self-organisation [38]. The runs with smaller Reynolds numbers have steeper energy spectra, presumably because of the enduring problem of the lack of separation between forcing scales and dissipation scales in direct numerical

simulations. The steeper slope in the lower range of run AHFa compared to NDa and SFa could thus also be a finite Reynolds number effect, since the adjustable helicity forcing consistently produced simulations with lower Reynolds numbers for a given viscosity.

The magnetic and kinetic helicity generally remained negligible (see Table 2.1), however the cross helicity in some simulations was prone to large fluctuations, yielding time-averaged values of ρ_c as large as 0.22 (Run NDc). We have seen that $\rho_c(k)$ is peaked at the forcing scales (as shown in Fig. 2.5) and therefore conclude that it has been injected by the forcing function. Interestingly, there also tends to be a build-up in the normalised cross helicity at small scales with the opposite sign to the build-up at the large scales.

Owing to its effect on the scaling exponents of the energy spectra in MHD in the presence of a magnetic guide field [104], the behaviour of $\sigma_c(k)$ has been studied extensively in solar wind data [108], numerical simulations [14] and theoretically [107]. The observational studies found $|\sigma_c(k)|$ to be constant in the inertial subrange provided that the average value was large, while states with small mean cross helicity suffered from uncertainties in the measurements.

Here, for steady states with low but non-negligible $\rho_c(k)$ and $\sigma_c(k)$, we consistently find a tendency to compensate the force-induced alignment between $\mathbf{u}$ and $\mathbf{b}$ at small k (large scales) mostly at large k (small scales). The relative cross helicity at a given scale is related to the scale-dependent alignment angle [19, 108]. However, provided the alignment angle is small, its scale dependence does not enforce a scale dependence of the relative cross helicity [108]. In view of the aforementioned results on scale-independence of $\sigma_c(k)$ for high cross helicity states in unbalanced MHD with a guide field, the approximately linear scaling observed here may point to a more complicated situation for low cross helicity states, which merits further investigation in its own right. Finally, we do not find a noticeable effect of small values of cross helicity on the scaling of the energy spectra in our data.

2.3.4 Energy and dissipation ratios

In our tests, only the velocity field was forced and so the magnetic field was sustained through the transfer of kinetic to magnetic energy, i.e., dynamo action. It is useful to know how efficient the dynamo is at sustaining the magnetic field,

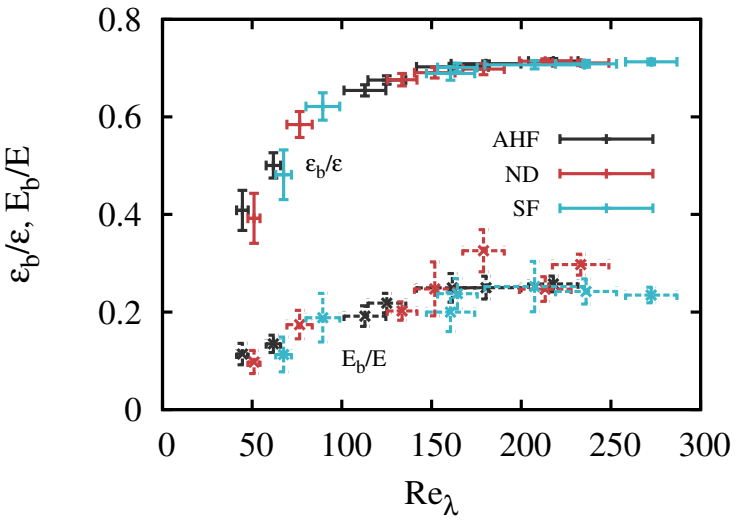

Figure 2.6: Fraction of magnetic dissipation $\varepsilon_M/\varepsilon$ (plusses) and magnetic energy E_M/E (crosses) as a function of Taylor Reynolds number. The error bars are the standard deviation.

which had initial conditions such that it was in equipartition with the velocity field at $t = 0$. Figure 2.6 shows the ratios E_M/E and $\varepsilon_M/\varepsilon$ as a function of Taylor-scale Reynolds number. The Taylor-scale Reynolds number is used instead of the integral-scale Reynolds number because we are interested in comparing the effects of the forces at smaller scales than the forcing range. The measurements of E_M/E and $\varepsilon_M/\varepsilon$ follow a clear trend regardless of the way in which the kinetic energy was injected. In particular, the magnetic dissipation fraction asymptotes quickly to $\varepsilon_M/\varepsilon \simeq 0.71$. This is in agreement with other results for nonhelical simulations with unity magnetic Prandtl number [22, 60, 78]. The magnetic energy fraction displays slightly more erratic behaviour, particularly in run NDc. The scatter is expected because the energy is dominated by the more volatile forcing scales, while the dissipation takes place at small scales. We conclude that the energy transfer and dissipation produced by each type of force is consistent. The efficiency of the nonhelical dynamo is independent of the implementation of the large-scale mechanical forcing.

2.3.5 Injection of ideal invariants

The total energy, magnetic helicity and cross helicity are conserved in the ideal (dissipationless) limit. It is therefore desirable for the helicities to remain approximately constant during a statistically steady state at high Re and Re_M.

The total energy in the system fluctuates around a constant value as energy is injected and dissipated and we expect the same from the other two ideal invariants. The initial conditions in our simulations have zero magnetic and cross helicity. The time evolution of relative magnetic helicity and cross helicity is shown in Fig. 2.7. The mean relative magnetic helicity remains within one standard deviation of zero in all cases, irrespective of the chosen forcing method. This could be expected since the magnetic field is not directly forced and should therefore be less susceptible to large variations.

The relative cross helicity, on the other hand, has the tendency to deviate from zero in some cases, with large fluctuations lasting for long times. This is particularly prevalent in the ND and SF runs, with fluctuations up to $\rho_c \simeq 0.3$ at times. Since ND feeds the velocity field back into itself, small fluctuations in cross helicity could be amplified, leading to a runaway effect at large scales. In Fig. 2.5 we saw that the relative cross helicity is peaked at the forcing scales, so it is clear that the growth of cross helicity is connected to the forcing. To guarantee negligible injection of cross helicity, the alignment between $\mathbf{f}$ and $\mathbf{b}$ (and when a magnetic force $\mathbf{f_b}$ is present, the alignment between $\mathbf{f_b}$ and $\mathbf{u}$) should remain negligible. The unusually large fraction of magnetic energy in Run NDc, as seen in Fig. 2.6, could be connected to the presence of high cross helicity. We will come back to this point in the next section.

The influence of intermediate values of cross helicity is not well understood, although it is known that systems with nonzero cross helicity can tend towards an Alfvénic state in which the cross helicity is maximal [59]. One of the findings of this study which has not been anticipated in the literature is that helicity can unexpectedly enter the system through certain forcing functions. Thus it is of practical importance to monitor and control its injection.

2.3.6 Comparison of repeated simulations

Generally when using DNS we make the assumption of ergodicity, that is, that in stationary turbulence the time-averaged values from one simulation are equivalent to ensemble-averaged values where the ensemble consists of many simulations. Thus for any set of parameters, usually only one simulation is performed and statistics are obtained by averaging over snapshots in time once the system has reached a steady state. This is the approach we took in the preceeding section. However, we found significant variations in cross helicity over time which

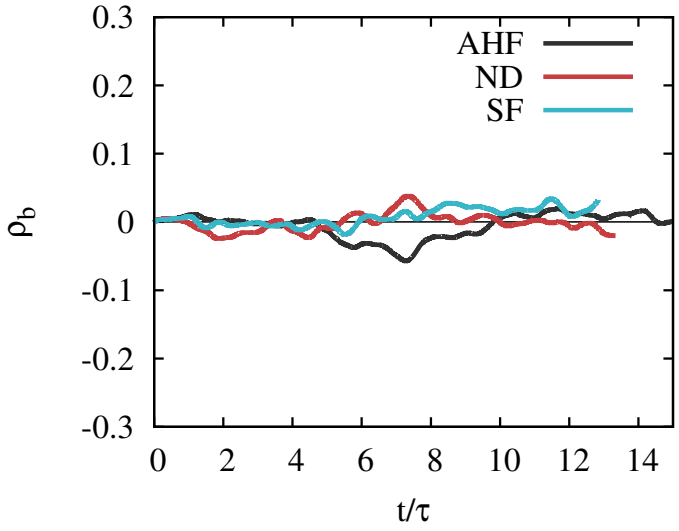

(a)

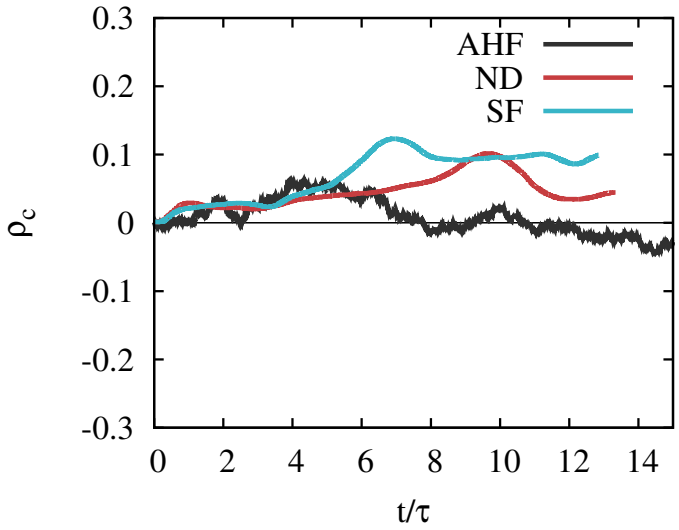

(b)

Figure 2.7: Evolution of (a) relative magnetic helicity and (b) relative cross helicity for runs AHFa, NDa and SFa. τ is the time-averaged large eddy turnover time. Note that the y-axis extends to ± 0.3 but the maximum possible values are 1.

prompted us to question how valid the ergodic principle is in situations where the injection of helicities cannot be controlled. Furthermore, one might expect that the fluctuations of the ideal invariants would decrease as we increase the Reynolds number, since we are increasing the number of interactions at each length scale, but this does not seem to be the case in our tests. Large fluctuations in cross helicity alter the behaviour of a flow, for example in Run NDc, which had an average relative cross helicity $\rho_c = 0.22$ and a larger than expected energy fraction E_M/E.

To test the variability of the cross helicity and its effect on the distribution of energy between the two fields, we ran an ensemble of 20 simulations for each forcing type on a 128^3 grid with viscosity $\nu = 0.008$. The time-averaged Reynolds numbers and relative cross helicity ρ_c are shown in Table 2.2. In all cases, the time-averaged Reynolds numbers stayed in a close range. The relative cross helicity, however, was less consistent, particularly in the SF ensembles. We plotted the time evolution of the magnetic energy fraction against the relative cross helicity for all our simulations to explore the possibility of a connection between the two quantities (Fig. 2.8). We see further evidence of the variability of cross helicity in the SF cases and also what seems to be a tendency for the magnetic energy fraction to increase as the magnitude of cross helicity increases. This observation for fairly low levels of cross helicity is reminiscent of the behaviour of the Archontis dynamo, which produces high levels of cross helicity and saturates with the velocity and magnetic fields approximately in equipartition [8]. Rapid variations in cross helicity have also been observed in MHD shell models subject to a constant mechanical force [52]. Since the SF is static and the AHF is randomised at every time step, the behaviour we see also echoes that of [38], who explored the effect of the correlation time of a kinetic and magnetic force on the helicities. Their results showed that the less often the force was randomised, the more the cross helicity was likely to grow. We see a similar effect here, although we only forced the velocity field.

The results of this section suggest that the ergodic principle does not hold well when the fluid is subject to the static sinusoidal forcing, as the relative cross helicity can vary significantly from one run to another, which affects aspects of the system such as the energy distribution. This is also likely the case with ND to a lesser degree. The concept of nonuniversality is of interest here, since two simulations with large average values of cross helicity of opposite sign would surely not behave in the same way as a system with zero cross helicity,

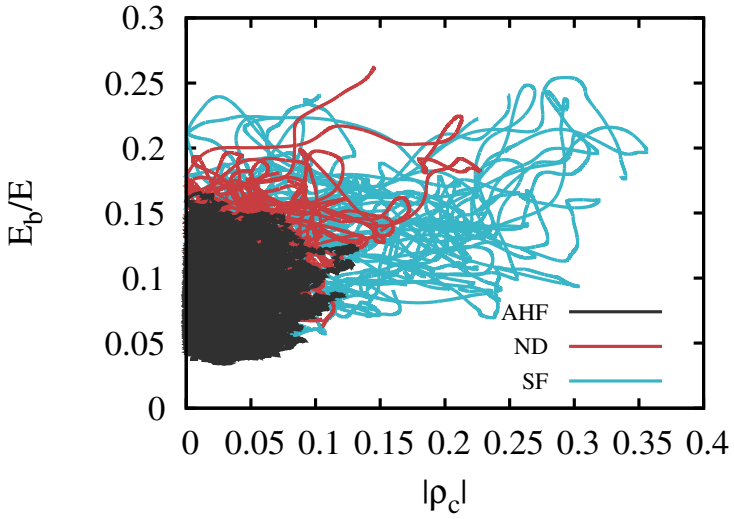

Figure 2.8: Magnitude of relative cross helicity versus the fraction of magnetic energy E_M/E at each point in time of the steady-state ensembles with $\nu = 0.008$.

Type	Re	Re_λ	$\lvert\rho_c\rvert$	#
AHF	$80 - 87$	$44 - 46$	$7.41 \times 10^{-6} - 0.0256$	20
ND	$100 - 111$	$52 - 57$	$0.000686 - 0.0561$	20
SF	$132 - 141$	$66 - 70$	$0.00111 - 0.193$	20

Table 2.2: The range of time-averaged quantities (integral-scale Reynolds number Re, Taylor-scale Reynolds number Re_λ and relative cross helicity magnitude $|\rho_c|$) from ensembles of each of the three forcing types with $\nu = 0.008$ on 128^3 grid points.

despite the ensemble-averaged values being small. So perhaps the solution is simply to monitor the ideal invariants carefully and be wary of large variations. Nevertheless, the AHF reliably maintains small values of cross helicity and so these extra considerations are not required.

2.4 Conclusions

In this chapter we explored the similarities and differences of three different types of mechanical forcing function in homogeneous, incompressible magnetohydrodynamic simulations without a mean magnetic field. These forces were negative damping, a random adjustable helicity forcing in which the kinetic helicity input was set to zero, and a nonhelical deterministic sinusoidal forcing. From a practical point of view, the AHF was least effective at reaching large Reynolds numbers at a given resolution but most effective at maintaining small values of cross helicity. It also produced slightly different energy spectra compared to the other two forcing types. We found that all three forces produce a steady state in a similar amount of simulation time, with reasonable agreement of dynamo efficiency, interpreted via the energy and dissipation fractions.

We considered the fluctuations of energy, relative magnetic helicity and relative cross helicity over time since these three quantities are the ideal invariants in MHD. The magnetic helicity had only very small fluctuations in all three cases, whereas the cross helicity was more erratic. In some simulations - particularly the ND and SF types - the cross helicity had large, long-term deviations from zero, although the deviations were not large enough to cause the system to become fully Alfvénic. However, it led us to question the validity of ergodicity when using forcing functions which are prone to causing build-ups in cross helicity, since large variations of cross helicity influence the development of the flow. We found that there may be a tendency for the magnetic energy fraction to increase as the relative cross helicity increases, but the cross helicity fluctuations were not large enough to be able to say this definitively. It is important to make sure that the rate of injection of cross helicity is small. Concerning the scale-by-scale behaviour of the cross helicity measured through the relative cross helicity spectrum, a response to large-scale cross helicity injection in the form of a mostly small-scale compensation effect was observed. Unlike high cross helicity states such as those observed in the solar wind [108], the relative cross helicity spectra measured for our low cross helicity states are not scale-independent in the inertial

subrange. This difference and the possible effect of a guide field on cross helicity dynamics perhaps merits its own systematic investigation.

In summary, the present analysis has highlighted some of the subtle problems with the control of ideal invariants in DNS of mechanically forced MHD turbulence. Future work could involve carrying out more simulations with higher Reynolds numbers to further assess the effect on fluctuations of the ideal invariants. The AHF simulations had the best control of cross helicity injection, presumably due to the stochastic nature of the force. Adding a random phase to the SF function might therefore help to minimise the cross helicity input. It would also be interesting to study flows which are forced magnetically, with or without mechanical forcing, particularly in light of the results on self-organisation in [38].

While we cannot make any absolute statements about the equivalence of all forcing functions at large Reynolds numbers, we have at least confirmed that three different implementations, typical of the kind generally used in MHD simulations, produce flows with similar characteristics, albeit with fairly significant deviations at the forcing scales. Forcing functions which do not control the injection of helicities should be monitored carefully. However, in the case of kinetic-only forcing which we have focussed on, discrepancies introduced by different forcing functions have not been too large. Thus, provided that the level of ideal invariants is maintained, it seems safe to rely on the hypothesis that the small-scale behaviour of a system is independent of how it is forced, at least in the case of mechanically-forced, homogeneous, nonhelical magnetohydrodynamics.

Chapter 3

"Big whirls have little whirls...": understanding energy flow

3.1 Introduction

Sustaining a magnetic field requires a constant injection of energy to counteract dissipation. Applications of MHD turbulence usually find themselves in the categories of decaying or mechanically-forced turbulence, rather than magnetically-forced. So it is beneficial for the conversion of this injected kinetic energy into magnetic energy to be efficient. But it is not just this process which amplifies magnetic fields. The transfer of energy into the magnetic field at a particular scale can be broken down into two parts: the conversion of kinetic to magnetic energy (dynamo action) and the redistribution of magnetic energy between different scales.

The MHD equations (and the Navier-Stokes equations for hydrodynamic flow) are quadratic, meaning that in wavenumber space any energy exchange involves three wavevectors. These wavevectors, $\mathbf{k}$, $\mathbf{p}$ and $\mathbf{q}$, must satisfy the *triad condition* $\mathbf{k} + \mathbf{p} + \mathbf{q} = 0$ (see Appendix A). One such exchange of energy is called a triadic interaction, and the total transfer of energy at any point in time involves summing over all possible combinations of wavevectors. For simplicity, we will take $\mathbf{k}$ to be the wavevector which receives energy, $\mathbf{q}$ to be the wavevector which loses energy, and $\mathbf{p}$ to be the mediating mode which completes the triad. A cruical detail in the Kolmogorov-Richardson cascade picture of homogeneous, isotropic hydrodynamic turbulence is that inertial range energy transfers are local and

forward in wavenumber space. This means that energy flows from large scales, i.e. small wavenumbers, to progressively smaller scales. This idea is less valid in MHD, as we shall see.

The DNS code which was used to obtain the results of this thesis, eDNS [81, 138], computes the transfer functions $T_K(k,t)$ and $T_M(k,t)$ which describe respectively the total energy transferred into the velocity field at wavenumber k and into the magnetic field at wavenumber k. These functions are composed of the sum of all triadic interactions associated with $\mathbf{u}(\mathbf{k},t)$ and $\mathbf{b}(\mathbf{k},t)$. As mentioned in the Introduction, these are the purely hydrodynamic interactions, energy exchanges between the velocity and magnetic fields, and magnetic-to-magnetic transfers mediated by the velocity field. Specifically, the definitions are

$$T_K(k,t) = \sum_{|\mathbf{k}|=k} \sum_{p=1}^{k_{max}} \sum_{q=1}^{k_{max}} (-\mathbf{u}_k(\mathbf{u}_q \cdot \nabla)\mathbf{u}_p + \mathbf{u}_k(\mathbf{b}_q \cdot \nabla)\mathbf{b}_p) \text{ and} \tag{3.1}$$

$$T_M(k,t) = \sum_{|\mathbf{k}|=k} \sum_{p=1}^{k_{max}} \sum_{q=1}^{k_{max}} (\mathbf{b}_k(\mathbf{b}_q \cdot \nabla)\mathbf{u}_p - \mathbf{b}_k(\mathbf{u}_q \cdot \nabla)\mathbf{b}_p) \ , \tag{3.2}$$

where k_{max} is the maximum wavenumber in a simulation.

3.2 Shell-to-shell transfers in simulations

To obtain detailed information about the energy transfer, the following shell decomposition is used [2, 4, 96]:

$$\mathbf{u}(\mathbf{k}) = \sum_K \mathbf{u}_K(k), \tag{3.3}$$

$$\mathbf{b}(\mathbf{k}) = \sum_K \mathbf{b}_K(k) \tag{3.4}$$

where

$$\mathbf{u}_K(\mathbf{k}) = \begin{cases} \mathbf{u}(\mathbf{k}), & \text{if } K - \frac{1}{2} \leq |\mathbf{k}| < K + \frac{1}{2} \\ 0 & \text{otherwise} \end{cases} \tag{3.5}$$

$$\mathbf{b}_K(\mathbf{k}) = \begin{cases} \mathbf{b}(\mathbf{k}), & \text{if } K - \frac{1}{2} \leq |\mathbf{k}| < K + \frac{1}{2} \\ 0 & \text{otherwise.} \end{cases} \tag{3.6}$$

The energy transfer terms can derived from the MHD equations:

- $u_p \to u_k : -\int d\mathbf{x}\, \mathbf{u}_k(\mathbf{u}_q \cdot \nabla)\mathbf{u}_p$
- $b_p \to u_k : \int d\mathbf{x}\, \mathbf{u}_k(\mathbf{b}_q \cdot \nabla)\mathbf{b}_p$
- $u_p \to b_k : \int d\mathbf{x}\, \mathbf{b}_k(\mathbf{b}_q \cdot \nabla)\mathbf{u}_p$
- $b_p \to b_k : -\int d\mathbf{x}\, \mathbf{b}_k(\mathbf{u}_q \cdot \nabla)\mathbf{b}_p$
- $z_p^+ \to z_k^+ : -\int d\mathbf{x}\, \mathbf{z}_k^+(\mathbf{z}_q^- \cdot \nabla)\mathbf{z}_p^+.$
- $z_p^- \to z_k^- : -\int d\mathbf{x}\, \mathbf{z}_k^-(\mathbf{z}_q^+ \cdot \nabla)\mathbf{z}_p^-.$

They need to be written in a form suitable for the code, i.e. involving a cross product rather than a dot product. To do this, we use the identities

$$\nabla(\mathbf{A}\cdot\mathbf{B}) = (\mathbf{A}\cdot\nabla)\mathbf{B} + (\mathbf{B}\cdot\nabla)\mathbf{A} + \mathbf{A}\times(\nabla\times\mathbf{B}) + \mathbf{B}\times(\nabla\times\mathbf{A})\ , \quad (3.7)$$

$$\nabla\times(\mathbf{A}\times\mathbf{B}) = \mathbf{A}(\nabla\cdot\mathbf{B}) - \mathbf{B}(\nabla\cdot\mathbf{A}) + (\mathbf{B}\cdot\nabla)\mathbf{A} - (\mathbf{A}\cdot\nabla)\mathbf{B}\ , \quad (3.8)$$

along with the facts that $\nabla\cdot\mathbf{A} = \nabla\cdot\mathbf{B} = 0$ for $\mathbf{A},\mathbf{B} = \mathbf{u},\mathbf{b},\mathbf{z}^{\pm}$, and gradient terms are projected out.

Thus we have

$$(\mathbf{B}\cdot\nabla)\mathbf{A} = \frac{1}{2}\left[\nabla\times(\mathbf{A}\times\mathbf{B}) + (\nabla\times\mathbf{B})\times\mathbf{A} + (\nabla\times\mathbf{A})\times\mathbf{B}\right] \quad (3.9)$$

and so the transfer terms are

- $u_p \to u_k : -\frac{1}{2}\int d\mathbf{x}\, \mathbf{u}_k\left[\nabla\times(\mathbf{u}_p\times\mathbf{u}_q) + (\nabla\times\mathbf{u}_p)\times\mathbf{u}_q + (\nabla\times\mathbf{u}_q)\times\mathbf{u}_p\right]$
- $b_p \to u_k : \frac{1}{2}\int d\mathbf{x}\, \mathbf{u}_k\left[\nabla\times(\mathbf{b}_p\times\mathbf{b}_q) + (\nabla\times\mathbf{b}_p)\times\mathbf{b}_q + (\nabla\times\mathbf{b}_q)\times\mathbf{b}_p\right]$
- $u_p \to b_k : \frac{1}{2}\int d\mathbf{x}\, \mathbf{b}_k\left[\nabla\times(\mathbf{u}_p\times\mathbf{b}_q) + (\nabla\times\mathbf{u}_p)\times\mathbf{b}_q + (\nabla\times\mathbf{b}_q)\times\mathbf{u}_p\right]$
- $b_p \to b_k : -\frac{1}{2}\int d\mathbf{x}\, \mathbf{b}_k\left[\nabla\times(\mathbf{b}_p\times\mathbf{u}_q) + (\nabla\times\mathbf{b}_p)\times\mathbf{u}_q + (\nabla\times\mathbf{u}_q)\times\mathbf{b}_p\right]$
- $z_p^+ \to z_k^+ : -\frac{1}{2}\int d\mathbf{x}\, \mathbf{z}_k^+\left[\nabla\times(\mathbf{z}_p^+\times\mathbf{z}_q^-) + (\nabla\times\mathbf{z}_p^+)\times\mathbf{z}_q^- + (\nabla\times\mathbf{z}_q^-)\times\mathbf{z}_p^-\right]$
- $z_p^- \to z_k^- : -\frac{1}{2}\int d\mathbf{x}\, \mathbf{z}_k^-\left[\nabla\times(\mathbf{z}_p^-\times\mathbf{z}_q^+) + (\nabla\times\mathbf{z}_p^-)\times\mathbf{z}_q^+ + (\nabla\times\mathbf{z}_q^+)\times\mathbf{z}_p^+\right]$

The transfer function module of the code computes snapshots of shell-to-shell transfer functions at specific points in time throughout an MHD simulation.

ID	ρ_M	ρ_c
nonhelical	0	0
magnetic helicity	1	0
cross helicity	0	0.7

Table 3.1: Initial conditions of the decaying MHD examined in Chapter 3.

The module is necessarily computationally expensive because the transfer terms are computed partly in real space and partly in Fourier space, and this step is performed for every combination of k, p and q. First the cross product is computed in real space, and then after Fourier transforming, the curl, which becomes a simple multiplication in Fourier space, is computed. For a simulation which does not explicitly compute shell-to-shell transfers only one transform is needed per timestep, but to fully-capture the transfers in a simulation with k_{max} wavenumbers, there are k_{max}^3 transforms at each timestep. Ideally the decomposition would happen with a high frequency in steady-state turbulence in order to obtain good statistics; this is understandably not feasible for large simulations. However, even a small smaple size of five-to-ten snapshots provides a clear insight into the nature of the interactions between scales.

3.3 Results

Simulations of decaying, homogeneous MHD turbulence without a mean magnetic field were performed on a grid of 512^3 points with the initial peak of the spectra at $k = 5$. Since the turbulence was decaying, we ran ensembles of size 10. Three sets of initial conditioned were explored, as outlined in Table 3.1.

3.3.1 The effects of magnetic and cross helicity on the direction and locality of transfers

Nonhelical MHD

To set the scene, we will look at nonhelical decaying MHD where the initial peak of the spectrum is small, $k_0 = 5$. We will then compare the transfers to MHD with magnetic and cross helicity. Nonhelical MHD has seen renewed interest because of the recent evidence of nonhelical reverse spectral transfer. The fact that this

is possible in the nonhelical case highlights that the phenomenon is an intrinsic feature of homogeneous MHD. Nonetheless, its actual mechanism or mechanisms are not well-understood.

We begin by breaking down the energy transfers into four types: u-to-b, b-to-b, z^+-to-z^+, and z^--to-z^- (see Figure 3.1). In the interest of brevity we do not consider the u-to-u transfers or the b-to-u transfers (although the latter are reflected in the u-to-b plots). We measure the instantaneous energy transfers in decaying turbulence subject to different initial values of magnetic and cross helicity. A small ensemble in each case is used to smooth out the functions. The scenario here is very simple [40, 42, 76]: the transfers, whether expressed in terms of the u-to-b and b-to-b or z^+-to-z^+ and z^--to-z^- transfers, are concentrated close to either side of the line $x = y$, with positive values above the line and negative values below. This means the energy transfers are forward and local. The strengths of the transfers decrease with increasing wavenumber, in other words proportionally to the energy spectra. The b-to-b interactions are more dominant than the u-to-b interactions, which are slightly more asymmetrical: the small velocity modes appear to give energy to a broader range of magnetic modes, with the larger velocity modes playing less of a role and the the b-to-u feedback staying local. The Elsässer transfers look very much the same as each other, as should be expected in a simulation with no cross helicity.

Initially large magnetic helicity

The situation is quite different in the ensemble of simulations with initially large magnetic helicity. Figure 3.2 shows the transfer functions. Clearly there is a net transfer into the large scales of the magnetic field, as one would expect. If we were to look only at the Elsässer transfers it would be reasonable to conclude that the RST is a relatively simple effect which affects both of the Elsässer fields in the same way, i.e. a change in sign of the transfer directions at scales larger than the peak of the energy spectrum. But the u-to-b and b-to-b transfer functions tell another story. As is known from previous studies, there is a nonlocal transfer of energy from the velocity field to the largest scales of the magnetic field accompanied by local b-to-b RST at the same large scales. To understand these features better we will later consider the effect of the *mediating* mode.

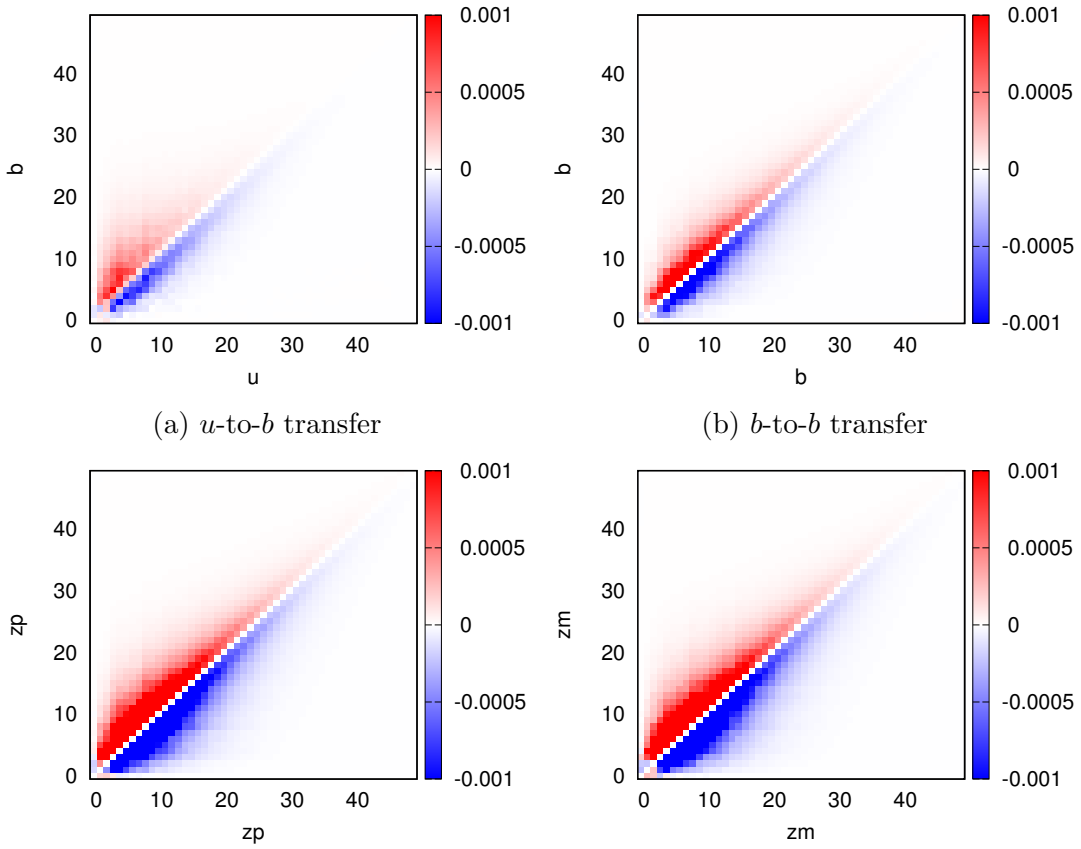

(a) u-to-b transfer

(b) b-to-b transfer

(c) z^+-to-z^+ transfer

(d) z^--to-z^- transfer

Figure 3.1: Energy transfer in the nonhelical case. The plots have the wavenumbers of the giving mode along the x-axis and the receiving mode along the y-axis, so positive values above the $x = y$ line and negative values below the line indicate a forward transfer of energy.

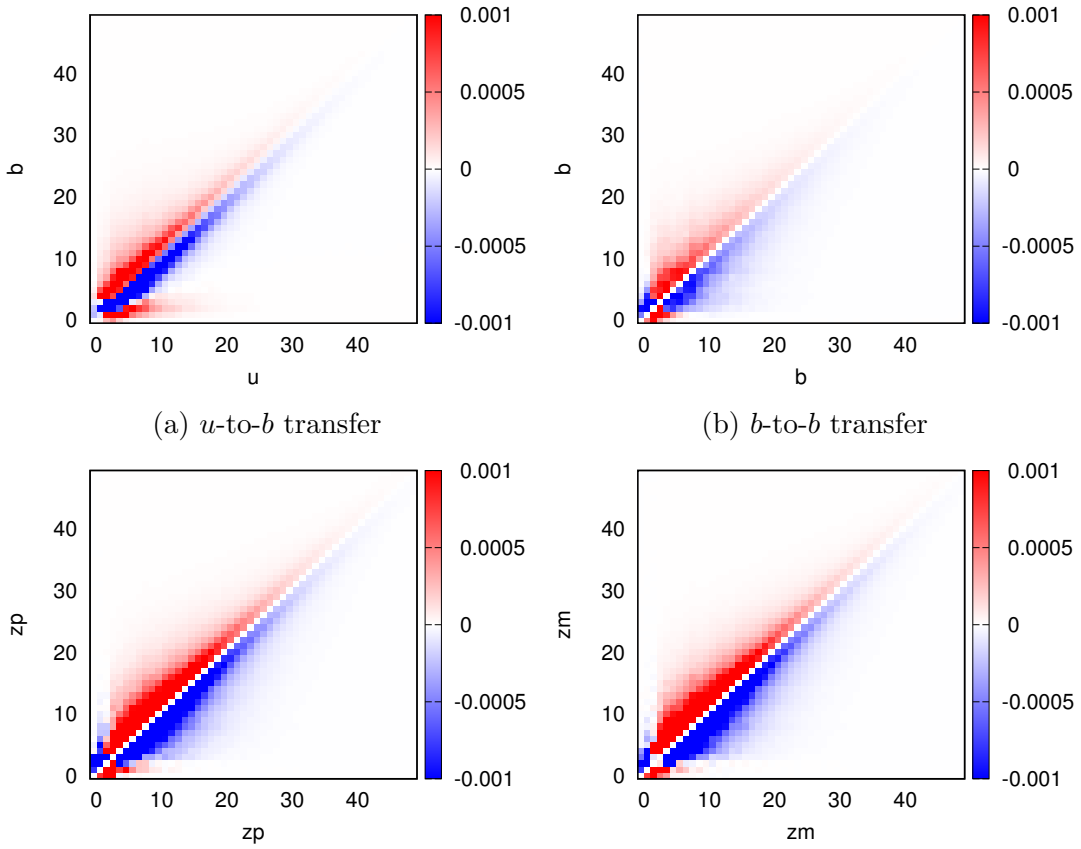

(a) u-to-b transfer

(b) b-to-b transfer

(c) z^+-to-z^+ transfer

(d) z^--to-z^- transfer

Figure 3.2: As Fig. 3.1 but in the case with initially large magnetic helicity.

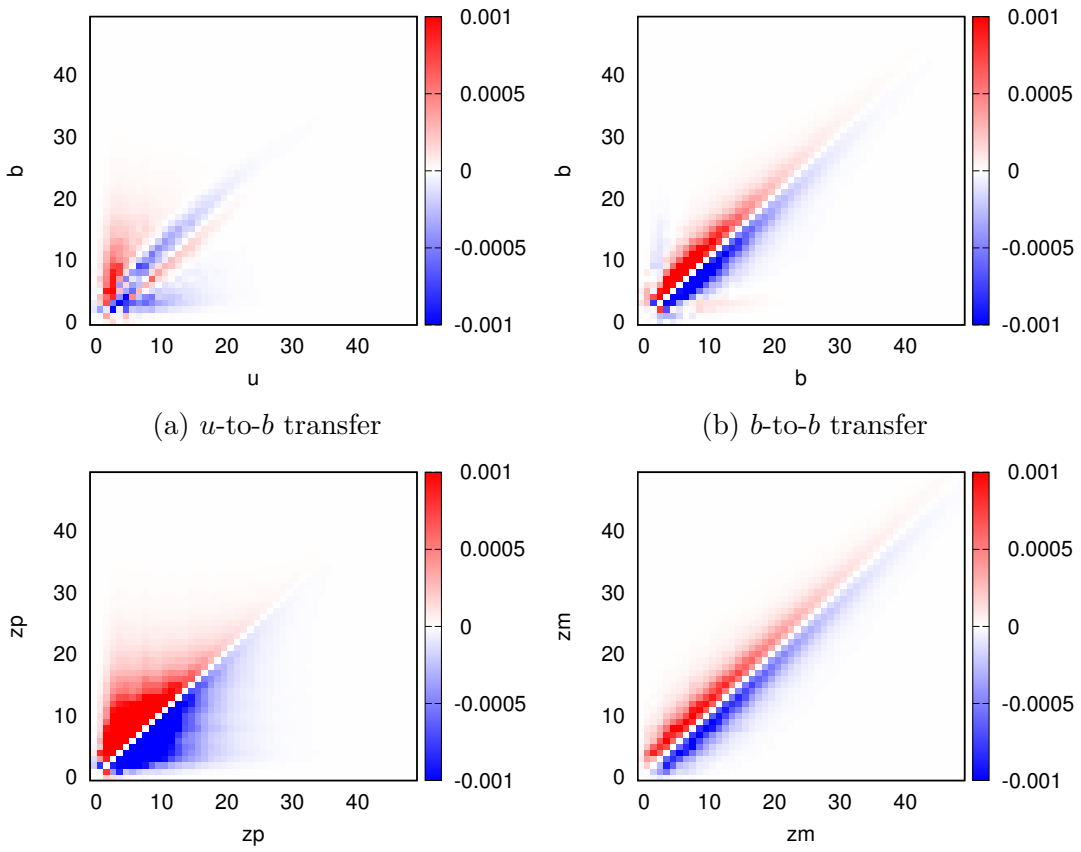

(a) u-to-b transfer

(b) b-to-b transfer

(c) z^+-to-z^+ transfer

(d) z^--to-z^- transfer

Figure 3.3: As Fig. 3.1 but in the case with initially large cross helicity.

Initially large cross helicity

Moving on to the case with initially large cross helicity (Figure 3.3), we can see that the u-to-b transfers are strongly affected. The transfers are very much weakened and their directionality is less uniform. The local u-to-b transfers are in the reverse direction, the large-scale velocity field feeds the magnetic field nonlocally and vice versa. The b-to-b transfer, however, is relatively unaffected by the cross helicity, with strong, local, forwards transfers at all scales, except possibly the very largest scales. Perhaps clearer is the Elsässer point of view: in this situation with large-but-not-maximal positive cross helicity, the z^- field maintains small amounts of local forward transfer whereas the z^+ field has stronger interactions, increased nonlocality and signs of RST at the largest scales.

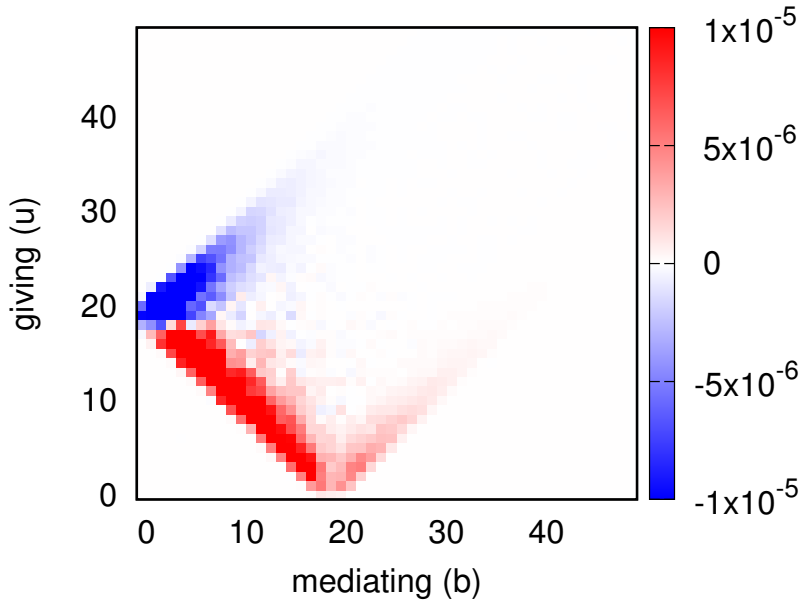

Figure 3.4: Kinetic-to-magnetic energy transfer into the 20th wavenumber. Red corresponds to energy gain; blue to energy loss. The y-axis indicates the velocity modes which are exchanging energy and the x-axis indicates the third mode in the interactions.

3.3.2 The effect of the mediating mode

We have seen that magnetic and cross helicity can influence the locality, strength and directions of energy transfers. What we have not yet taken into account is the effect of the third mode in any particular energy exchange. This third mode, bound by the triad condition, does not itself exchange energy but mediates the energy flow between the two modes to which it is coupled. The sum over all interactions with all possible mediating modes is what is shown in the above figures. I wish to address the question of which effects, e.g. local and nonlocal forward and reverse transfers, are governed by which triad geometries, e.g. local interactions where the three wavenumbers form an approximately equilateral triangle or nonlocal interactions where the triangle is long and narrow.

Figure 3.4 shows, as an example, the kinetic-to-magnetic energy transfer into the magnetic field at wavenumber 20 in the nonhelical case. The x and y axes show which magnetic wavenumbers are mediating the transfer from which velocity wavenumers. The triad condition is automatically embedded into the results, as we can see the rectangular shape confining the interactions to $q < k + p$, $q > p - k$ and $q > k - p$ (where k, p and q are the receiving, mediating and giving wavenumbers, respectively). In this example, we can see that the transfers are all

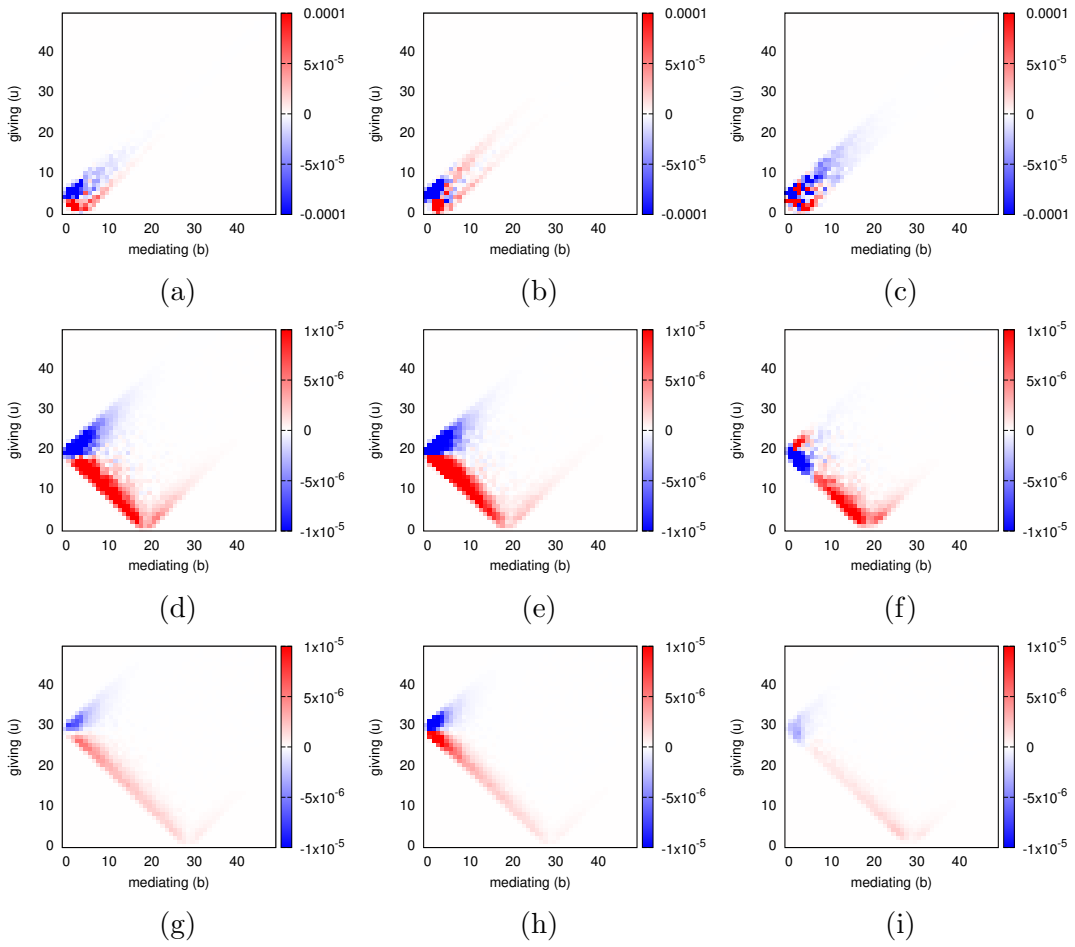

Figure 3.5: u-to-b transfers into $k = 5$ (a, b, c), $k = 20$ (d, e, f) and $k = 30$ (g, h, i). The leftmost column is the nonhelical case, the central column is the magnetic helicity case and the rightmost column is the cross helicity case.

forwards (positive-valued below the $y = 20$ line and negative-valued above it) and mostly local with both nonlocal and local mediating wavenumbers. Interestingly, there is also a small amount of nonlocal u-to-b transfer mediated by a large magnetic wavenumber.

Figures 3.5, 3.6, 3.7, and 3.8 focus each on one of the four types of energy transfer we have been considering (u-to-b, b-to-b, z^+-to-z^+ and z^--to-z^-). Each column corresponds to a different set of initial conditions (fully nonhelical, large magnetic helicity, large cross helicity) and each row to a different receiving wavenumber ($k = 5, 20, 30$). These examples illustrate the different types of interaction that can arise under different circumstances.

The first thing to note in each case is the directionality of the transfers: whether or not the transfers are positive below the $p = k$ line and negative above it. We

find evidence of RST in the following:

- u-to-b
  - magnetic helicity (large scales, locally)
  - cross helicity (large and intermediate scales, particularly for large mediating wavenumbers)
- b-to-b
  - magnetic helicity (large scales, locally)
  - cross helicity (large and intermediate scales, for the wavenumber ordering $q < p < k$ i.e. giving<mediating<receiving)

The cross helicity RST is interesting because we did not see a significant effect in the integrated transfer functions. In the Elsässer representation, we can see that the magnetic helicity RST comes about mostly through local, large-scale couplings but that there is also a very small nonlocal transfer to the largest scales. Other than that, compared to the nonhelical case, the transfers look really quite similar. Positive cross helicity seems to strengthen the forward z^+-to-z^+ energy transfer from all scales and weaken the z^--to-z^- transfers, except where the mediating z^+ wavenumber is small. We do not see RST in these interactions.

3.3.3 Triad interactions and the magnetic Prandtl number

A future application of the shell decomposition module should be systems with nonunity magnetic Prandtl number. Before we examine various macroscopic properties of these systems in the following chapter, I will briefly discuss how the triad interactions are likely to be affected by the magnetic Prandtl number.

The most naive disentangling of triadic interactions in MHD using helical modes (i.e. decomposing the velocity and magnetic fields into a positively-helical part and a negatively-helical part [79], section 8) can provide some clues about the mechanisms of energy transfer. Specifically, for the reverse transfer of energy, there are three possibilities: two of these arise from the coupling of two magnetic modes and one velocity mode, and the third is a purely hydrodynamic reverse spectral transfer which only has a net effect when all other types of interaction

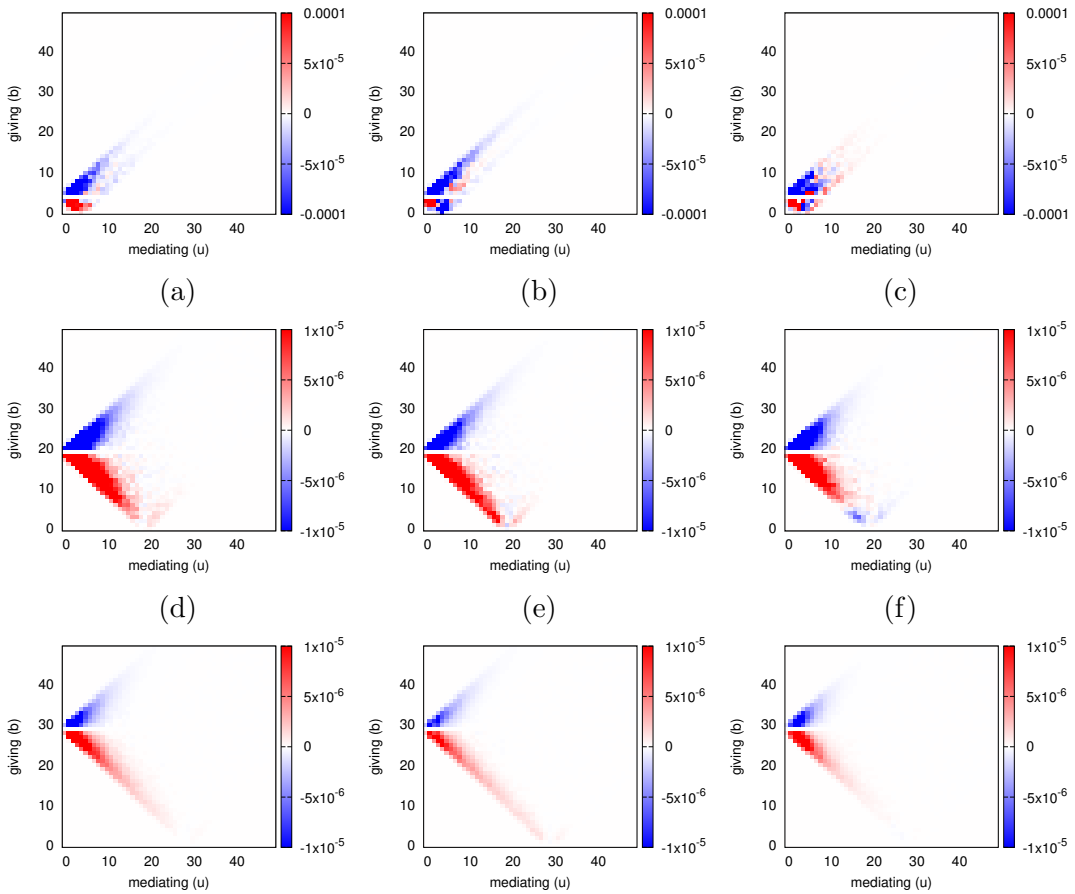

Figure 3.6: *b*-to-*b* transfers. The plots are arranged in the same way as Figure 3.5.

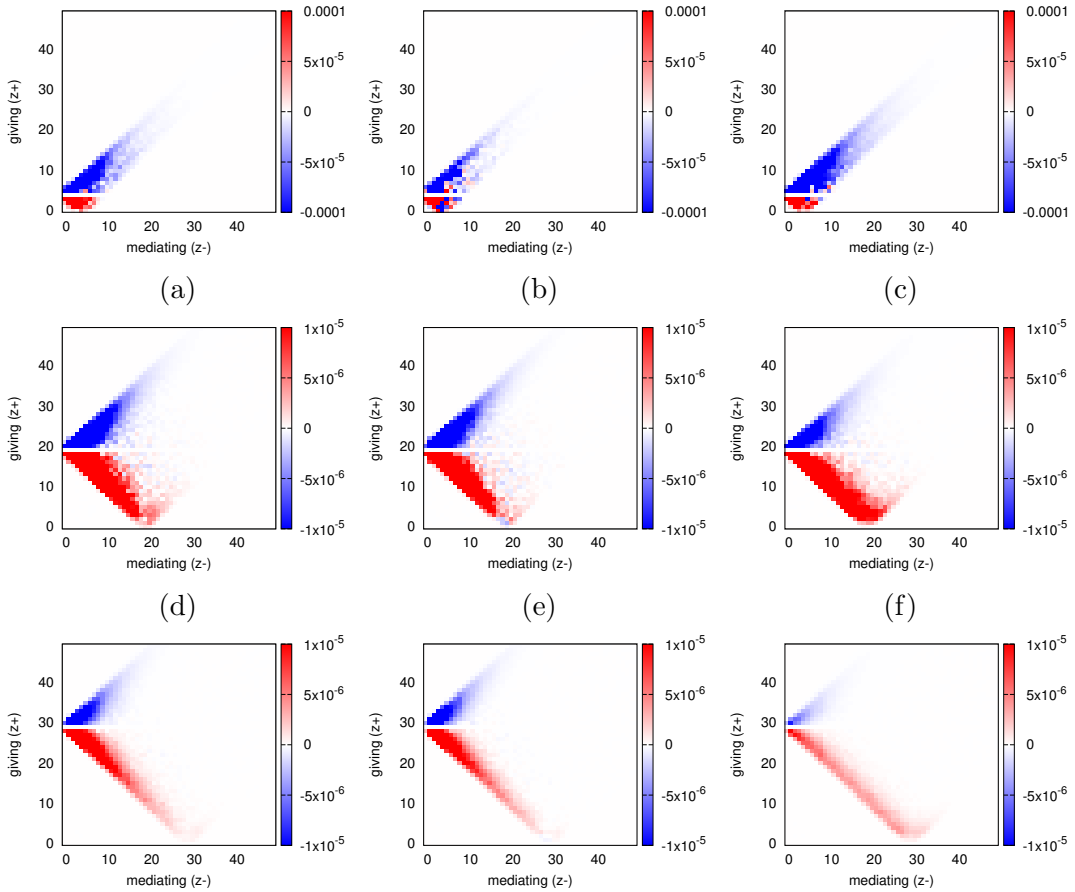

Figure 3.7: z^+-to-z^+ transfers. The plots are arranged in the same way as Figure 3.5.

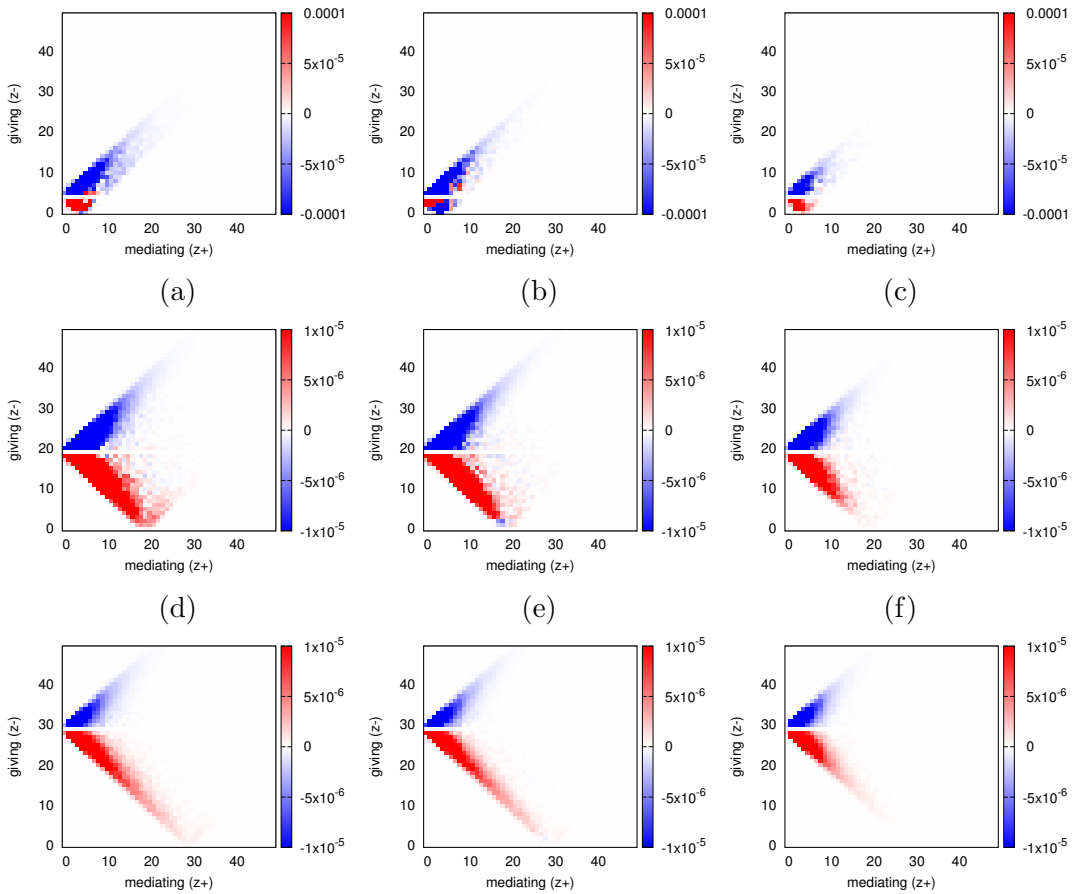

Figure 3.8: z^--to-z^- transfers. The plots are arranged in the same way as Figure 3.5.

are filtered out. A velocity mode can transfer energy to the magnetic field at a larger or smaller scale if it is coupled to two magnetic modes with opposite signs of helicity to each other. If two coupled magnetic modes have the same sign of helicity there is a reverse transfer from the smaller-scale magnetic field to the larger scale, and also a transfer to the third mode in the triad, a velocity mode. In reality the energy transferred between scales is a complicated function depending on energies, wavenumbers and helicities, and a simple, decoupled analysis of single triads cannot fully describe the dynamics of the problem, but it does allow us to begin to make sense of the many ways in which energy can move between different length scales.

As we know, triadic interactions are generally either local, with all three wavenumbers having a similar magnitude, or nonlocal, involving one small wavenumber k and two larger wavenumbers $p \simeq q$. Local interactions always produce local energy transfers, but nonlocal interactions may produce local energy transfers between p and q or nonlocal transfers between k and p or q.

Studies of triadic interactions are generally concerned with energy transfer rather than dissipation, and, as such, do not require knowledge of the magnetic Prandtl number. However, when considering the total effect of all triadic interactions, the value of $\mathrm{Pr_M}$ becomes relevant. When the magnetic Prandtl number is not equal to one, there is a separation of dissipative length scales and an intermediate range between these two scales, where one field is in the dissipative regime but the other is not. In a basic model, one could consider all velocity modes with wavenumbers larger than the kinetic dissipation wavenumber k_ν to be inactive, in the sense that they contain no kinetic energy and immediately dissipate any energy that is transferred to them. At scales smaller than the magnetic dissipation scale, i.e. when the wavenumber is larger than k_η, the magnetic field would be treated similarly. In the following analysis we will consider how the magnetic Prandtl number affects two main types of interaction: local interactions which occur in-between the two dissipative scales, i.e. $k_{\eta \text{ or } \nu} < k \simeq p \simeq q < k_{\nu \text{ or } \eta}$ and nonlocal interactions, in which $k << k_{\eta \text{ or } \nu} < p \simeq q < k_{\nu \text{ or } \eta}$. We assume that interactions in which all three wavenumbers are less than both dissipative scales are unaffected by the magnetic Prandtl number.

When $\mathrm{Pr_M} < 1$, $k_\eta < k_\nu$ and in the range between these two wavenumbers the magnetic field is inactive. Since triadic interactions involve either three velocity modes or one velocity mode and two magnetic modes, the allowed interactions in the intermediate range are the local hydrodynamic interaction, local and nonlocal

velocity-to-small-scale-magnetic transfers in which the energy would be removed from the system (e.g. Figure 3.5h) and nonlocal reverse transfers from the small-scale velocity field to the large-scale magnetic field (e.g. Figure 3.5b). This third mechanism is particularly relevant in the context of dynamo action: part of what sustains a magnetic field may come from the small-scale velocity field. Therefore in simulations it is important to make sure that both dissipation scales are included. Furthermore, since energy is transferred from the velocity field at the forcing scale to the magnetic and velocity fields at all scales [76], for each Re_M there should be a value of $\mathrm{Pr_M}$ below which more energy will be transferred to the dissipative part of the magnetic field than to wavenumbers smaller than k_η. It thus seems natural that at some critical value $\mathrm{Pr_{M,crit}}$ the magnetic field would become unsustainable, as put forward in [117]. In the other scenario, that is, $\mathrm{Pr_M} > 1$, we have $k_\nu < k_\eta$ and the velocity field is inactive in the intermediate range. We thus no longer have small-scale purely hydrodynamic interactions or the possibility of the nonlocal reverse transfer from the velocity field to the magnetic field. We may however still have nonlocal interactions between a large-scale velocity mode and two small-scale magnetic modes, which, according to the simplest helical mode model, would involve a nonlocal forward energy transfer from the velocity mode to the magnetic modes and, in the presence of magnetic helicity, a local reverse energy transfer between the magnetic modes. Furthermore, in the helical case, reverse magnetic-to-magnetic and reverse magnetic-to-velocity transfers, both local and nonlocal, may also occur.

These ideas have not yet been examined with the shell decomposition module because of time and computational constraints, but makes for interesting future work. For accurate results, especially around the threshold of parameter space where a magnetic field may be sustained, both dissipation scales must be well resolved.

3.4 Conclusion

In this chapter we examined the flow of energy in homogeneous MHD using a shell decomposition module written for the in-house DNS code. This module computes shell-to-shell energy transfers as a function of three wavenumbers; a coarse-grained version of the fundamental triadic interactions. The transfers were examined in the context of decaying simulations with three initial settings of magnetic and cross helicity. We looked at fully nonhelical initial conditions,

maximum magnetic helicity with zero cross helicity, and zero magnetic helicity with 70% of the maximum allowed value of cross helicity. Maximum cross helicity was not used since if the fields are fully-aligned the term responsible for energy transfer disappears. We compared the different ways that RST manifests from the point of view of the physical (magnetic and velocity) fields and the Elsässer fields. We showed that RST was mostly evident in the scales larger than the peak of the energy spectra. To study this more closely the three-wavenumber transfer functions should be computed in situations with highly-peaked spectra. Finally, we made a connectino between the analytical study of triad interactions and the computational study by presenting ideas for future work with nonunity magnetic Prandtl number.

Chapter 4

Velocity versus magnetism: the influence of the magnetic Prandtl number

4.1 Introduction

Physical properties of a magnetofluid affect its behaviour. One such property is the magnetic Prandtl number $\mathrm{Pr_M} = \mathrm{Re}_M/\mathrm{Re}$, where Re_M and Re are the magnetic and kinetic Reynolds numbers, quantifying respectively the turbulence of the magnetic and kinetic components of the fluid. In nature, extreme values of $\mathrm{Pr_M}$ are commonplace: stellar and planetary interiors can have $\mathrm{Pr_M}$ in the range $\mathrm{Pr_M} \sim 10^{-4}$ to 10^{-7} and smaller, while the interstellar medium and cosmological-scale magnetic fields have estimated values of $\mathrm{Pr_M} \sim 10^{10}$ to 10^{14} [49, 106, 118–120, 135]. The achievable range of $\mathrm{Pr_M}$ in direct numerical simulations (DNS) is highly restricted because of computational requirements and is often set to one, which is not representative of most magnetofluids. Extrapolating from simulations with $\mathrm{Pr_M}$ in the vicinity of one is very often necessary when connecting computational results to real-life applications. That said, the region around unity is not without its applications: models of black hole accretion disks indicate that $\mathrm{Pr_M}$ may transition from being very small in most of the disk, to being greater than one near the centre, potentially providing an explanation for the change of state from emission to accretion in these objects [10]. Estimates of $\mathrm{Pr_M}$ in the solar wind and solar convective zone have found $\mathrm{Pr_M} \simeq 1$ [134, 135]. In tokamak reactors $\mathrm{Pr_M}$ is usually small but could become as large as 100 [91].

In this chapter we present an array of 36 high-resolution DNS of mechanically-forced, homogeneous, incompressible magnetohydrodynamic turbulence without a mean magnetic field, in the range $\mathrm{Pr_M}$=1/32 to 32. Additionally, we present 18 decaying simulations in the range $\mathrm{Pr_M}$=1/16 to 16, in which we test the effect of $\mathrm{Pr_M}$ on reverse spectral energy transfer (also known as the inverse cascade). With our forced data we focus on the energy spectra, the ratios of the total kinetic and magnetic energies E_K/E_M and the kinetic and magnetic dissipation rates $\varepsilon_K/\varepsilon_M$. We also discuss resolution requirements in connection with recent theoretical findings.

In previous studies, an approximate scaling $\varepsilon_K/\varepsilon_M \simeq \mathrm{Pr_M}^q$ was found [22, 116]. The parameter q varied depending on the magnetic helicity (i.e. the knottedness of the magnetic field) and whether $\mathrm{Pr_M}$ was greater than or less than one. However, these papers only guaranteed full resolution of one dissipation scale. In other words, the largest wavenumber in the simulation, k_{max}, was greater than either the kinetic dissipation wavenumber $k_\nu = (\varepsilon_K/\nu^3)^{1/4}$ (where ν is the kinematic viscosity) or the magnetic dissipation wavenumber $k_\eta = (\varepsilon_M/\eta^3)^{1/4}$ (where η is the magnetic resistivity), but not both. This is an issue because although a system's energy is mostly concentrated in the largest length scales, the dissipation spectrum is proportional to the wavenumber squared. In hydrodynamic turbulence, in order to capture 99.5% of the dissipative dynamics, the condition $k_\nu > 1.25 k_{max}$ must be fulfilled [138]. Therefore we took this as the definition of "fully-resolved" and in all our forced simulations made sure that the maximum resolved wavenumber was always at least 1.25 times greater than both dissipation wavenumbers.

Of particular interest in MHD turbulence is the presence and efficiency of dynamo action, that is, the conversion of kinetic energy to magnetic energy. Below some critical value of Re_M (in the region of Re_M=50 for $\mathrm{Pr_M}$=1) the magnetic field becomes unsustainable [11, 61, 75, 129], and above this threshold, the magnetic field may be shut down if Re is too large relative to Re_M, i.e. below a critical value of $\mathrm{Pr_M}$ [117].

Our set of forced simulations are an extensive dataset for DNS of homogeneous MHD turbulence, with 36 data points in the Re-Re_M plane covering a square grid (see Fig. 4.1 for a summary and Table 4.1). Re and Re_M range from approximately 50 to 2300, allowing for a three order of magnitude range in magnetic Prandtl number. Each point was run on a 512^3 or 1024^3 lattice depending on the resolution requirements at each Re and Re_M, ensuring that the data for all the grid points

were fully resolved. This is the largest fully-resolved set of data for a magnetic Prandtl number study.

ν	η	Pr_M	Re	Re_M	k_{max}/k_ν	k_{max}/k_η	E_K	E_M	ε_K	ε_M	ρ_M	ρ_C
0.01	0.01	1	73	73	9.30	9.30	0.434	0.032	0.078	0.031	0.005	0.031
0.01	0.005	2	69	139	9.21	5.48	0.376	0.066	0.063	0.051	-0.007	0.032
0.01	0.0025	4	66	263	9.24	3.27	0.319	0.096	0.054	0.058	0.012	-0.013
0.01	0.00125	8	62	494	9.25	1.94	0.273	0.127	0.051	0.061	0.011	0.001
0.01	0.000625	16	61	970	9.06	1.13	0.258	0.156	0.053	0.068	-0.006	-0.007
0.01	0.0003125	32	56	1803	18.33	1.36	0.225	0.203	0.055	0.062	-0.003	-0.032
0.005	0.01	0.5	138	69	5.48	9.21	0.497	0.022	0.083	0.030	0.013	0.021
0.005	0.005	1	133	133	5.51	5.51	0.412	0.059	0.056	0.054	0.011	-0.003
0.005	0.0025	2	129	258	5.48	3.26	0.336	0.112	0.045	0.067	0.037	-0.019
0.005	0.00125	4	124	497	5.48	1.94	0.313	0.121	0.045	0.068	-0.007	0.026
0.005	0.000625	8	128	1023	10.94	2.30	0.295	0.155	0.047	0.068	0.006	-0.035
0.005	0.0003125	16	112	1794	10.97	1.37	0.247	0.191	0.050	0.064	0.006	-0.015
0.0025	0.01	0.25	252	63	3.28	9.28	0.519	0.012	0.087	0.023	0.009	0.001
0.0025	0.005	0.5	279	139	3.24	5.45	0.471	0.058	0.051	0.065	-0.015	0.018
0.0025	0.0025	1	270	270	3.22	3.22	0.416	0.088	0.043	0.075	0.009	0.016
0.0025	0.00125	2	251	502	3.26	1.94	0.337	0.122	0.040	0.073	0.002	-0.003
0.0025	0.000625	4	256	1025	6.50	2.30	0.319	0.152	0.043	0.073	-0.009	0.025
0.0025	0.0003125	8	232	1857	6.49	1.36	0.269	0.185	0.047	0.069	0.009	-0.043
0.00125	0.01	0.125	514	64	1.94	9.22	0.534	0.017	0.076	0.037	0.007	0.016
0.00125	0.005	0.25	527	132	1.93	5.45	0.524	0.032	0.058	0.057	-0.008	-0.006
0.00125	0.0025	0.5	528	264	1.91	3.21	0.432	0.089	0.036	0.084	-0.004	-0.015
0.00125	0.00125	1	518	518	1.93	1.93	0.375	0.115	0.035	0.080	-0.011	-0.0003

0.00125	0.000625	2	500	1001	3.91	2.32	0.337	0.132	0.037	0.074	-0.002	-0.017
0.00125	0.0003125	4	465	1860	3.88	1.37	0.288	0.186	0.044	0.070	0.003	-0.069
0.000625	0.01	0.0625	1035	65	2.30	18.38	0.583	0.004	0.101	0.015	-0.007	-0.028
0.000625	0.005	0.125	1080	135	2.33	11.07	0.536	0.027	0.052	0.058	-0.010	-0.005
0.000625	0.0025	0.25	1094	274	2.32	6.56	0.470	0.068	0.030	0.082	-0.004	-0.011
0.000625	0.00125	0.5	1105	552	2.32	3.90	0.445	0.084	0.029	0.083	0.003	0.005
0.000625	0.000625	1	1091	1091	2.28	2.28	0.391	0.132	0.034	0.085	0.002	-0.014
0.000625	0.0003125	2	1032	2064	2.28	1.36	0.351	0.157	0.040	0.079	-0.002	-0.035
0.0003125	0.01	0.03125	2048	64	1.37	18.41	0.569	0.010	0.083	0.032	-0.005	-0.013
0.0003125	0.005	0.0625	1996	125	1.36	10.86	0.517	0.043	0.035	0.084	-0.0004	-0.006
0.0003125	0.0025	0.125	2107	263	1.37	6.51	0.463	0.076	0.022	0.092	0.010	-0.032
0.0003125	0.00125	0.25	2039	510	1.37	3.87	0.399	0.115	0.022	0.093	-0.006	0.050
0.0003125	0.000625	0.5	2068	1034	1.35	2.27	0.369	0.156	0.029	0.092	0.001	-0.007
0.0003125	0.0003125	1	2276	2276	1.33	1.33	0.397	0.168	0.038	0.092	0.005	0.016

Table 4.1: Table of data associated with the forced, high-resolution simulations of Chapter 4.
ν is the viscosity, η is the resistivity, Pr_M is the magnetic Prandtl number, Re and Re_M are the kinetic and magnetic Reynolds numbers, k_{max}/k_ν and k_{max}/k_η are the ratios of the maximum wavenumber to the kinetic and magnetic dissipation wavenumbers, E_K and E_M are the time-averaged kinetic and magnetic energies, ε_K and ε_M are the time-averaged kinetic and magnetic dissipations rates, and ρ_M and ρ_C are the relative magnetic and cross helicities. These quantities are all defined in Chapter 1.

Large values of magnetic helicity can encourage reverse spectral transfer (RST), where energy is transferred to the largest length scales in the system, rather than to the small, dissipative scales, as in the usual Richardson-Kolmogorov phenomenology [3, 4, 77, 110]. The second aspect of our study also covers magnetofluids with nonzero magnetic helicity. We found RST in both helical and nonhelical turbulence down to $\mathrm{Pr_M}=1/4$, increasing as Re_M increased, with Re playing little role. We thus confirm the results of recent simulations that found RST without helicity [13, 25, 26] and have seminal results showing RST occurring for $\mathrm{Pr_M} < 1$.

4.2 Results

We carried out DNS of the incompressible MHD equations subject to a random force $\mathbf{f_u}$ defined via a helical basis, (as in 2.2) with variable parameters that allow the injection of helicity to be adjusted; we chose to force nonhelically. As we have seen in Chapter 2, the nature of the forcing function does not greatly affect the dynamics of the fields [90]. This is also true of the forcing length scale, so long as it is sufficiently large [24]. We also ran a set of decaying simulations, where we were less interested in the inertial range energy spectra and more interested in observing RST, so we set the initial spectral peak at $k_0 = 40$. There was no imposed magnetic guide field. The viscosity and resistivity of each simulation are given in Fig. 4.1; note that $\mathrm{Re}_M \simeq 0.65/\eta$ and $\mathrm{Re} \simeq 0.65/\nu$.

4.2.1 Energy spectra of forced data

Figure 4.2 shows the time-averaged compensated kinetic energy spectra of selected simulations. In each of the three plots the solid line represents the same simulation, with $\mathrm{Re} = \mathrm{Re}_M \simeq 2275$ and $\mathrm{Pr_M} = 1$. The top plot shows the spectra of four simulations where Re and Re_M were increased with $\mathrm{Pr_M} = 1$ kept constant. The middle plot compares data with $\mathrm{Re}_M \simeq 2275$ and $\mathrm{Pr_M}$ increasing from 1 to 32 by decreasing Re; while the bottom plot shows data with $\mathrm{Re} \simeq 2275$ and $\mathrm{Pr_M}$ being decreased from 1 to 1/32 via decreasing Re_M. When we increase Re but keep $\mathrm{Pr_M}$ constant, as in the top plot, we see that less energy is stored in the large scales of the velocity field, whereas if we increase Re but keep Re_M constant and large-valued, as in the middle plot, the amount of energy in the large-scale

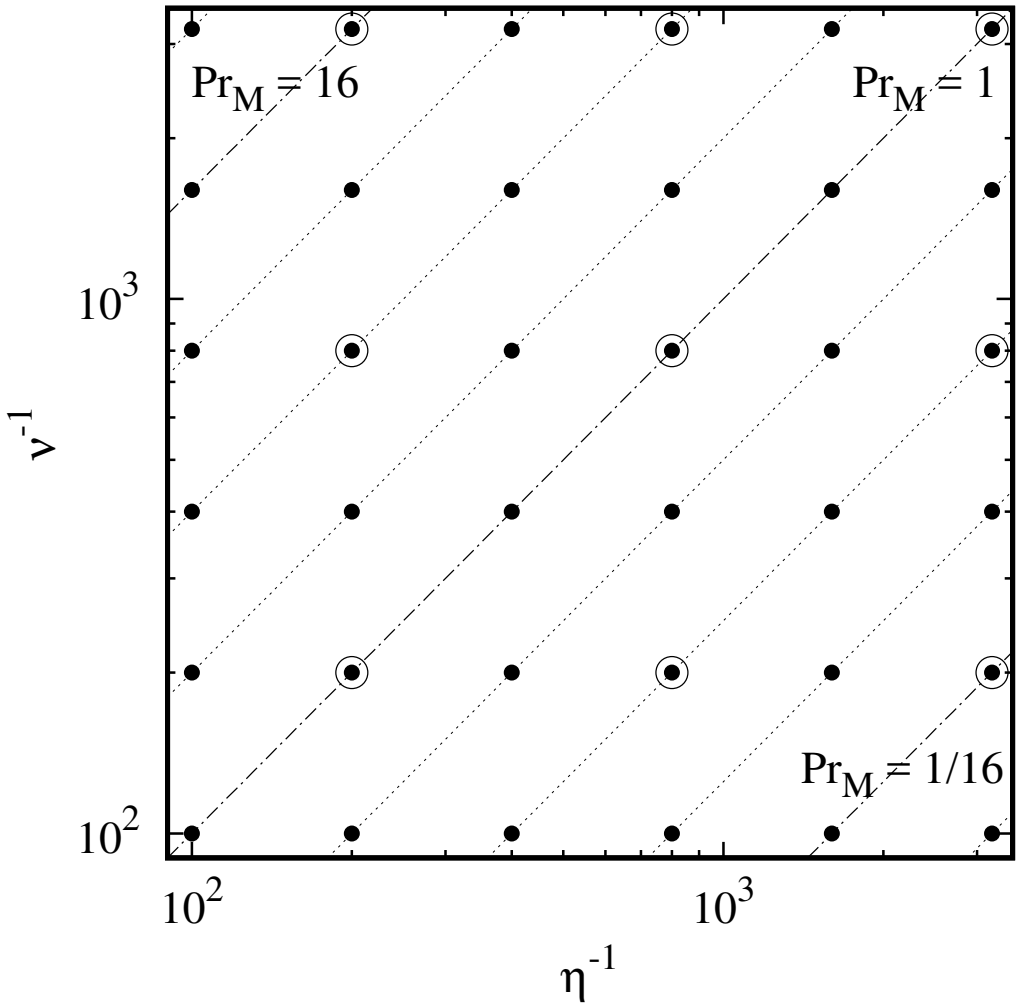

Figure 4.1: Simulations associated with the results of this chapter. Small circles show ν^{-1} and η^{-1} for each of the 36 forced simulations appearing in Figs. 4.2, 4.3, 4.4 and 4.5. The 9 large circles indicate the decaying helical and nonhelical simulations with initial spectra peaking at $k_0 = 40$ (see Fig. 4.7). The lines connect points of constant $\mathrm{Pr_M} = 2^n$ for $-5 \leq n \leq 5$. The largest and smallest values of η and ν are 0.01 and 0.0003125. See Table 4.1 for more details.

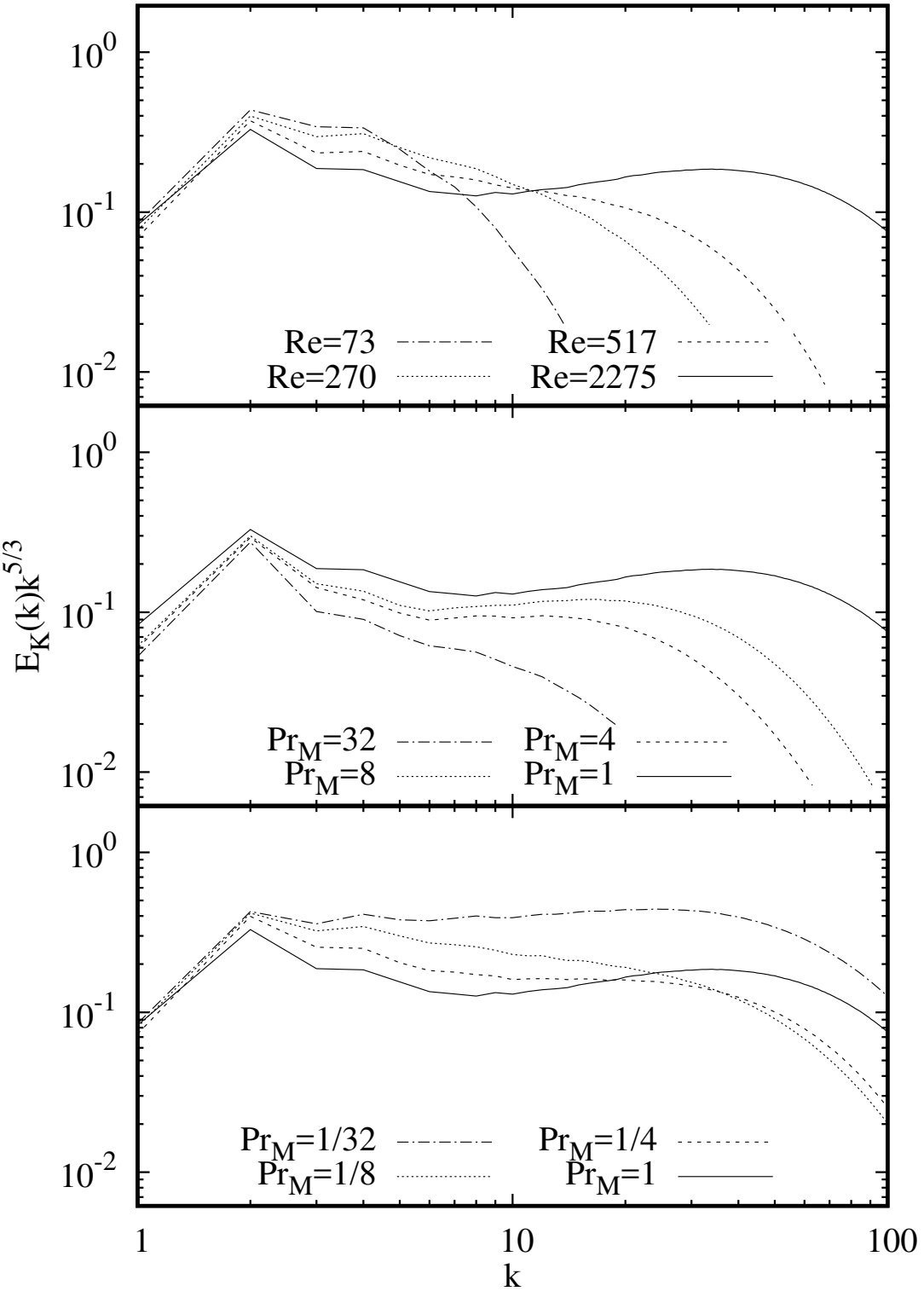

Figure 4.2: Kinetic energy spectra of selected simulations, compensated by $k^{-5/3}$. The top images show data with $\mathrm{Pr_M} = 1$; the second show data with $\mathrm{Re}_M \simeq 2275$ and the third show $\mathrm{Re} \simeq 2275$. In each plot the solid line corresponds to the same simulation, with $\mathrm{Pr_M} = 1$ and $\mathrm{Re} = \mathrm{Re}_M \simeq 2275$.

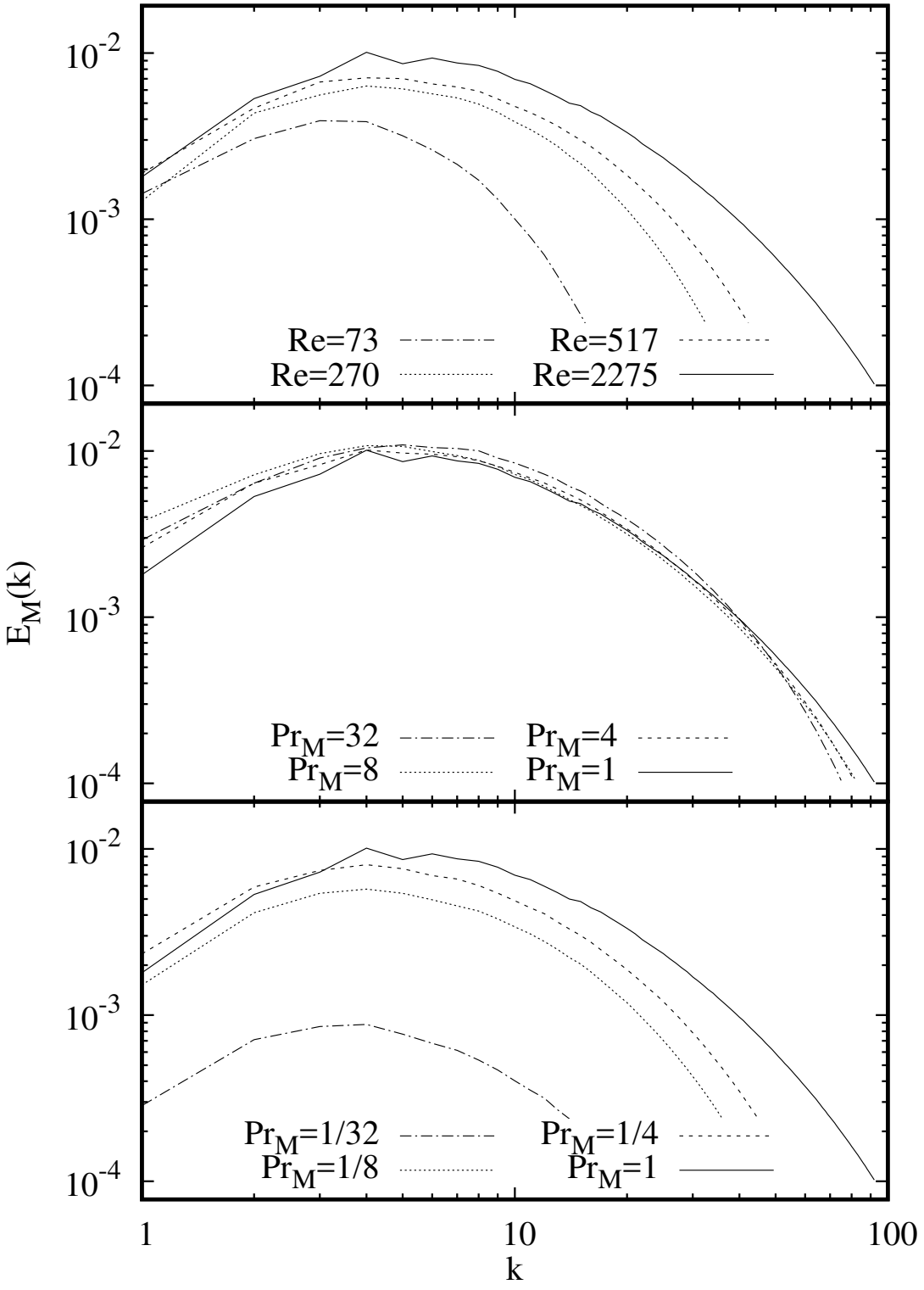

Figure 4.3: Magnetic energy spectra of selected simulations. The top images show data with $\mathrm{Pr_M} = 1$; the second show data with $\mathrm{Re}_M \simeq 2275$ and the third show $\mathrm{Re} \simeq 2275$. In each plot the solid line corresponds to the same simulation, with $\mathrm{Pr_M} = 1$ and $\mathrm{Re} = \mathrm{Re}_M \simeq 2275$.

velocity field is slightly enhanced. The spectrum most closely resembling the Kolmogorov $k^{-5/3}$ scaling is the $\mathrm{Pr_M} = 1/32$ run in the bottom plot. In this case it seems that we are below the threshold for the onset of dynamo action, and so the magnetic field (which was initially in equipartition with the velocity field) will eventually decay completely, leaving a purely hydrodynamic simulation.

The corresponding magnetic energy spectra are shown in Fig. 4.3. The spectra are most heavily influenced by Re_M. In the top and bottom plots, Re_M is varied while $\mathrm{Pr_M}$ and Re are respectively kept constant. The spectra produced in these two plots are relatively similar except in the Re_M=73 case, where for $\mathrm{Pr_M}$=1 the magnetic field is sustained but for $\mathrm{Pr_M}$=1/32 it is decaying. In the second plot we see that increasing $\mathrm{Pr_M}$ with constant Re_M may slightly augment the large-scale magnetic field.

4.2.2 The balance between kinetic and magnetic quantities in forced data

Figure 4.4 shows the time-averaged kinetic-to-magnetic energy ratios as a function of $\mathrm{Pr_M}$, grouped into sets of points with approximately equal Re_M. For fixed Re_M the energy ratios tend to decrease as $\mathrm{Pr_M}$ is increased, although the slope flattens at larger Re_M. Bearing in mind that Re_M doubles with each set of points, we see that the data are converging onto an asymptotic high-Re_M limit. For all values of $\mathrm{Pr_M}$, the ratio E_K/E_M decreases with increasing Re_M. These behaviours are in agreement with what was put forward in [60].

Figure 4.5 shows the kinetic-to-magnetic dissipation ratios for our dataset. Our $\mathrm{Pr_M} > 1$ data collapse onto the same line as Re_M increases, implying asymptotic independence from Re_M when $\mathrm{Pr_M} > 1$. The scalings for nonhelical MHD with $\mathrm{Pr_M} < 1$ and $\mathrm{Pr_M} > 1$ that were proposed in [22] have been indicated. Since for $\mathrm{Pr_M} < 1$ the kinetic dissipation scale was not properly resolved in the simulations reported in [22], it is probable that the measurement of ε_K was affected, and similarly ε_M when $\mathrm{Pr_M} > 1$, so the steepness of the scaling of $\varepsilon_K/\varepsilon_M$ with $\mathrm{Pr_M}$ appears exaggerated for both $\mathrm{Pr_M} < 1$ and $\mathrm{Pr_M} > 1$ compared to our results. In some of our low-$\mathrm{Pr_M}$ runs the magnetic energy was unable to saturate to a steady state and would thus go to zero in the limit $t \to \infty$. This means that the This ambiguity should be kept in mind when considering the energy and dissipation ratios for $\mathrm{Pr_M} < 1$.

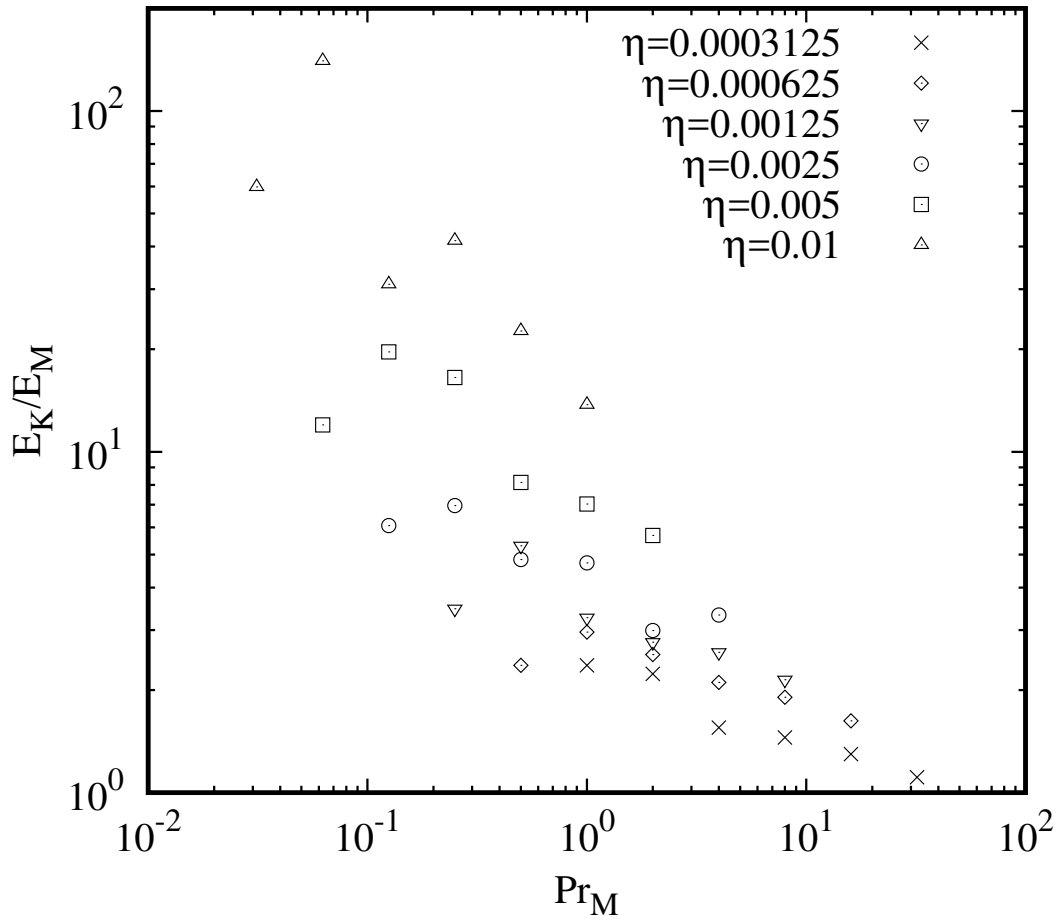

Figure 4.4: Time-averaged kinetic-to-magnetic energy ratios of simulations grouped according to resistivity, η.

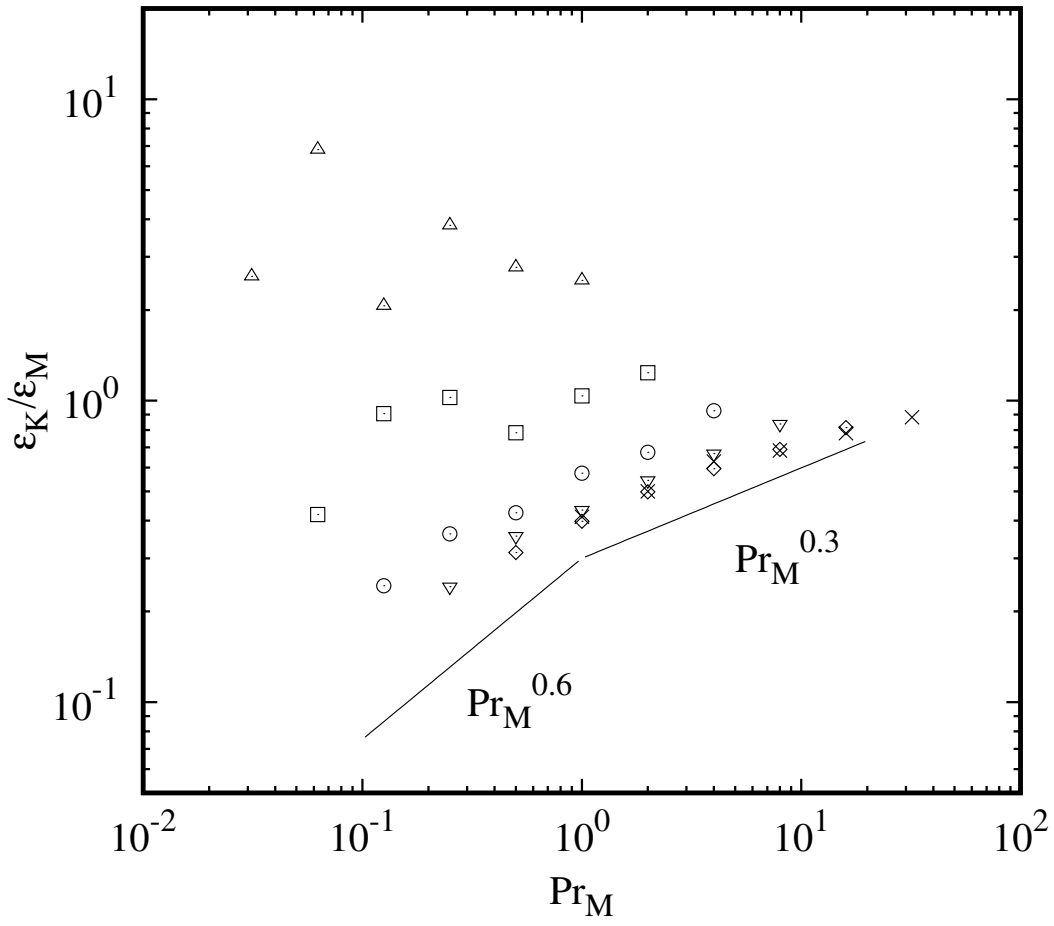

Figure 4.5: Time-averaged kinetic-to-magnetic dissipation rate ratios grouped according to resistivity, η. The simulations with the smallest values of Re_M are marked by an upwards-pointing triangle and those with the largest Re_M are marked by a cross. The symbols are fully defined in the top right corner of Fig. 4.4.

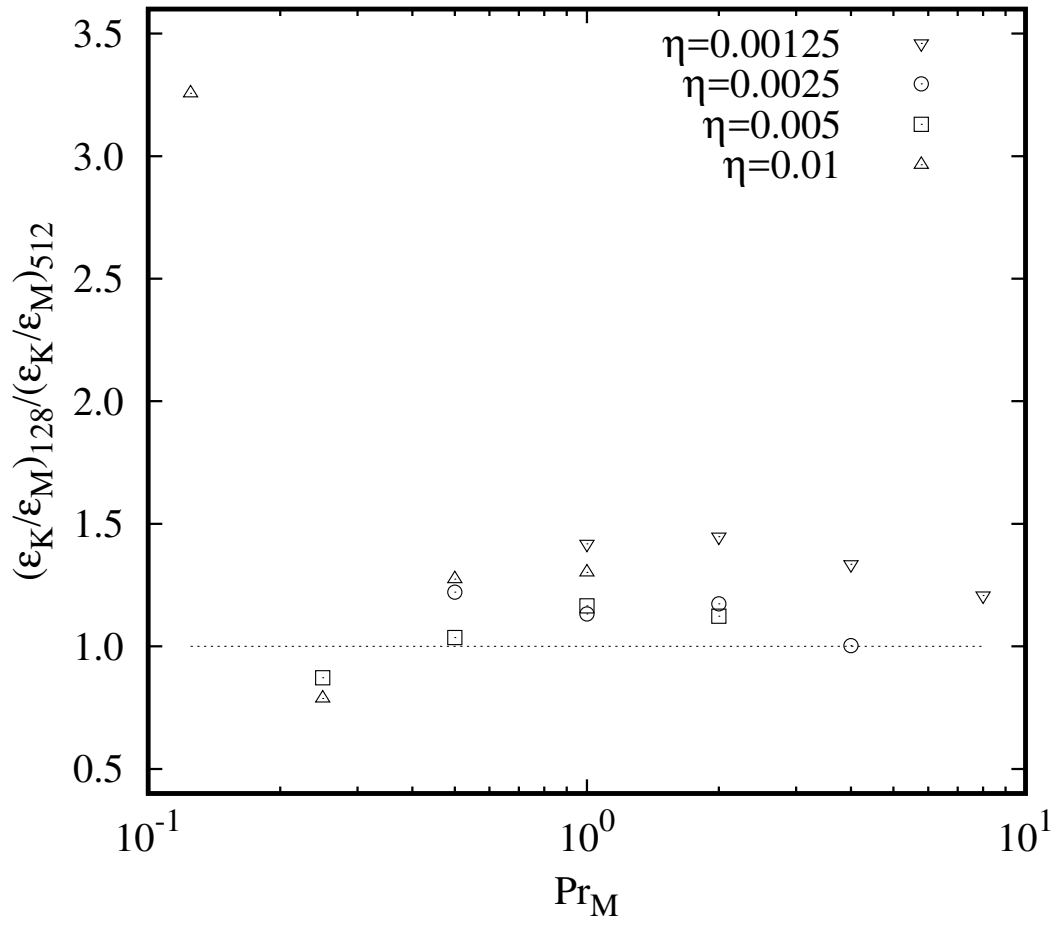

Figure 4.6: Comparison of the time-averaged kinetic-to-magnetic dissipation rate in simulations on a 128^3 lattice $(\varepsilon_K/\varepsilon_M)_{128}$ and on a 512^3 lattice $(\varepsilon_K/\varepsilon_M)_{512}$ with otherwise identical initial conditions.

Small amounts of kinetic-to-magnetic transfer are always present in MHD [79], but are not always strong enough to allow the development of a steady-state magnetic field. Because of this, the critical magnetic Reynolds and Prandtl numbers for the onset of dynamo action are difficult to pinpoint exactly without running the simulations for a very lengthy amount of time.

4.2.3 Resolution

To illustrate the importance of resolution we repeated on a 128^3 lattice our simulations which had been done on a 512^3 lattice; see Fig. 4.6. The low-resolution simulations miscalculated the dissipation ratios by up to 40%, with the biggest discrepancies mostly occuring at high Re_M. Additionally, for $\mathrm{Pr_M} = 1/8$, where dynamo action was not sustainable, the low-resolution dissipation ratio was more than 3 times the high-resolution ratio.

To fully capture the dynamics of nonunity $\mathrm{Pr_M}$ turbulence, careful consideration of resolution is required. A system's energy is mostly concentrated in the largest scales, but the dissipation spectrum is proportional to the wavenumber squared, so good resolution is especially important when comparing dissipative quantities. What follows is a brief discussion outlining some of the theoretical ways in which the small scales may affect the overall evolution.

It is known from analyses of triad interactions and shell-to-shell energy transfers that energy is transferred from the velocity field at the forcing scale to the magnetic and velocity fields at all scales in a way that depends on the separation between the giving and receiving scales and the energy contained in the involved scales, amongst other things [2, 76, 79, 80, 96, 136]. Therefore it is reasonable to expect a consistent scaling of the kinetic-to-magnetic dissipation ratio with $\mathrm{Pr_M}$ that is not affected by whether $\mathrm{Pr_M} < 1$ or $\mathrm{Pr_M} > 1$, as we see in Fig. 4.5. Furthermore, when the velocity field is turbulent over a larger range of scales than the magnetic field, i.e. $k_\nu > k_\eta$ and $\mathrm{Pr_M} < 1$, then for a given Re_M there should be a corresponding value of $\mathrm{Pr_M}$ below which more energy will be transferred to the dissipative part of the magnetic field, $k > k_\eta$, than to $k < k_\eta$. It thus seems natural that the magnetic field would become unsustainable at some critical value of $\mathrm{Pr_M}$, as put forward in [117]. The coupling between the small-scale velocity field and the large-scale magnetic field may be key to tipping the balance in favour of sustainable dynamo action for small values of $\mathrm{Pr_M}$ [20]. Indeed, this explains why the $\mathrm{Pr_M} = 1/8$ result in Fig. 4.6 was so large: dynamo action in the

low-resolution simulation was suppressed.

4.2.4 Reverse spectral transfer in decaying helical and nonhelical MHD

In Fig. 4.3 it seems that the high-Re_M data have more of a build-up of magnetic energy in the largest scales than the lower-Re_M data. Inspired by this, we move on to examining the effect of Re_M and $\mathrm{Pr_M}$ on RST by comparing simulations of decaying MHD turbulence with initially fully helical or nonhelical magnetic fields. We performed 9 pairs of simulations covering the range $1/16 \leq \mathrm{Pr_M} \leq 16$ in multiples of 4, with the extreme values of ν and η being 0.005 and 0.0003125, as shown in Fig. 4.1. These simulations were carried out by Richard Ho and analysed by both of us. The data are publicly available online [128].

To facilitate RST, we set the peak of the initial energy spectra to $k_0 = 40$. Because our simulations were done with RST in mind we turned off the forcing functions and looked at decaying turbulence. Steady-state turbulence is valued because of its better statistics but is does not work well when there is significant RST. This is because artificial large-scale kinetic and magnetic energy sinks must be set up and then the energy injected must be balanced with four dissipative processes, rather than two. The effect of introducing such a change to the MHD equations warrants its own detailed study.

We define the energy in the first 3 wavenumbers of the magnetic field as $E_3(t) = \int_0^3 E_M(k,t)dk$. Since the system is not subject to an external force, then if $E_3(t)$ is constant or increasing, energy must be coming from smaller length scales. We measured $E_3(t)$ until the simulation entered a power law decay of total energy and plotted the results in Fig. 4.7. We found that increasing $\mathrm{Pr_M}$ by increasing Re_M enhances the growth rate of RST, with a stronger effect than increasing $\mathrm{Pr_M}$ by decreasing Re. In general the high-Re_M simulations (top plot in Fig. 4.7) had the most RST. RST was completely shut off at $\mathrm{Pr_M} = 1/16$ but present at $\mathrm{Pr_M} = 1/4$ for high enough Re_M, particularly in the helical case. As far as we are aware, nonhelical RST for $\mathrm{Pr_M} < 1$ has not been seen previously in the literature.

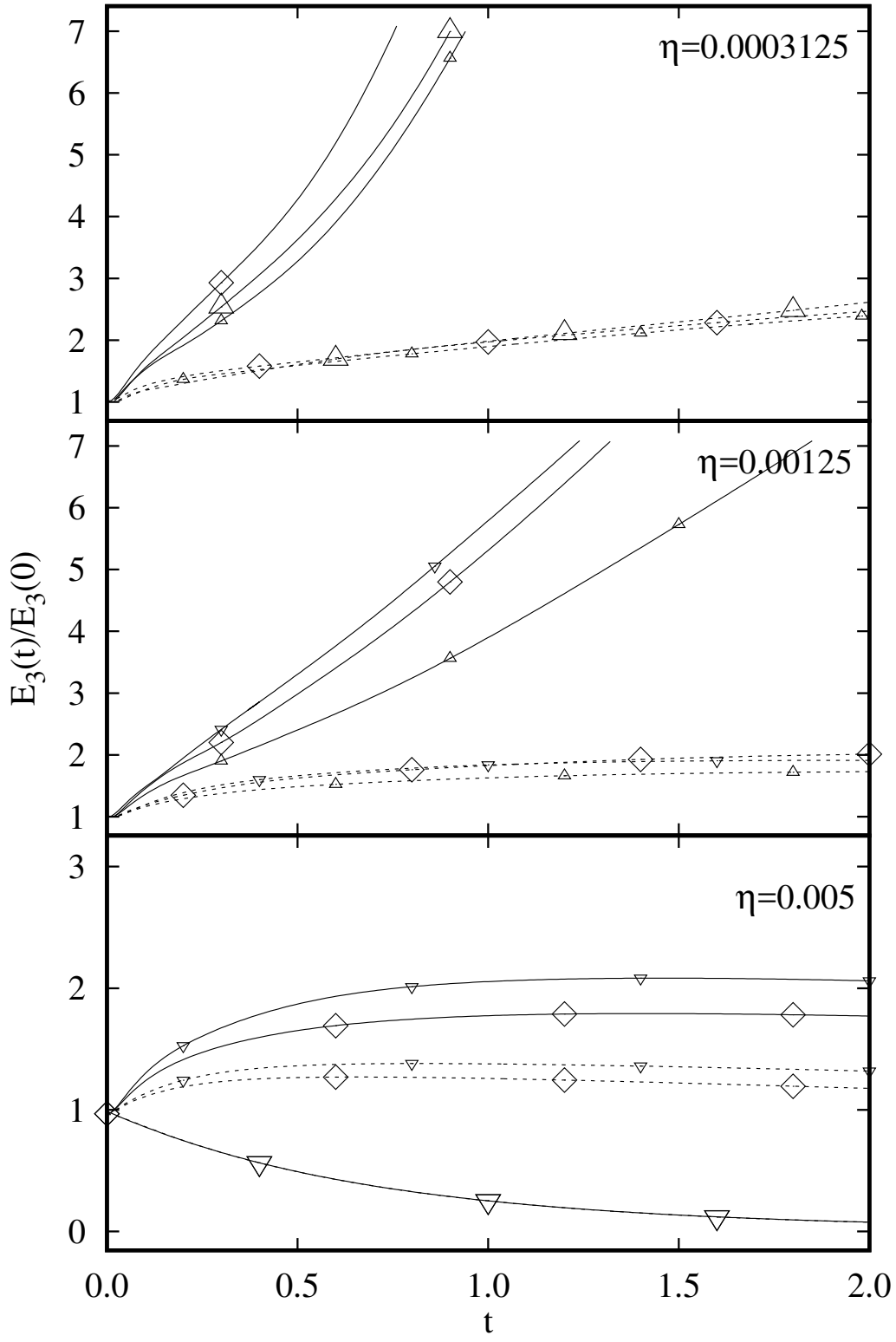

Figure 4.7: $E_3(t)$ normalised by $E_3(0)$ for nonhelical runs (dashed lines) and helical runs (solid lines). Lines with diamond points correspond to $\mathrm{Pr_M} = 1$, upwards-pointing small and large triangles to $\mathrm{Pr_M} = 4$ and 16, and downward-pointing small and large triangles to $\mathrm{Pr_M} = 1/4$ and $\mathrm{Pr_M} = 1/16$.

4.3 Conclusion

The fully-resolved simulations developed in this chapter are a definitive dataset, improving confidence on the scaling and energy transfer properties of MHD in the near couple decade region around unity. Our dataset provides considerable new insights and builds upon the few previous studies in the literature. We have shown that many results rely on reaching a critical Re_M before we find asymptotic dependence on $\mathrm{Pr_M}$. Furthermore, underresolved simulations may exaggerate the scaling of properties such as the kinetic-to-magnetic dissipation ratio by failing to account for all of the dissipative dynamics. In our highly-peaked decaying simulations, not only did we find evidence of RST for both initially helical and nonhelical fields, this RST was possible for even $\mathrm{Pr_M} = 1/4$ with large enough Re_M. This indicates that RST should be possible as long as there is adequate separation of k_1, k_0 and k_η, where $k_1 = 1$ is the largest wavenumber in the system and k_ν is close to the value of k_η or greater.

These results are especially interesting when put in the context of physical applications. Although our simulations feature simple geometry and do not take into account e.g. rotation, approaching complex physical problems from this angle may still have merit. In black hole accretion disks, luminosity is influenced by the dissipation ratios and in tokamaks DNS measurements could be a useful calibration tool. We reiterate that fully-resolved simulations such as ours are vital when it comes to accurately producing dynamo action and other effects incurred by nonunity $\mathrm{Pr_M}$.

Chapter 5

Conclusion and outlook

In this thesis we have explored the way energy is transferred in homogeneous magnetohydrodynamics and the way that length scales affect this. Homogeneity means there is translational symmetry, so rather than comparing the velocity and magnetic fields at different positions in space, it is necessary only to compare their characteristics across different length scales. Roughly speaking, this is like comparing the effects of long waves and short waves. In a generic homogeneous system there are several scales of interest. Two important large scales are

- L, a characteristic scale of the system. This is usually where energy is injected, or in decaying MHD, where the peak of the energy spectrum is. It may then even be a relatively small scale.
- L_{sys}, a system-size scale of the problem, which may or may not coincide with L. For example this could be the domain size in a simulation. If L_{sys} is much larger than L in MHD there is a tendency for net RST to appear.

At the other end of the spectrum there are

- l_ν, the small scale below which viscous dissipative effects are more dominant than turbulent fluid effects.
- l_η, the scale below which magnetic dissipative effects take prevalence over turbulent magnetic effects.
- $\frac{1}{k_{max}}$, the smallest-resolved scale in a simulation or experiment.

Between these large and small scales is the inertial range, which, in hydrodynamics, tends to be self-similar and evolves without memory of large-scale properties. If $l_\nu > l_\eta$ then the magnetic Prandtl number is greater than one, and large-scale RST is more likely to be present. The separation between the dissipative scales and the large length scales is important for the production of a self-similar inertial range, and in MHD (particularly nonhelical systems) the separation between the scale of the system L_{sys} and the peak of the energy spectrum L is also crucial for the production of large-scale RST.

After giving an overview of some of the core concepts of magnetohydrodynamics as well as a selection of its applications, I presented the results of my thesis.

First, three large-scale, nonhelical, mechanical methods of energy injection were compared. It was shown that the mathematical specifics of the forcing function do not play a great role, with the cavet that a small unintentional build-up of cross helicity may occur in deterministically-forced simuluations. This comes as a bit of a surprise because only the velocity field is forced, but it is the coupling of the forcing term to the magnetic field that produces this effect. I therefore recommend that either a stochastic forcing is used, such as the well-known adjustable helicity force defined in section 2.2.2, or that explicit protection against the injection of cross helicity is included in the forcing function.

The triadic nature of MHD interactions was investigated in Chapter 3 using a module of code that I wrote for this purpose. The code identifies the transfer of energy between scales, which necessarily involves three modes. We focussed in particular on the transfer of energy to the magnetic field and showed that the strongest transfers involved one small wavenumber and two similarly-sized wavenumbers; in other words, nonlocal interactions. The transfers themselves were both local and nonlocal, moving energy from the magnetic field and velocity field in roughly equal measures. We also compared the Elsässer transfer functions in simulations with magnetic helicity or cross helicity. Magnetic helicity is not usually examined in the context of Elsässer fields but this viewpoint highlighted that it is very narrow triad shapes, i.e. very nonlocal interactions, that feed back and amplify the large-scales, although this effect does diminish proportionally to the size of the small-scale wavenumbers. A brief discussion on the application of a single-triad helical mode analysis to systems with nonunity magnetic Prandtl number was had, with suggestions for future numerical tests and analysis.

Next, a systematic study of the effect of the magnetic Prandtl number was carried

out by varying the parameter in two ways, i.e. via the viscosity and the magnetic resistivity. Results were collected from 36 mechanically-forced simulations and 18 decaying simulations. This was the first time that the number has been examined in such detail since it is heavily constrained by computing requirements. Our results demonstrated that if the smallest-resolved scale in a simulation is not sufficiently small (i.e. smaller at least than both dissipation scales) then measurements of spectral properties are affected. Large magnetic and kinetic Reynolds numbers are desired so it is tempting to sacrifice the resolution quality. To achieve a good balance between these needs in DNS of homogeneous MHD, we suggest that the smallest-resolved length scale is no more than 80% of the smallest dissipation scale.

We showed that a large-scale magnetic field was able to be sustained in decaying, nonhelical turbulence with $\mathrm{Pr}_M = \frac{1}{4}$ as long as the magnetic Reynolds number was large enough. The field was unsustainable in our $\mathrm{Pr}_M = \frac{1}{16}$ test but perhaps in the future when larger magnetic Reynolds numbers are accessible there will be more evidence of RST in simulations with small magnetic Prandtl number. The essence of this is that RST is enhanced as the magnetic Reynolds number increases, but, for each magnetic Reynolds number there is a corresponding magnetic Prandtl number below which the RST is shut down. Another way to look at it is that if the fluid is too turbulent relative to the magnetic field, RST will not be sustained. This result from homogeneous MHD contributes to the body of knowledge about planetary, stellar and accretion disk physics. Recognising the ubiquity of RST in magnetofluids will lead to better modelling of physical systems.

Recommendations for future work in this area include:

- Consider the effect of magnetic forcing instead of, or in addition to, mechanical forcing. It seems reasonable to assume that this would affect spectral energy transfer behaviour but this has not been well-researched.
- Seek to understand RST, magnetic helicity and the magnetic Prandtl number in the Elsässer formulation. Building a framework for those problems in the Elsässer formulation may seem unintuitive because they are more easily visualisable in terms of the physical fields, but the additional perspective gained could improve the theoretical understanding of issues such as critical Reynolds and Prandtl numbers.
- Quantify the RST compared to forward spectral transfer in *dissipationless* simulations with an initial energy spectrum peaking in intermediate scales.

Perhaps this could clarify how much the directionality of energy transfer is influenced by the difference between the largest, smallest and most energetic scales.

Appendix A

Triple correlations in homogeneous turbulence

Let $A_\alpha(\mathbf{x})$, $B_\beta(\mathbf{x})$ and $C_\gamma(\mathbf{x})$ be three homogeneous fields with Fourier transforms defined in the usual way, e.g.

$$A_\alpha(\mathbf{k}) = \left(\frac{1}{L}\right)^3 \int d^3x A_\alpha(\mathbf{x}) \exp(-i\mathbf{k}\cdot\mathbf{x}) \ . \tag{A.1}$$

The Fourier transform of the triple correlation of these three fields is

$$\begin{aligned}\langle A_\alpha(\mathbf{k}) B_\beta(\mathbf{p}) C_\gamma(\mathbf{q})\rangle = \left(\frac{1}{L}\right)^9 \int\int\int d^3x d^3x' d^3x'' \langle A_\alpha(\mathbf{x}) B_\beta(\mathbf{x}') C_\gamma(\mathbf{x}'')\rangle \\ \times \exp\{-i(\mathbf{k}\cdot\mathbf{x} + \mathbf{p}\cdot\mathbf{x}' + \mathbf{q}\cdot\mathbf{x}'')\} \ .\end{aligned} \tag{A.2}$$

Since the fields are homogeneous, we need only consider relative positions $\mathbf{r} = \mathbf{x} - \mathbf{x}'$ and $\mathbf{r}' = \mathbf{x} - \mathbf{x}''$ and can translate to $\mathbf{x} = 0$. The x-integral is then

$$\left(\frac{1}{L}\right)^3 \int d^3x \exp\{-i(\mathbf{k}+\mathbf{p}+\mathbf{q})\cdot\mathbf{x}\} = \delta(\mathbf{k}+\mathbf{p}+\mathbf{q}) \ , \tag{A.3}$$

and the resulting delta function imposes the condition that the triple correlation in Fourier space is nonzero only when the wavevectors form a triad, i.e.

$$\begin{aligned}\langle A_\alpha(\mathbf{k})B_\beta(\mathbf{p})C_\gamma(\mathbf{q})\rangle =&\delta(\mathbf{k}+\mathbf{p}+\mathbf{q})\\ &\times\left(\frac{1}{L}\right)^6\int\int d^3r d^3r'\langle A_\alpha(0)B_\beta(-\mathbf{r})C_\gamma(-\mathbf{r}')\rangle\\ &\times\exp\{-i(\mathbf{p}\cdot\mathbf{r}+\mathbf{q}\cdot\mathbf{r}')\}\ . \end{aligned}\tag{A.4}$$

Therefore in MHD we may integrate over all values of the wavevectors $\mathbf{k},\mathbf{p}$ and $\mathbf{q}$ when considering the correlations $\langle u_\alpha u_\beta u_\gamma\rangle$ and $\langle u_\alpha b_\beta b_\gamma\rangle$, since all non-triadic combinations vanish.

Bibliography

[1] A. Alexakis. Large-scale magnetic fields in magnetohydrodynamic turbulence. *Phys. Rev. Lett.*, 110:084502, 2013.

[2] A. Alexakis, P. D. Mininni, and A. Pouquet. Shell-to-shell energy transfer in magnetohydrodynamics. I. Steady state turbulence. *Phys. Rev. E*, 72:046301, 2005.

[3] A. Alexakis, P. D. Mininni, and A. Pouquet. On the inverse cascade of magnetic helicity. *Astrophys. J.*, 640:335–343, 2006.

[4] A. Alexakis, P. D. Mininni, and A. Pouquet. Turbulent cascades, transfer, and scale interactions in magnetohydrodynamics. *New Journal of Physics*, 9:298, 2007.

[5] H. Alfvén. Existence of electromagnetic-hydrodynamic waves. *Nature*, 150:405–406, 1942.

[6] K. Alvelius. Random forcing of three-dimensional homogeneous turbulence. *Phys. Fluids*, 11(7):1880–1889, 1999.

[7] ARCHER, `http://www.archer.ac.uk/`.

[8] V. Archontis, S. B. F. Dorch, and A. Nordlund. Nonlinear MHD dynamo operating at equipartition. *Astron. Astrophys.*, 472:715–726, 2007.

[9] K. Avila, D. Moxey, A. de Lozar, M. Avila, D. Barkley, and B. Hof. The onset of turbulence in pipe flow. *Science*, 333(6039):192–196, 2011.

[10] S. A. Balbus and P. Henri. On the magnetic Prandtl number behavior of accretion disks. *Astrophys. J.*, 674:408–414, 2008.

[11] G. K. Batchelor. On the spontaneous magnetic field in a conducting liquid in turbulent motion. *Proceedings of the Royal Society of London A: Mathematical, Physical and Engineering Sciences*, 201:405–416, 1950.

[12] R. Beck, A. Brandenburg, D. Moss, A. Shukurov, and D. Sokoloff. Galactic magnetism: Recent developments and perspectives. *Annu. Rev. Astron. Astrophys*, 34:155–206, 1996.

[13] A. Berera and M. Linkmann. Magnetic helicity and the evolution of decaying magnetohydrodynamic turbulence. *Phys. Rev. E*, 90:041003, 2014.

[14] A. Beresnyak and A. Lazarian. Scaling laws and diffuse locality of balanced and imbalanced magnetohydrodynamic turbulence. *Astrophys. J. Lett.*, 722:L110, 2010.

[15] M. A. Berger and G. B. Field. The topological properties of magnetic helicity. *Journal of Fluid Mechanics*, 147:133–148, 1984.

[16] L. Biferale, S. Musacchio, and F. Toschi. Inverse energy cascade in three-dimensional isotropic turbulence. *Phys. Rev. Lett.*, 108:164501, 2012.

[17] L. Biferale, S. Musacchio, and F. Toschi. Split energy-helicity cascades in three-dimensional homogeneous and isotropic turbulence. *J. Fluid Mech.*, 730:309–327, 2013.

[18] D. Biskamp. *Magnetohydrodynamic Turbulence*. Cambridge University Press, Cambridge, UK, 2003.

[19] S. Boldyrev. Spectrum of magnetohydrodynamic turbulence. *Phys. Rev. Lett.*, 96:115002, 2006.

[20] S. Boldyrev and F. Cattaneo. Magnetic-field generation in Kolmogorov turbulence. *Phys. Rev. Lett.*, 92:144501, 2004.

[21] A. Brandenburg. The inverse cascade and nonlinear alpha-effect in simulations of isotropic helical hydromagnetic turbulence. *Astrophys. J.*, 550(2):824, 2001.

[22] A. Brandenburg. Magnetic Prandtl number dependence of the kinetic-to-magnetic dissipation ratio. *Astrophys. J.*, 791(1):12, 2014.

[23] A. Brandenburg, K. Enqvist, and P. Olesen. Large-scale magnetic fields from hydromagnetic turbulence in the very early universe. *Phys. Rev. D*, 54:1291–1300, 1996.

[24] A. Brandenburg, N. E. L. Haugen, X.-Y. Li, and K. Subramanian. Varying the forcing scale in low Prandtl number dynamos. *Mon. Not. R. Astron. Soc.*, 479(2):2827–2833, 2018.

[25] A. Brandenburg and T. Kahniashvili. Classes of hydrodynamic and magnetohydrodynamic turbulent decay. *Phys. Rev. Lett.*, 118:055102, 2017.

[26] A. Brandenburg, T. Kahniashvili, and A. G. Tevzadze. Nonhelical inverse transfer of a decaying turbulent magnetic field. *Phys. Rev. Lett.*, 114:075001, 2015.

[27] A. Brandenburg, G. J. D. Petrie, and N. K. Singh. Two-scale analysis of solar magnetic helicity. *Astrophys. J.*, 836(1):21, 2017.

[28] B. Brown, M. Miesch, M. Browning, A. Brun, and J. Toomre. Magnetic cycles in a convective dynamo simulation of a young solar-type star. *Phys. Fluids*, 731:1–19, 2011.

[29] R. Bruno and V. Carbone. The solar wind as a turbulence laboratory. *Living Reviews in Solar Physics*, 10(1):2, 2013.

[30] R. Cameron and D. Galloway. High field strength modified ABC and rotor dynamos. *Mon. Not. R. Astron. Soc.*, 367(3):1163–1169, 2006.

[31] R. H. Cameron, M. Dikpati, and A. Brandenburg. The global solar dynamo. *Space Science Reviews*, 210(1):367–395, 2017.

[32] L. Campanelli. Helical magnetic fields from inflation. *Int. Journal of Modern Physics D*, 18(09):1395–1411, 2009.

[33] W. Chen, J. H. Buckley, and F. Ferrer. Search for GeV γ-ray pair halos around low redshift blazars. *Phys. Rev. Lett.*, 115:211103, 2015.

[34] S. Childress. New solutions of the kinematic dynamo problem. *Journal of Mathematical Physics*, 11(10):3063–3076, 1970.

[35] J. Cho and E. T. Vishniac. The anisotropy of magnetohydrodynamic Alfvénic turbulence. *Astrophys. J.*, 539:273–282, 2000.

[36] U. Christensen and P. Olson. A dynamo model interpretation of geomagnetic field structures. *Geophysical Research Letters*, 25(10):1565–1568, 1998.

[37] V. Dallas and A. Alexakis. The signature of initial conditions of magnetohydrodynamic turbulence. *Astrophys. J.*, 788(2):L36, 2014.

[38] V. Dallas and A. Alexakis. Self-organisation and non-linear dynamics in driven magnetohydrodynamic turbulent flows. *Phys. Fluids*, 27(4), 2015.

[39] P. A. Davidson. *An Introduction to Magnetohydrodynamics*. Cambridge University Press, 2001.

[40] O. Debliquy, M. K. Verma, and D. Carati. Energy fluxes and shell-to-shell transfers in three-dimensional decaying magnetohydrodynamic turbulence. *Phys. Plasmas*, 12:042309, 2005.

[41] M. Dobrowolny, A. Mangeney, and P. Veltri. Fully developed anisotropic hydromagnetic turbulence in interplanetary space. *Phys. Rev. Lett.*, 45:144–147, 1980.

[42] J. A. Domaradzki and D. Carati. An analysis of the energy transfer and the locality of nonlinear interactions in turbulence. *Phys. Fluids*, 19:085112, 2007.

[43] S. B. F. Dorch and V. Archontis. On the saturation of astrophysical dynamos: Numerical experiments with the no-cosines flow. *Solar Physics*, 224(1):171–178, 2004.

[44] ECDF, `http://www.ecdf.ed.ac.uk`.

[45] B. Eckhardt. Introduction. turbulence transition in pipe flow: 125th anniversary of the publication of reynolds' paper. *Philos. Trans. R. Soc. London Ser. A*, 367:449, 2009.

[46] W. M. Elsässer. The hydromagnetic equations. *Phys. Rev.*, 79:183, 1950.

[47] V. Eswaran and S. B. Pope. An examination of forcing in direct numerical simulations of turbulence. *Computers & Fluids*, 16(3):257–278, 1988.

[48] C. Federrath. Magnetic field amplification in turbulent astrophysical plasmas. *J. Plasma Phys.*, 82:535820601, 2016.

[49] C. Federrath, J. Schober, S. Bovino, and D. R. G. Schleicher. The turbulent dynamo in highly compressible supersonic plasmas. *Astrophys. J. Lett.*, 797(2):L19, 2014.

[50] C. Finlay. Historical variation of the geomagnetic axial dipole. *Phys. Earth Planet. Inter.*, 170:1–14, 2008.

[51] J. Finn. Magnetic helicity: What is it and what is it good for? *Comments Plasma Phys. Controlled Fusion*, 9:111, 12 1984.

[52] Frick, P., Boffetta, G., Giuliani, P., Lozhkin, S., and Sokoloff, D. Long-time behavior of MHD shell models. *Europhys. Lett.*, 52(5):539–544, 2000.

[53] U. Frisch. *Turbulence: The Legacy of A. N. Kolmogorov*. Cambridge University Press, Cambridge, UK, 1995.

[54] B. Galanti, P. L. Sulem, and A. Pouquet. Linear and non-linear dynamos associated with ABC flows. *Geophysical & Astrophysical Fluid Dynamics*, 66(1-4):183–208, 1992.

[55] D. Galloway. ABC flows then and now. *Geophysical & Astrophysical Fluid Dynamics*, 106(4-5):450–467, 2012.

[56] D. Galloway and U. Frisch. A numerical investigation of magnetic field generation in a flow with chaotic streamlines. *Geophysical & Astrophysical Fluid Dynamics*, 29(1-4):13–18, 1984.

[57] A. D. Gilbert, Y. Ponty, and V. Zheligovsky. Dissipative structures in a nonlinear dynamo. *Geophysical & Astrophysical Fluid Dynamics*, 105(6):629–653, 2011.

[58] P. Goldreich and S. Sridhar. Toward a theory of interstellar turbulence. II. Strong Alfvénic turbulence. *Astrophys. J.*, 438:763–775, 1995.

[59] R. Grappin, J. Léorat, and A. Pouquet. Dependence of MHD turbulence spectra on the velocity field-magnetic field correlation. *Astron. Astrophys.*, 126(1):51–58, 1983.

[60] N. E. L. Haugen, A. Brandenburg, and W. Dobler. Is nonhelical hydromagnetic turbulence peaked at small scales? *Astrophys. J. Lett.*, 597(2):L141, 2003.

[61] N. E. L. Haugen, A. Brandenburg, and W. Dobler. Simulations of nonhelical hydromagnetic turbulence. *Phys. Rev. E*, 70:016308, 2004.

[62] J. D. Hogg and C. S. Reynolds. The dynamics of truncated black hole accretion disks. ii. magnetohydrodynamic case. *Astrophys. J.*, 854(1):6, 2018.

[63] J. D. Hogg and C. S. Reynolds. The influence of accretion disk thickness on the large-scale magnetic dynamo. *Astrophys. J.*, 861(1):24, 2018.

[64] T. S. Horbury, M. A. Forman, and S. Oughton. Spacecraft observations of solar wind turbulence: an overview. *Plasma Physics and Controlled Fusion*, 47(12B):B703, 2005.

[65] H. Hotta, M. Rempel, and T. Yokoyama. Large-scale magnetic fields at high reynolds numbers in magnetohydrodynamic simulations. *Science*, 351(6280):1427–1430, 2016.

[66] L. Huguet, H. Amit, and T. Alboussi?re. Magnetic to magnetic and kinetic to magnetic energy transfers at the top of the Earth's core. *Geophys. J. Int.*, 207(2):934–948, 2016.

[67] S. Ineson, A. Scaife, J. Knight, J. Manners, N. Dunstone, L. Gray, and J. Haigh. Solar forcing of winter climate variability in the northern hemisphere. *Nature Geoscience*, 4:753–7, 2011.

[68] J. Jiménez, A. A. Wray, P. G. Saffman, and R. S. Rogallo. The structure of intense vorticity in isotropic turbulence. *J. Fluid Mech.*, 255:6590, 1993.

[69] T. Kahniashvili, A. Brandenburg, R. Durrer, A. G. Tevzadze, and W. Yin. Scale-invariant helical magnetic field evolution and the duration of inflation. *J. Cosmol. Astropart. Phys.*, 12:002, 2017.

[70] T. Kahniashvili, A. Brandenburg, and A. G. Tevzadze. The evolution of primordial magnetic fields since their generation. *Physica Scripta*, 91(10):104008, 2016.

[71] T. Kahniashvili, A. G. Tevzadze, A. Brandenburg, and A. Neronov. Evolution of primordial magnetic fields from phase transitions. *Phys. Rev. D*, 87:083007, 2013.

[72] Y. Kaneda and T. Ishihara. High-resolution direct numerical simulation of turbulence. *Journal of Turbulence*, 7:N20, 2006.

[73] Y. Kaneda, T. Ishihara, M. Yokokawa, K. Itakura, and A. Uno. Energy dissipation rate and energy spectrum in high resolution direct numerical simulations of turbulence in a periodic box. *Phys. Fluids*, 15(2):L21–L24, 2003.

[74] Käpylä, P. J., Käpylä, M. J., Olspert, N., Warnecke, J., and Brandenburg, A. Convection-driven spherical shell dynamos at varying Prandtl numbers. *A&A*, 599:A4, 2017.

[75] A. P. Kazantsev. Enhancement of a magnetic field by a conducting fluid. *Sov. Phys. JETP*, 25(5):1031–1034, 1968.

[76] R. Kumar, M. Verma, and R. Samtaney. Energy transfers in dynamos with small magnetic Prandtl numbers. *Journal of Turbulence*, 16:1114–1134, 2015.

[77] J. Léorat, U. Frisch, and A. Pouquet. Helical magnetohydrodynamic turbulence and the nonlinear dynamo problem. *Annals of the New York Academy of Sciences*, 257(1):173–176, 1975.

[78] M. Linkmann, A. Berera, and E. E. Goldstraw. Reynolds-number dependence of the dimensionless dissipation rate in homogeneous magnetohydrodynamic turbulence. *Phys. Rev. E*, 95:013102, 2017.

[79] M. Linkmann, A. Berera, M. McKay, and J. Jäger. Helical mode interactions and spectral transfer processes in magnetohydrodynamic turbulence. *J. Fluid Mech.*, 791:61–96, 2016.

[80] M. Linkmann, G. Sahoo, M. McKay, A. Berera, and L. Biferale. Effects of magnetic and kinetic helicities on the growth of magnetic fields in laminar and turbulent flows by helical Fourier decomposition. *Astrophys. J.*, 836(1):26, 2017.

[81] M. F. Linkmann. *Self-organisation processes in (magneto)hydrodynamic turbulence*. PhD thesis, The University of Edinburgh, Scotland, 2016.

[82] M. F. Linkmann, A. Berera, W. D. McComb, and M. E. McKay. Nonuniversality and finite dissipation in decaying magnetohydrodynamic turbulence. *Phys. Rev. Lett.*, 114:235001, 2015.

[83] M. F. Linkmann and A. Morozov. Sudden relaminarization and lifetimes in forced isotropic turbulence. *Phys. Rev. Lett.*, 115:134502, 2015.

[84] A. J. Long, E. Sabancilar, and T. Vachaspati. Leptogenesis and primordial magnetic fields. *Journal of Cosmology and Astroparticle Physics*, 2014(02):036, 2014.

[85] L. Machiels. Predictability of small-scale motion in isotropic fluid turbulence. *Phys. Rev. Lett.*, 79:3411–3414, 1997.

[86] S. K. Malapaka and W.-C. Müller. Large-scale magnetic structure formation in three-dimensional magnetohydrodynamic turbulence. *Astrophys. J.*, 778(1):21, 2013.

[87] W. D. McComb. *Homogeneous, Isotropic Turbulence: Phenomenology, Renormalization and Statistical Closures*. Oxford Science Publications, Oxford, UK, 2014.

[88] W. D. McComb, M. F. Linkmann, A. Berera, S. R. Yoffe, and B. Jankauskas. Self-organization and transition to turbulence in isotropic fluid motion driven by negative damping at low wavenumbers. *J. Phys. A*, 48(25):25FT01, 2015.

[89] M. E. McKay, A. Berera, and R. D. J. G. Ho. Fully-resolved array of simulations investigating the influence of the magnetic Prandtl number, 2018. arXiv:1806.10202.

[90] M. E. McKay, M. Linkmann, D. Clark, A. A. Chalupa, and A. Berera. Comparison of forcing functions in magnetohydrodynamics. *Phys. Rev. Fluids*, 2:114604, 2017.

[91] J. Mendonca, D. Chandra, A. Sen, and A. Thyagaraja. Visco-resistive MHD study of internal kink (m = 1) modes. *Phys. Plasmas*, 25(2):022504, 2018.

[92] M. Miesch, N. Featherstone, M. Rempel, and R. Trampedach. On the amplitude of convective velocities in the deep solar interior. *Astrophys. J.*, 757:128, 2012.

[93] M. Miesch, W. Matthaeus, A. Brandenburg, A. Petrosyan, A. Pouquet, C. Cambon, F. Jenko, D. Uzdensky, J. Stone, S. Tobias, J. Toomre, and M. Velli. Large-eddy simulations of magnetohydrodynamic turbulence in heliophysics and astrophysics. *Space Science Reviews*, 194(1):97–137, 2015.

[94] F. Miniati, G. Gregori, B. Reville, and S. Sarkar. Axion-driven cosmic magnetogenesis during the qcd crossover. *Phys. Rev. Lett.*, 121:021301, 2018.

[95] P. D. Mininni. Inverse cascades and α effect at a low magnetic Prandtl number. *Phys. Rev. E*, 76:026316, 2007.

[96] P. D. Mininni. Scale interactions in magnetohydrodynamic turbulence. *Ann. Rev. Fluid Mech.*, 43:377, 2011.

[97] H. K. Moffat. The degree of knottedness of tangled vortex lines. *J. Fluid Mech.*, 35:117–129, 1969.

[98] R. Monchaux, M. Berhanu, M. Bourgoin, P. Odier, M. Moulin, J.-F. Pinton, R. Volk, S. Fauve, and F. Mordant, N.; Pétrélis. Generation of a magnetic field by dynamo action in a turbulent flow of liquid sodium. *Phys. Rev. Lett.*, 98:044502, 2007.

[99] Moraitis, K., Pariat, E., Valori, G., and Dalmasse, K. Relative magnetic field line helicity. *A&A*, 624:A51, 2019.

[100] W. C. Müller, S. K. Malapaka, and A. Busse. Inverse cascade of magnetic helicity in magnetohydrodynamic turbulence. *Phys. Rev. E.*, 85:015302, 2012.

[101] A. Neronov and I. Vovk. Evidence for strong extragalactic magnetic fields from fermi observations of tev blazars. *Science*, 328(5974):73–75, 2010.

[102] M. Ossendrijver. The solar dynamo. *The Astronomy and Astrophysics Review*, 11(4):287–367, 2003.

[103] D. Peña, H. Amit, and K. J. Pinheiro. Deep magnetic field stretching in numerical dynamos. *Progress in Earth and Planetary Science*, 5(1):8, 2018.

[104] J. C. Perez and S. Boldyrev. Role of cross-helicity in magnetohydrodynamic turbulence. *Phys. Rev. Lett.*, 102:025003, 2009.

[105] Planck Collaboration. Planck 2015 results - XIX. Constraints on primordial magnetic fields. *A&A*, 594:A19, 2016.

[106] F. Plunian, R. Stepanov, and P. Frick. Shell models of magnetohydrodynamic turbulence. *Physics Reports*, 523:1–60, 2013.

[107] J. J. Podesta. On the cross-helicity dependence of the energy spectrum in magnetohydrodynamic turbulence. *Phys. Plasmas*, 18:012907, 2011.

[108] J. J. Podesta and J. E. Borovsky. Scale invariance of normalized cross-helicity throughout the inertial range of solar wind turbulence. *Phys. Plasmas*, 17(11):112905, 2010.

[109] S. B. Pope. *Turbulent Flows*. Cambridge University Press, 2000.

[110] A. Pouquet, U. Frisch, and J. Léorat. Strong MHD helical turbulence and the nonlinear dynamo effect. *J. Fluid Mech.*, 77:321–354, 1976.

[111] A. Pouquet, P. L. Sulem, and M. Meneguzzi. Influence of velocity-magnetic field correlations on decaying magnetohydrodynamic turbulence with neutral X points. *Phys. Fluids*, 31(9):2635–2643, 1988.

[112] A. Ribeiro, G. Fabre, J.-L. Guermond, and J. M. Aurnou. Canonical models of geophysical and astrophysical flows: Turbulent convection experiments in liquid metals. *Metals*, 5:289–335, 2015.

[113] P. Roberts and E. King. On the genesis of Earth's magnetism. *Rev. Prog. Phys.*, 76:096801, 2013.

[114] P. Roberts and A. Soward. A unified approach to mean field electrodynamics. *Astronomische Nachrichten*, 296(2):49–64, 1976.

[115] G. Rüdiger and R. Hollerbach. *The Magnetic Universe: Geophysical and Astrophysical Dynamo Theory*. Wiley-VCH Verlag GmbH & Co. KGaA, 2004.

[116] G. Sahoo, P. Perlekar, and R. Pandit. Systematics of the magnetic-Prandtl-number dependence of homogeneous, isotropic magnetohydrodynamic turbulence. *New Journal of Physics*, 13(1):013036, 2011.

[117] A. A. Schekochihin, S. C. Cowley, J. L. Maron, and J. C. McWilliams. Critical magnetic Prandtl number for small-scale dynamo. *Phys. Rev. Lett.*, 92:054502, 2004.

[118] J. Schober, A. Brandenburg, I. Rogachevskii, and N. Kleeorin. Magnetic Prandtl number dependence of turbulence generated by chiral mhd dynamos, 2018. arXiv:1803.06350 [physics.flu-dyn].

[119] J. Schober, D. Schleicher, C. Federrath, S. Glover, R. S. Klessen, and R. Banerjee. The small-scale dynamo and non-ideal magnetohydrodynamics in primordial star formation. *Astrophys. J.*, 754(2):99, 2012.

[120] C. Schrijver and G. Siscoe. *Heliophysics: Evolving Solar Activity and the Climates of Space and Earth*. Cambridge University Press, 2010.

[121] J. V. Shebalin, W. H. Matthaeus, and D. Montgomery. Anisotropy in MHD turbulence due to a mean magnetic field. *J. Plasma Phys.*, 29:525–547, 1983.

[122] S. Sridhar and P. Goldreich. Toward a theory of interstellar turbulence. I. Weak Alfvénic turbulence. *Astrophys. J.*, 432:612–621, 1994.

[123] S. Stanley and G. Glatzmaier. Dynamo models for planets other than Earth. *J. Fluid Mech.*, 152:617–649, 2010.

[124] R. Stepanov, F. Plunian, M. Kessar, and G. Balarac. Systematic bias in the calculation of spectral density from a three-dimensional grid. *Phys. Rev. E*, 90:053309, 2014.

[125] T. Stribling and W. H. Matthaeus. Relaxation processes in a low-order three-dimensional magnetohydrodynamics model. *Physics of Fluids B: Plasma Physics*, 3(8):1848–1864, 1991.

[126] K. Subramanian. The origin, evolution and signatures of primordial magnetic fields. *Reports on Progress in Physics*, 79(7):076901, 2016.

[127] `http://dx.doi.org/10.7488/ds/1999`.

[128] `http://dx.doi.org/10.7488/ds/2361`.

[129] S. M. Tobias, F. Cattaneo, and N. H. Brummell. On the generation of organised magnetic fields. *Astrophys. J.*, 728:153, 2011.

[130] C. Y. Tu and E. Marsch. Mhd structures, waves and turbulence in the solar wind: Observations and theories. *Space Science Reviews*, 73(1):1–210, 1995.

[131] M. S. Turner and L. M. Widrow. Inflation-produced, large-scale magnetic fields. *Phys. Rev. D*, 37:2743, 1988.

[132] P. O. U. Christensen and G. A. Glatzmaier. Numerical modelling of the geodynamo: a systematic parameter study. *Geophys. J. Int.*, 138:393–409, 1999.

[133] T. Vachaspati. Fundamental implications of intergalactic magnetic field observations. *Phys. Rev. D*, 95:063505, 2017.

[134] M. K. Verma. Nonclassical viscosity and resistivity of the solar wind plasma. *Journal of Geophysical Research: Space Physics*, 101(A12):27543–27548, 1996.

[135] M. K. Verma. Satistical theory of magnetohydrodynamic turbulence: recent results. *Physics Reports*, 401(5-6):229–380, 2004.

[136] F. Waleffe. The nature of triad interactions in homogeneous turbulence. *Phys. Fluids A*, 4:350–363, 1992.

[137] B. Weiss, J. Gattacceca, S. Stanley, P. Rochette, and U. Christensen. Paleomagnetic records of meteorites and early planetesimal differentiation. *Space Sci. Rev.*, 152:341–390, 2010.

[138] S. R. Yoffe. *Investigation of the transfer and dissipation of energy in isotropic turbulence*. PhD thesis, The University of Edinburgh, Scotland, 2012.

[139] Z. Zeren and B. Bédat. Spectral and physical forcing of turbulence. In *Progress in Turbulence III: Proceedings of the iTi Conference in Turbulence 2008*, pages 9–12. Springer Berlin Heidelberg, 2010.

[140] H. Zhang, A. Brandenburg, and D. D. Sokoloff. Magnetic helicity and energy spectra of a solar active region. *Astrophys. J. Lett.*, 784(2):L45, 2014.